THESIS FOR THE DEGREE OF DOCTOR OF PHILOSOPHY

High-Temperature Corrosion Behavior in Biomass- and Waste-Fired Boilers

Insights into catastrophic corrosion and corrosion mitigation techniques

Julien Phother-Simon

Department of Chemistry and Chemical Engineering

CHALMERS UNIVERSITY OF TECHNOLOGY

Gothenburg, Sweden 2020

High-Temperature Corrosion Behavior in Biomass- and Waste-Fired Boilers
Insights into catastrophic corrosion and corrosion mitigation techniques
Julien Phother-Simon
ISBN: 978-91-7905-353-6

Doktorsavhandlingar vid Chalmers tekniska högskola
Ny serie nr 4820
ISSN 0346-718X

Department of Chemistry and Chemical Engineering
Chalmers University of Technology
SE-412 96 Gothenburg
Sweden
Telephone + 46 (0)31-772 1000

Cover:
(From left to right)
Picture of a boiler owned by E.ON Värme AB at Händelöverket in Norrköping, Sweden.
Picture showing superheater tubes non-exposed (top) and after service (bottom).
SEM image using BSE of a 347H sample after an 8000-hour exposure in the Steamboost superheater.
Ultra-high-resolution SEM image using SE of a KCl crystal on top of an iron oxide scale.
3D reconstruction and rendering of intergranular corrosion in a 304L sample.
TEM image using high-angle annular dark-field (HAADF) of a grain boundary attack. Picture provided courtesy of Dr. Imran Hanif.

Printed by Chalmers Reproservice
Gothenburg, Sweden 2020

ABSTRACT

Carbon dioxide is contributing to the greenhouse effect and a significant part comes from the use of fossil fuels. Utilizing more renewable fuels is therefore a solution to decrease the net release of CO_2 emissions to the atmosphere. This can be achieved by substituting fossil fuels, such as coal and oil, with renewable fuels, such as biomass and waste. However, the combustion of these renewable fuels releases corrosive species creating corrosion challenges for critical parts of the plants, resulting in lower electrical efficiency and higher maintenance costs. It is therefore necessary to understand and investigate the corrosion attack that occurs in this type of environment, in order to find sustainable solutions.

High-temperature corrosion research can be divided into two steps: laboratory investigations focus on determining the role or influence of different parameters such as water vapor content or specific corrosive species, while field investigations are more oriented towards *in-situ* studies to test ideas developed within laboratory studies for mitigation of the corrosion attack.

Both approaches are included within the scope of this thesis to broaden the knowledge about the accelerated corrosion of steels, as well as investigate different techniques of mitigation of high-temperature corrosion occurring in biomass- and waste-fired boilers.

The laboratory investigations in this thesis focused on KCl-induced corrosion of steels at elevated temperatures (600 °C). A setup allowing a continuous supply of a corrosive species (KCl) during the whole exposure was developed. This generated a corrosive environment mimicking a boiler environment and a corrosion attack better resembling the attack observed in commercial boilers compared to previous methods.

Within this setup, four commercial/steels/alloys were investigated and selected in such a way that they represent a broad range of material classes, but also to contain an increasing amount of nickel (from 0 wt.% to 62 wt.%). The results showed that the corrosion attack could be divided into two corrosion morphologies: general corrosion and steel grain boundary attack. Increasing the nickel content resulted in a decrease of the thickness of the general oxide scales. The corrosion attack of the steel grain boundary exhibited a different trend. The attack became more severe when nickel is part of the alloy’s composition.

In order to improve the understanding of the corrosion attack in this type of environment, an in-depth study of intergranular corrosion (steel grain boundary attack) in a stainless steel (304L) using the state-of-the-art combination of 3D tomography and TEM was performed. The grain boundary corrosion attack was characterized in detail and revealed new insights of how this complex attack progresses. Very small amounts of Cl were observed in the corrosion front together with very large depletion zones.

The design of a new material exhibiting outstanding corrosion resistance properties, excellent mechanical strength, and reasonable costs for application in biomass- and waste-fired boilers is both difficult and time-demanding. Another approach is to separate these properties using a base material (with good mechanical properties) with a corrosion resistant coating. In this work, a set of nickel-based coatings (NiCr, NiAl and NiCrAlY) were investigated in a KCl-rich environment for up to 168 hours. The results showed that the NiAl and NiCrAlY coatings performed well. However, it is necessary to perform a more advanced investigation, i.e. longer durations of exposure, to ascertain their reliability.

Another way to mitigate the high-temperature corrosion experienced in boilers would be to alter the environment. Two studies of this alternative solution were investigated in this thesis. A potential new position for superheaters predicted via CFD (Computational Fluid Dynamics) calculations was studied and showed that it is possible to decrease the amount of corrosive species (chlorides) in the deposits.

Within the similar scope of making the environment milder for the materials, another technical solution was investigated, the Sulfur Recirculation technique. In this setup, the corrosion history caused by a variation in fuel (corrosion memory effect) was studied and the results showed that the corrosion memory effect can influence positively (when exposed first in a mild environment) and negatively (when exposed first in a corrosive environment) the future corrosion behavior of a material.

Keywords: High-temperature corrosion, KCl-induced corrosion, Stainless steel, Ni-based alloy, Coating, 3D tomography, TEM, Biomass, Waste, Deposits, Sulfur Recirculation

LIST OF PUBLICATIONS

This thesis is based on the following papers:

Paper I

J. Phother-Simon, T. Jonsson, J.Liske

“Continuous KCl addition in high temperature exposures of 304L: A way to mimic a boiler environment”

Corrosion Science (2020). doi:10.1016/j.corsci.2020.108511

Paper II

J. Phother-Simon, I. Hanif, J. Liske, T. Jonsson

“High-temperature corrosion of P91/T91, 304L, Sanicro 28 and Inconel 625 exposed at 600 °C under continuous KCl deposition”

Manuscript

Paper III

J. Phother-Simon, I. Hanif, T. Jonsson

“The influence of a KCl-rich environment on the corrosion attack of 304L: 3D FIB/SEM and TEM investigation”

Manuscript

Paper IV

Y C Malede, J. Phother-Simon, T. Jonsson, M. Montgomery, K V. Dahl, J. Hald

“KCl-induced of Ni-based alloys containing 35-45 wt% Cr”

Materials and Corrosion (2019). 10.1002/maco.201810658

Paper V

E. Sadeghimeresht, J. Eklund, J. Phother-Simon, J. Liske, N. Markocsan, S. Joshi

“Effect of water vapor on the oxidation behavior of HVAF-sprayed NiCr and NiCrAlY coatings”

Materials and Corrosion (2019). 10.1002/maco.201710005

Paper VI

J. Eklund, J. Phother-Simon, E. Sadeghimeresht, S. Joshi, J. Liske

"High-Temperature Corrosion of HVAF-Sprayed Ni-Based Coatings for Boiler Applications"

Oxidation of metals (2019). doi:10.1007/s11085-019-09906-0

Paper VII

M. Dolores Paz, J. Phother-Simon, L. Mikkelsen, T. Jonsson

"Increased steam temperature with Steamboost superheater: The effect of the combustion in deposits and high temperature corrosion"

Proceeding, Impact Fuel Quality, Prague, Czech Republic, 2016

Paper VIII

M. Dolores Paz, J. Phother-Simon, S. Andersson, T. Jonsson

"High-temperature corrosion memory in a waste-fired boiler: Influence of sulfur"

(Submitted to Fuel Processing Technology)

Statement of the author's contribution

Paper I: I was the main author of the paper and performed all the experimental and analytical work.

Paper II: I was the main author of the paper and performed all the experimental and analytical work.

Paper III: I was the main author of the paper and performed the corrosion tests, SEM investigation, 3D serial sectioning, and 3D reconstruction.

Paper IV: I co-authored the paper and performed part of the corrosion tests and analyses of the exposed samples.

Paper V: I co-authored the paper and performed part of the corrosion tests and analyses of the exposed samples.

Paper VI: I co-authored the paper and performed part of the corrosion tests and analyses of the exposed samples.

Paper VII: I co-authored the paper and assisted in the microscopy analyses, the ion chromatography, and the work performed in the boiler.

Paper VIII: I co-authored the paper and assisted in the microscopy analyses, the ion chromatography, and the work performed in the boiler.

ACKNOWLEDGEMENTS

I would like to thank all the people who made this PhD thesis possible.

I would like to thank my supervisors, Professor Jan-Erik Svensson, Associate Professor Jesper Liske and Dr. Torbjörn Jonsson not only for giving me the opportunity to pursue a PhD in their research group, but also for their supervision, their support, their time, their knowledge and of course their company as well as the friendly discussions outside of work.

I would like also to thank Professor Lars-Gunnar Johansson and Professor Vratislav Langer for their kind support.

I also gratefully acknowledge the High Temperature Corrosion Center (HTC), Konsortiet för Materialteknik för termiska Energiprocesser (KME), the Biokraft program by the Swedish Energy Agency (SEA), and all the member companies for, support and funding.

The CMAL group, past and present, the senior research engineer Anders Kvist, research engineer Stefan Gustafsson, and research engineer Reza Zamani for their kind assistance.

Sandra Gustafsson, Christina Andersson, Susanne Bågenfelt are gratefully acknowledged for their assistance with administrative issues and Esa Väänänen, Erik Brunius, and Torbjörn Jönsson are gratefully acknowledged for all their technical support.

Special thanks to Dr. Christine Geers and Dr. Loli Paz, the first people to introduce me to HTC, giving me the first impressions of life as a PhD student within the group. Special thanks also to Dr. Niklas Israelsson for his kind help at the beginning of my PhD. Lars Mikkelsen and Sven Andersson are gratefully acknowledged for arranging the work in the field, a pleasant visit in the industry, and also for delightful discussions.

I also thank my office mates Vedad Babic and Robin Faust for making a special working room, a peaceful place suitable for the high productivity of work and for deep science discussions.

I would like to thank in a more general way all my colleagues within the HTC, that made my doctoral studies an amazing experience in the academic world.

Last but not least, I would like to thank my family and friends. Most of all my parents, who supported and continue to support me no matter how old I am and no matter where I am. Special thanks to all the housemates I had the chance to meet during my PhD period, making my home better than I could have imagined. And finally, all the friends I met during these four/five years that made my experience in Sweden an incredible journey.

Contents

1. Introduction

The greenhouse effect is an important feature for life on Earth. The principle relies on greenhouse gases, such as carbon dioxide, which confine the heat on Earth's surface making the climate livable. In general, the more greenhouse gases in the atmosphere, the more heat is confined. Therefore, an increase in net emission of greenhouse gases would lead to an increase in the overall temperature of Earth's surface. This has been observed since the industrial revolution; the concentration of carbon dioxide in the atmosphere has increased more than a third due to human activity [1]. Such an increase would normally occur over thousands of years but is now happening over decades. The consequences are noticeable: drier droughts, more intense storms, and environmental changes that are faster than the ability of some living beings to adapt [1]. Naturally, humans are and will also be affected by these changes from an environmental aspect and a socio-economic aspect [2]. A decrease in the amount of greenhouse gases released to the atmosphere is therefore crucial in order to minimize climate change.

Subsequently, several countries have agreed to combat the phenomenon by reducing the release of greenhouse gases and more specifically carbon dioxide [3-5]. A major contribution to the release of carbon dioxide to the atmosphere comes from the use of fossil fuels [1]. Thus, increasing the utilization of renewable fuels would be one solution to reduce the net release of carbon dioxide emissions to the atmosphere. However, in the field of powerplants, the combustion of renewable fuels such as biomass and waste produce corrosive deposits and gases[6-8]. From a corrosion aspect, the flue gas originating from combustion consists of mainly alkali chlorides, water vapor, and hydrogen chloride [6-13]. Such species are extremely aggressive towards superheaters [14-25], leading to higher maintenance costs and lower electrical efficiency than powerplants using fossil fuels. When fossil fuels, such as oil and coal, are used for combustion, the corrosion rate experienced by superheaters is considerably low. The steam temperature can therefore remain high e.g. 650 °C, while for biomass- and waste-fired powerplants, the range of temperature is kept between 350 and 550 °C [26]. However, when the steam temperature is reduced, the electrical efficiency is reduced as well, making powerplants using renewable fuels less competitive than powerplants using fossil fuels. Thus, to increase the competitiveness of powerplants utilizing renewable fuels, it is necessary to investigate the corrosion phenomena to find suitable solutions. However, the understanding of the corrosion mechanisms behind the aggressiveness of the flue gas towards superheaters remains partially elucidated. It is therefore crucial to increase knowledge about these corrosion phenomena.

This thesis aims at expanding knowledge about accelerated corrosion of steels, as well as demonstrating different techniques for the mitigation of high-temperature corrosion occurring in biomass- and waste-fired boilers. For these purposes, laboratory and field investigations were conducted as follows:

The study of accelerated corrosion was mainly investigated in laboratory. Laboratory investigations focused on the KCl-induced corrosion on steels at elevated temperatures (600 °C). The difference between the performed investigations in this thesis and traditional studies investigating KCl-induced corrosion [17-19, 22-24, 27, 28] was the continuous supply of salt during the whole exposure. This was possible due to an experimental setup allowing the continuous deposition (via condensation) of KCl onto samples. This resulted in the materials experiencing accelerated corrosion, which reached breakaway oxidation. This was characterized by the loss of the original protective oxide (primary protection) and the growth of a fast-growing oxide (secondary protection). This experimental setup was the foundation of the laboratory investigations of this thesis.

In the first part, a comparative study investigating the secondary protection of four commercial alloys with varying amounts of nickel was conducted. The influence of alloying elements such as chromium or nickel on the high-temperature corrosion resistance of alloys when the primary protection has been lost is not fully understood. For this purpose, these materials were tested in the referred experimental setup.

In the second part, an investigation combining 3D tomography and Transmission Electron Microscope (TEM) was conducted to improve the understanding of the role of chlorine in intergranular corrosion of stainless steels. This study aimed at providing more accurate representations of and new insights into intergranular corrosion in stainless steels.

The last part entailed collaboration between the Technical University of Denmark (DTU) and Chalmers University of Technology (CTH). The aim was to investigate further the influence of the microstructure of a nickel-based alloy on a KCl-induced corrosion attack.

The different techniques for corrosion mitigation were studied in both laboratory and field.
The first study investigated the performance of three nickel-based coatings when exposed to simulated mild and harsh environments. The second study explored the potential of a new location for superheaters in a grate-fired boiler. The last study investigated the influence of a novel sulfur-addition technique on the corrosion history of materials exposed to grate-fired boilers.

2. Biomass- and waste-fired boilers

The principle of boilers or powerplants relies on the hot flue gas originating from the combustion of fuels. The flue gas is used to heat water to steam with heat exchangers, such as superheaters and water walls. The superheated steam goes through a steam turbine that produces electrical power. The average efficiency for electrical power production is approximatively 20 – 30%. However, it is also possible to use the steam leaving the turbine for district heating, thus increasing the total energy efficiency of the powerplant to nearly 80%[29, 30]. Such a combination for energy production is called Combined Heat and Power (CHP). The nature of the energy produced by a boiler (only electrical, heat, or CHP) is based on neighboring needs. As an example, Sweden and many other cold countries rely heavily on district heating due to environmental conditions. Therefore, CHPs are highly suitable for such regions.
Among the different types of boilers used for biomass and waste, two are commonly used:

- Grate-Fired (GF) boilers.
- Fluidized Bed Combustion (FBC) boilers.

- Grate-Fired boilers

In grate-fired boilers, the fuel is added from the top of a grate and is carried to the bottom of the grate using e.g. rotary or vibrating grates. Thus, the combustion of the fuel occurs on a grate. Air is injected from below the grate in order to sustain the combustion process with oxygen and reduce the temperature of the metal grate. Difficult fuels, such as straw or high-alkaline-containing crops, are better processed in this type of boiler than in an FBC boiler due to the high-agglomeration tendency of these fuels [31]. Another asset of this type of boiler compared to FBC boilers is the lack of extensive fuel preparation. In a grate-fired boiler, there is no (or little) fuel preparation while FBC boilers require the fuel to be reduced to fine particles (the size of particles depends on restrictions) to allow the fluidization of the bed. A schematic drawing of a grate-fired boiler is presented below in Figure 1:

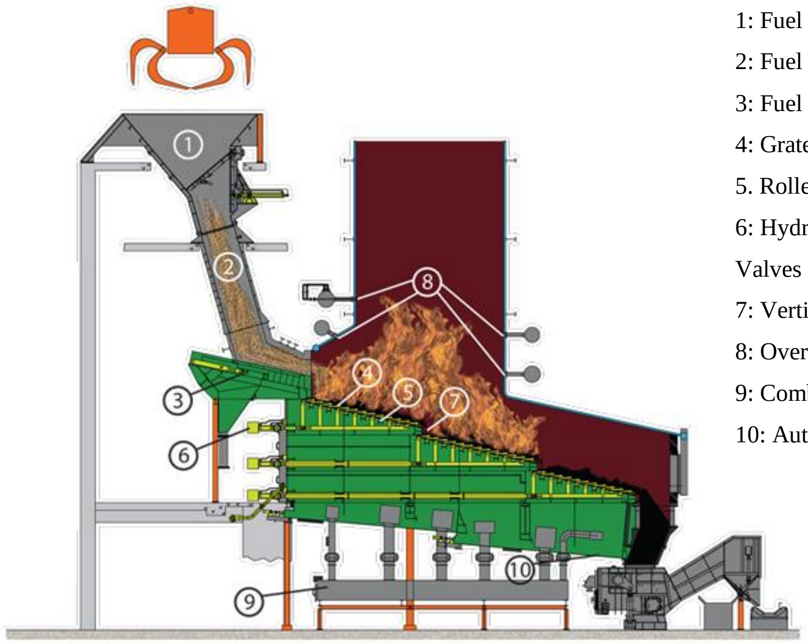

1: Fuel Charging Hopper
2: Fuel Charging Throat
3: Fuel Charging Ram
4: Grates
5. Roller Bearings
6: Hydraulic Power Cylinders and Control Valves
7: Vertical Drop Off
8: Overfire/Secondary Air
9: Combustion air (Primary Air)
10: Automatic Sifting Removal System

Figure 1: Schematic drawing of a grate-fired boiler [32].

❖ Fluidized Bed Combustion boilers

This type of boiler allows the combustion of a fuel to take place in a hot bed of particulate materials (mainly sand) and ash. The result is a blend of gas and solids that improves heat transfer and chemical reactions within the bed. Air injected from the bottom of the bed induces the fluidization of the bed. Recent work aimed at improving the efficiency of the combustion of these boilers has been performed. The principle is named Oxygen Carrier Aided Combustion (OCAC) and relies on incorporating an oxygen carrier (ilmenite in these studies) into the bed to distribute more homogeneously the oxygen in the furnace, allowing for more efficient combustion [33-35].

Different regimes of fluidization can be attained and depend on several parameters such as the velocity of the gas, particles' physical properties (size, shapes, and density) or the bed's geometries. Among these different regimes of fluidization, two are commonly used: Bubbling Fluidized Bed (BFB) and Circulation Fluidized Bed (CFB). CFB boilers show a higher efficiency than BFB boilers due to the solid separators that recycle unburned particles to the lower part of the furnace. Overall, Fluidized Bed technology exhibits good fuel flexibility [31]. A schematic drawing of a CFB boiler is illustrated below in Figure 2:

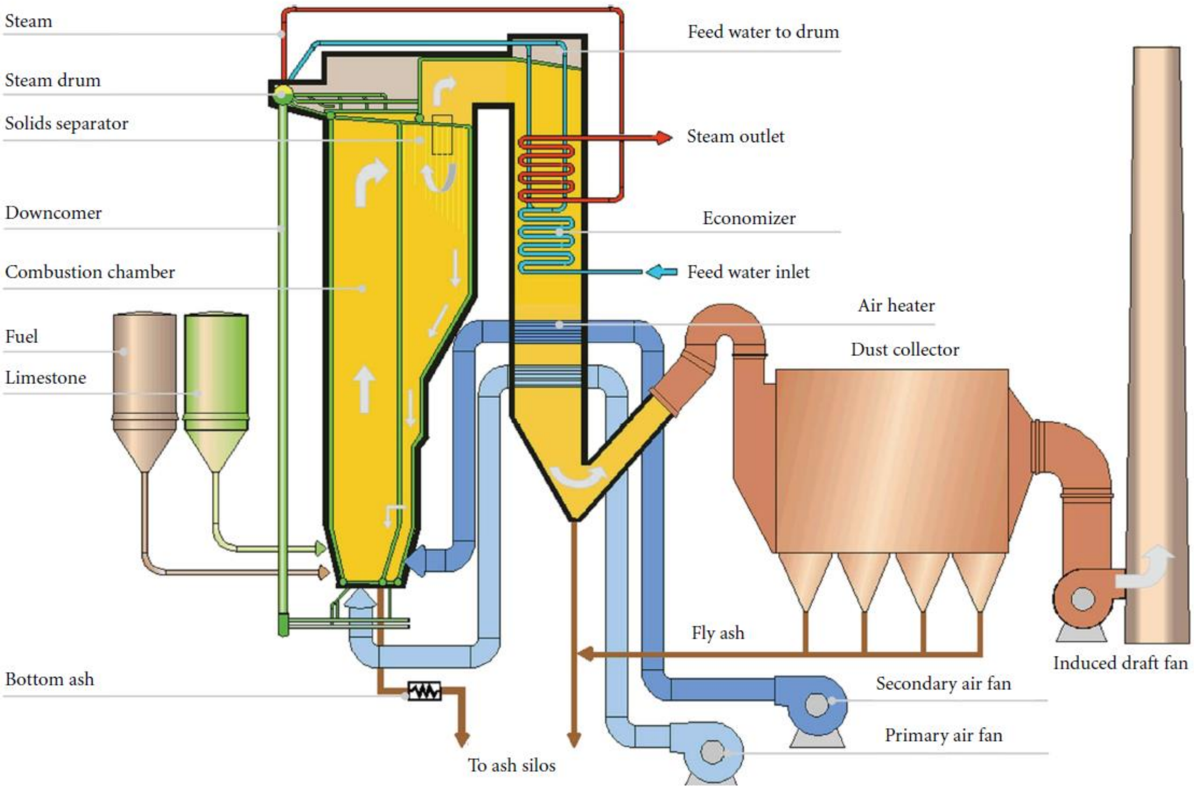

Figure 2: Schematic drawing of a CFB boiler [36].

- Fuels in biomass- and waste-fired boilers

Reducing the net emission of CO_2 released to the atmosphere can be achieved by replacing fossil fuels with renewable fuels in power plants. Several countries, such as Sweden, have decided to make a change in the fuels used in power plants. This has been achieved by gradually increasing the fraction of biomass and waste of the fuel [37, 38]. This trend can be observed in Sweden and more specifically at the Händelö plant located in Norrköping, where fossil fuels have been nearly completely substituted with renewable fuels(Figure 3):

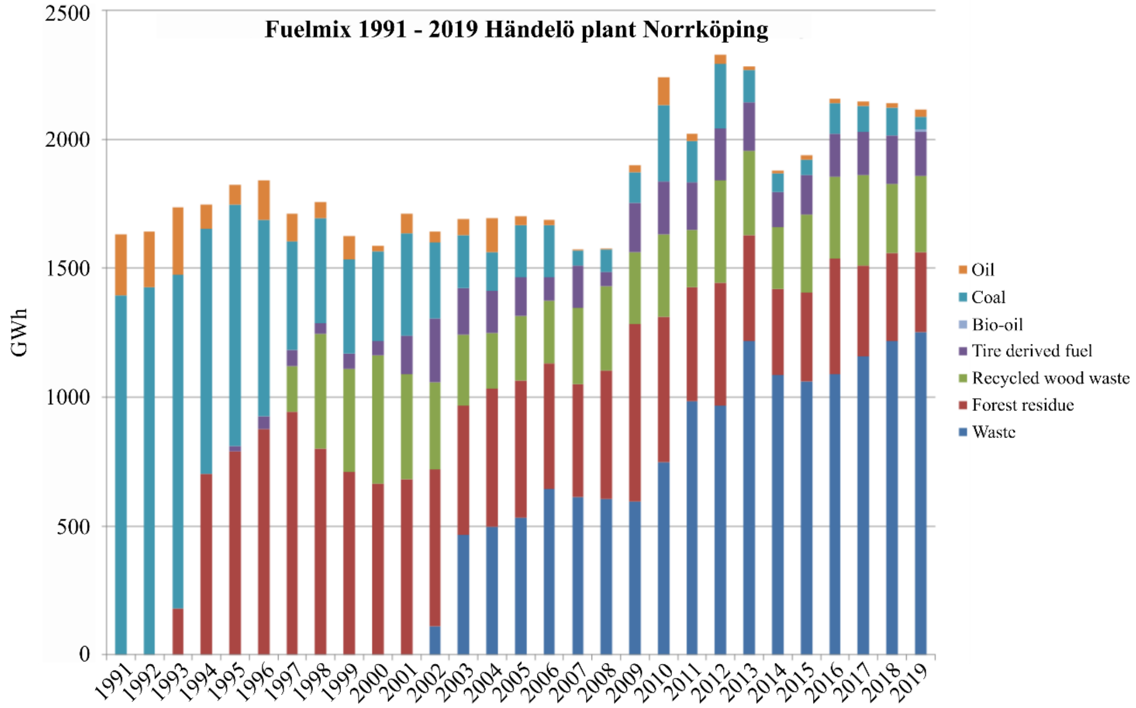

Figure 3: Power generation by fuel type from 1991 to 2019 at the Händelö plant (owned by E.ON Värme AB) in Norrköping, Sweden [39].

However, the composition of renewable fuels is different from fossil fuels. This results in the production of a flue gas during combustion that is different as well. Renewable fuels used in biomass- and waste-fired plants exhibit a higher content of water vapor and alkali chlorides than boilers using fossil fuels. This results in a higher level of hydrochloric acid (HCl) and a lower level of sulfur dioxide (SO_2) (see Table 1). It has been reported that the presence of alkali chlorides in the flue gas, and in a more general way, a chlorine-containing environment, induces a severe corrosion attack on biomass- and waste fired-boilers [14, 16-21, 23, 24, 40, 41]. Therefore, vital parts of a power plant, such as superheaters and water walls, are severely deteriorated by the corrosion processes that occur at high temperatures in such environments.

Table 1: Approximate flue gas composition (volume %) in waste-, biomass- and coal-fired boilers [9-13, 42, 43].

Fuel	O_2 (%)	H_2O (%)	SO_2 (ppm)	HCl (ppm)	KCl + NaCl (ppm)
Coal	~ 4-5	~ 4-16	~ 400-1200	~ 10-50	-
Biomass	~ 5-10	~ 10-20	~ 0-70	~ 25-1000	~ 5-50
Waste	~ 5-11	~ 10-20	~ 0-150	~ 250-1300	< 120

3. Materials

3.1. Steels

Steels are solid solutions of iron (major element) and carbon (minor element). Their well-known reputation comes from the addition of a small amount of carbon to iron. Pure iron is a ductile material with three possible crystal structures: ferrite (α), which has a body-centered cubic (bcc) structure; austenite (γ), which has a face-centered cubic (fcc) structure; and δ, which is a body-centered cubic.

When adding small amounts of carbon to iron, the movement of dislocations within the crystal structure are limited and the material becomes less ductile. Carbon therefore plays the role of a hardening agent. Consequently, the mechanical properties of the material are improved, such as hardness, yield strength, or tensile strength [44].

Besides carbon, other elements can be added in order to customize the final properties of the steel and favor the stabilization of a phase. For example, adding titanium, chromium, molybdenum, or aluminum will stabilize the ferritic phase at room temperature, while adding cobalt, manganese, nickel, carbon or silicon will stabilize the austenitic phase at room temperature. The stabilization of the phases is due to the alloying elements sharing the same crystal structure with one of the corresponding crystal structures of iron. The addition of alloying elements also contributes to the alteration of the final properties of the steel. From a corrosion aspect, chromium is the most important alloying element. It improves the corrosion resistance properties of steels by allowing them to form a chromium-rich oxide layer on top of the alloy, thus protecting the steels from further oxidation. Stainless steels exhibit such a property. The minimum chromium content of ferritic stainless steels is about 10.5-11 %, while it is 17-19 % for austenitic stainless steels [45]. Ferritic stainless steels and austenitic stainless steels are the most common steels used in industry. They have totally different properties due to their crystal structure, which make them suitable for specific applications. Another type of stainless steel used in the industry is the martensitic stainless steel which is a ferritic or austenitic stainless steel that has been quenched (rapid cooling). The quenching prevents carbon from forming cementite (Fe_3C) by locking the carbon within the crystal structure. This results in a crystal structure that is a highly strained body-centered tetragonal form called martensite. Martensitic stainless steels are well-known for their excellent mechanical properties due to the strengthening mechanism induced by shear deformation during the rapid cooling.

3.2. Nickel-based alloys

Nickel-based alloys are superalloys with nickel as the main constituent. Superalloys are intricate materials able to maintain some of their room-temperature physical and mechanical properties at elevated temperatures [46]. Nickel is a good candidate as a base for such alloys due to its high melting point (1453 °C), adequate corrosion resistance, and ability to dissolve, at least to some limited extent, various other metallic elements for strengthening the alloy and enhancing its corrosion properties. After heat treatment, a nickel-based alloy can be considered as a composite material consisting of several intermetallic phases bound by a metallic matrix. The most common phases are the matrix phase, gamma (γ); the intermetallic precipitate, gamma prime (γ'); and the carbides of the MC and $M_{23}C_6$ types, where M represents a metal [46].

As for steels, the addition of alloying elements results in a change in the final properties of the alloy:

- The addition of molybdenum, tungsten and chromium contributes to solid solution strengthening as well as carbide formation and stability. Chromium is also necessary for improving corrosion resistance.
- The addition of aluminum, titanium and niobium contributes to the formation of a fine dispersion of γ'-phase $Ni_3(Al,Ti,Nb)$.
- The addition of cobalt increases the solubility temperature of γ', therefore increasing the maximum temperature at which the alloy can be used.

Nickel-based alloys are usually used in load-bearing structures at elevated temperature. Hot sections of turbine engines are good examples of such challenging environments for a structural material. The ability of nickel-based alloys to retain their physical and mechanical properties at these high temperatures makes them ideal candidates for gas turbine applications.

However, even though nickel-based alloys exhibit great performance at temperatures near 1000 °C, they are prone to experience environmental attack due to the presence of the same alloying elements that provide their high-temperature strength. Surface attacks include oxidation, hot corrosion and thermal fatigue. To prevent such deterioration, nickel-based alloys are usually coated to improve their environmental resistance in highly demanding applications [47].

3.3. Materials investigated

This PhD thesis focused on several different materials, the chemical compositions of which are given in Table 2. The laboratory experiments involved the commercial alloys T91/P91, 304L, 347H, Sanicro 28, Inconel 625 and nickel-based model alloys containing 35-45 wt%. Cr. Nickel-based coatings (NiCr, NiAl and NiCrAlY) were also used in laboratory experiments, thermally sprayed over a low-alloyed steel 16Mo3. For the field studies, only the material 347H was considered among all the different materials tested as it was able to display significant results to be interpreted.

Table 2: Chemical compositions (wt.%) of the different materials investigated (First table: Cast alloys. Second table: coatings and substrate)

Material	Fe	Cr	Ni	Mn	Si	Mo	N	Cu	P	S	Al	Nb	Ti	O
T91/P91	Bal.	8.5	0.3	0.6	-	0.85	-	0.1	0.05	0.06	0.15	-	-	-
304L	Bal.	19.9	10	1.4	0.5	-	-	-	0.05	0.1	-	-	-	-
347H	Bal	17.7	10.1	1.6	0.57	-	-	-	0.03	0.002	-	0.64	-	-
Sanicro 28	Bal.	27.5	30.3	1.82	0.5	3.2	0.4	1.2	0.01	0.1	-		-	-
Inconel 625	1.9	23	Bal.	0.1	0.1	9.1	-	-	-	0.07	0.3	3.4	0.3	-
Ni35Cr4Nb	0.03	34.4	Bal.	-	0.03	-	0.002	-	<0.005	-	≤0.02	3.8	0.5	0.027
Ni45Cr4Nb	0.03	44.8	Bal.	-	0.05	-	0.001	-	<0.005	-	0.01	4.1	0.5	0.032

Material	Fe	C	Cr	Ni	Mn	Si	Mo	Al	Y	O
16Mo3	Bal.	0.15	0.01	-	0.5	0.3	0.3	-	-	-
NiCr	-	-	21.3	Bal.	-	-	-	-	-	0.1
NiAl	-	-	-	Bal.	-	-	-	5.7	-	0.2
NiCrAlY	-	-	21.2	Bal.	-	-	-	7.3	0.9	0.2

T91/P91:

The T91/P91 ferritic steel is mainly used for superheater and reheater in a power plant boiler, the main steam pipeline, and the heating furnace piping in the petrochemical industry. In this study, it was supplied by Livallco Stål AB. This steel displays outstanding heat-resistance and creep strength. It also has good resistance to corrosion and fatigue rupture at elevated temperatures, and it shows better thermal conductivity and thermal expansivity than austenitic steels.

304L:

The 304L grade steel is the most widely used commercial stainless steel and was supplied by Outokumpu. Its low carbon content (<0.03 wt.%) named by “L”, compared to its higher carbon content grade (<0.08 wt.%) gives it the ability to minimize the precipitation of chromium carbides. These carbides would deplete the chromium content within the steel, which would lead to a weaker corrosion resistance.

Sanicro 28:

This grade of austenitic stainless steel is often used in highly corrosive environments and was supplied by Sandvik. Both the chromium and nickel content are higher for this steel than for 304L. Sanicro 28 exhibits good resistance to stress-corrosion cracking (usually not the case for austenitic stainless steels) and to high-temperature corrosion.

Inconel 625:

This nickel-based alloy used for its high strength, excellent fabricability and outstanding corrosion resistance was provided by Harald Pihl. This alloy is well-known for its superior resistance to a wide range of corrosive environments as well as high-temperature oxidation and carburization. Due to its ease of fabrication, Inconel 625 is made into a variety of components for plant equipment. Applications requiring the combination of strength and corrosion resistance offered by this alloy are for example tubing, reaction vessels, heat exchangers, transfer piping, or over welding.

Nickel-based model alloys:

The two materials investigated differed mainly in chromium content. They were produced and compacted by hot isostatic pressing (HIP) of Ar atomized powder. The process was performed at 800 bar and 1323 K (1050 °C) for 3 hours in an argon atmosphere.

16Mo3:

This low-alloyed steel grade is a ferritic steel. It is widely used in powerplants, exhaust systems, and incineration plants. It is known for its good mechanical properties up to 500 °C and a low price compared to stainless steels. However, due to its low content of chromium, this alloy is unable to form a chromium-rich oxide layer. Thus, its corrosion resistance is due to an iron-oxide layer, which is less protective than chromium-containing alloys.

Coatings NiCr, NiAl and NiCrAlY:

These three commercial gas-atomized powders were supplied by HC Starck GmBH and were used for spraying on a 16Mo3 substrate. The powders had a particle size distribution of 45±22 µm.

4. Oxidation theory

4.1. Thermodynamics

When exposed to a gas-containing environment, non-noble metals are prone to be thermodynamically unstable. This results in the formation of oxides, carbides, nitrides, sulfides, or mixtures, depending on the composition of the surrounding environment [48]. Considering oxidation, the chemical reaction occurring between the metal M and oxygen O is as follows:

$$xM(s) + \left(\frac{y}{2}\right) O_2(g) \rightarrow M_xO_y(s) \qquad (1)$$

To determine if the formation of an oxide will occur spontaneously, it is possible to look at the variation of Gibbs free energy ΔG under constant pressure and temperature. The value of Gibbs free energy informs if the reaction will occur spontaneously or not:

- If ΔG < 0, the reaction will occur spontaneously.
- If ΔG > 0, the reverse reaction is favored.
- If ΔG = 0, the system is at equilibrium state, and no reaction is favored.

Gibbs free energy is expressed via the following equation:

$$\Delta G = \Delta G^0 + RTln(\frac{a_{M_xO_y}}{(a_M^x)\left(a_{O_2}^{\frac{y}{2}}\right)}) \qquad (2)$$

Where ΔG^0 is the standard Gibbs free energy, R is the universal gas constant, T is the temperature, and a is the activity of the products and reactants. The activities of solids are approximatively equal to 1, and the activities of gases are equal to their respective partial pressure. Thus, at equilibrium, the equation can be simplified as follows (when $\Delta G = 0$):

$$\Delta G° = RTln(p_{O_2}^{y/2}) \qquad (3)$$

The partial pressure of oxygen at equilibrium is called the equilibrium partial pressure or dissociation pressure. If the partial pressure of oxygen at a given temperature is higher than the equilibrium partial pressure of oxygen at the same given temperature, the formation of an oxide will be favored. Plotting the ΔG° of the formation of an oxide as a function of temperature can be summarized in the Ellingham diagram (Figure 4). This type of diagram is used to determine if an oxide will be reduced or if a metal will be oxidized. In essence, it shows if the formation of an oxide is thermodynamically favorable at a given temperature and partial pressure of oxygen. The lower the ΔG° is, the more stable the oxide is. The slopes of the lines are positive, which means that oxides become less stable as the temperature increases. However, the Ellingham diagram does not provide any information on the kinetics of the reactions (or growth rate).

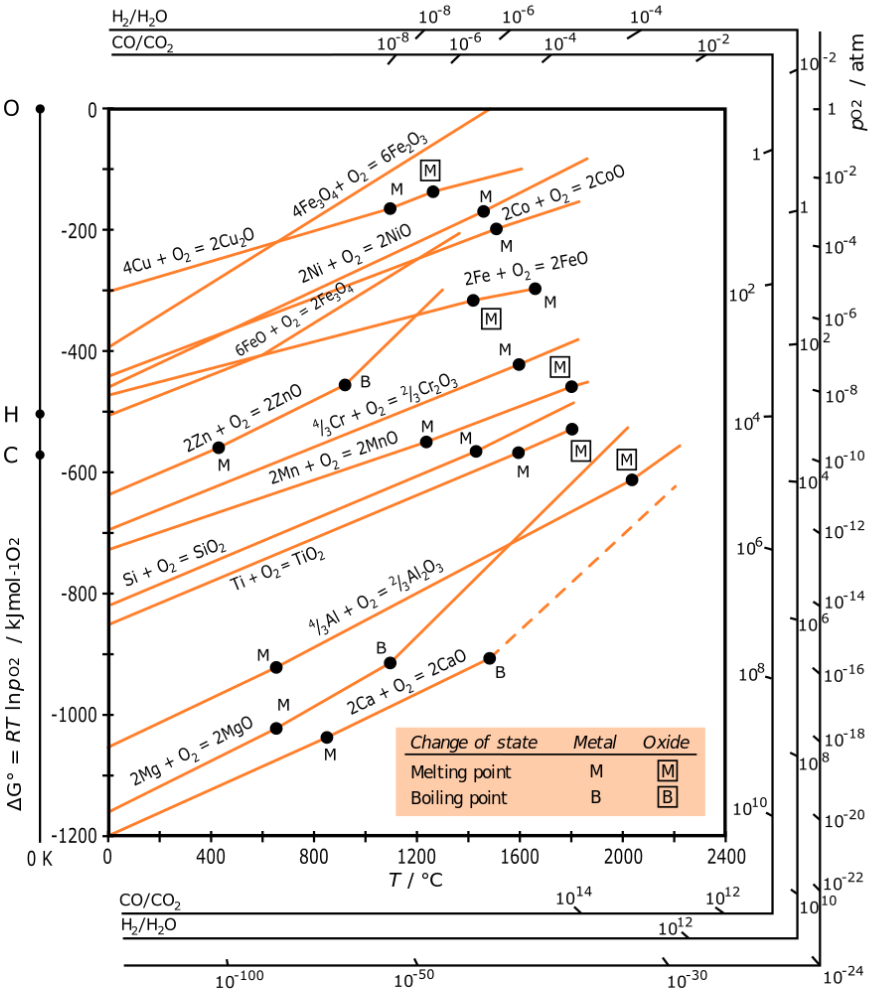

Figure 4: Ellingham diagram of various oxides [49].

4.2. Oxide formation

The oxidation process begins with the adsorption of oxygen on the surface of a metal. The oxygen adsorption and oxide formation steps are both affected by crystal defects on the surface of the material, surface preparation, surface orientation, as well as impurities in the metal and gas [48]. The oxide will keep growing until it covers the surface as a continuous scale. The growth of the oxide can then proceed only via solid-state diffusion of the reactants through the scale. However, crack formation within the oxide scale may expose the substrate to the environment, resulting in an increase in the oxidation rate. A schematic drawing in Figure 5 illustrates this process. The initial steps of oxidation are fast even at room temperature, however, once the continuous oxide scale has been formed, the oxidation rate decreases drastically as solid-state diffusion rates are very slow at room temperature. However, as the temperature increases, so do the diffusion rates.

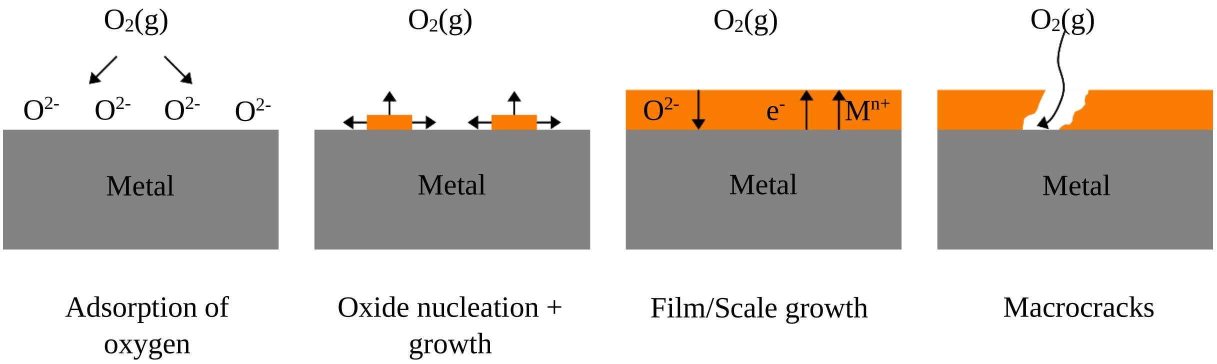

Figure 5: Schematic illustration of the oxidation process (after [48]).

4.3. Diffusion mechanisms

Once a continuous oxide scale has been formed, the growth of the scale occurs via the solid-state diffusion of reactants (atoms, ions, and/or electrons). The diffusion of these reactants depends on the presence of defects within the oxide. All metals and oxides have defects that can be categorized into three types: point defects (e.g. vacancies and interstitials), linear and planar defects (e.g. dislocations and grain boundaries) and bulk/volume defects (e.g. precipitates and voids). Based on the type of defect, the oxide scale can be divided into two types of compounds: stoichiometric and non-stoichiometric.

In stoichiometric compounds, the proportions of the elemental composition can be expressed with whole numbers [50]. Alumina (Al_2O_3) is an example of a compound close to ideal stoichiometry as it displays low-defect content, which makes the oxide formed a continuous and dense layer. In a stoichiometric crystal, electro-neutrality is maintained by the defects present in the oxide, which is the case for Frenkel and Schottky defects (see Figure 6) [48]. The Frenkel defect consists of a cationic vacancy and an interstitial cation, while the Schottky defect consists of a cationic vacancy and an anionic vacancy [48].

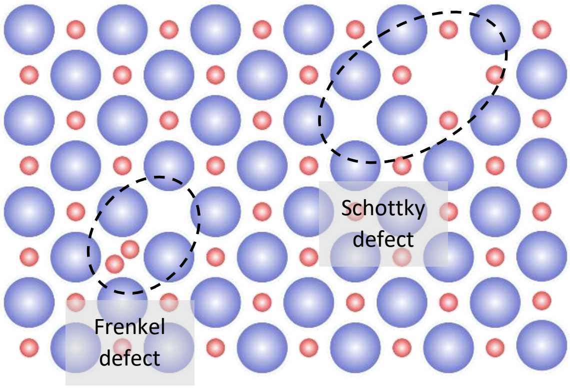

Figure 6: Schematic drawing of the Frenkel and Schottky defects(after [45]).

However, most oxides are non-stoichiometric and exhibit an excess or deficit of either oxygen or metal, e.g. FeO (wüstite) commonly written $Fe_{1-x}O$, where a deficit of metal is the main defect. The absence of stoichiometry results in the compound being considered as a semi-conductor. By definition, there are two types of semi-conductors [48]:

- The p-type semiconductor: electric conductivity is the result of the formation of electron holes caused by the removal of metal ions or the addition of oxygen ions. The charge is transferred by positive carriers.
- The n-type semiconductor: electric conductivity is the result of the formation of concentrations of electrons caused by the removal of oxygen ions or the addition of metal ions. The charge is transferred by negative carriers.

Such a categorization allows the prediction of the electrical properties of an oxide and, therefore, a better understanding of the diffusion mechanisms through the oxide. For example, FeO (wüstite) exhibits a deficit of metal, which is considered as a cation vacancy resulting in the charge being transferred by positive carriers, holes. The oxide is, therefore, a p-type semiconductor outward-growing.

Defects within the oxide also allow the transport of atoms or ions through the oxide scale, which is called diffusion. This phenomenon occurs in two different ways: lattice diffusion and short-circuit diffusion [48].

Lattice diffusion:

This type of diffusion occurs within the bulk material due to the presence of point defects leading to several diffusion mechanisms (Figure 7):

- The interstitial mechanism: The migration of an atom or ion at an interstitial site to a neighboring interstitial site. This mechanism has a higher probability of occurring when the interstitial ion or atom is smaller than the atoms located at the lattice sites.
- The vacancy mechanism: The migration of an atom or ion at a normal lattice site to a neighboring unoccupied lattice site. This results in a vacancy created where the atom or ion was previously located, which can be interpreted as a vacancy migration.
- The interstitialcy mechanism: The migration of an interstitial ion or atom to a normal lattice site, which causes the original ion or atom at that lattice site to migrate to a neighboring interstitial site.

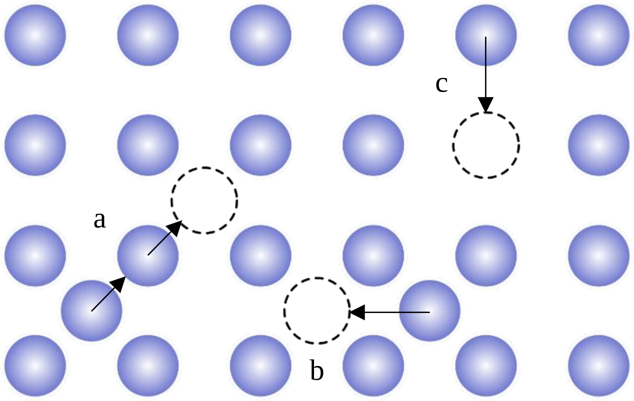

Figure 7: Representation of a) interstitialcy diffusion, b) interstitial diffusion, and c) vacancy diffusion (after [51]).

Short-circuit diffusion

This type of diffusion takes place within two-dimensional defects, such as grain boundaries and dislocations. These defects can be considered as fast transport paths through the oxide, as the diffusion coefficients are higher than lattice diffusion. This difference in diffusion coefficient is due to the activation energies for short-circuit diffusion being 0.5-0.7 times those for lattice diffusion [48]. Therefore, short-circuit diffusion is the dominant diffusion mechanism at low temperatures, which is considered to be below 0.8 times the melting temperature of an alloy/metal [52]. Increasing the temperature of the surrounding environment increases the contribution of lattice diffusion while reducing the contribution of short-circuit diffusion. As the temperature rises until it reaches values close to the melting temperature of the alloy/metal, the contribution of short-circuit diffusion diminishes until it becomes negligible. However, in this thesis, short-circuit diffusion was considered as the investigations were performed at 600 °C or below.

The diffusion coefficient D is temperature-dependent and obeys an Arrhenius relationship as follows:

$$D = D_0 \exp\left(-\frac{E_a}{RT}\right)\ [\mathrm{m^2/s}][53] \qquad (4)$$

Where D_0 represents a temperature-independent constant called the frequency factor or pre-exponential factor, E_a is the activation energy of the diffusion process, R is the universal gas constant, and T is the temperature.

4.4. Oxidation kinetics

Two aspects must be considered when looking at a reaction:

- Whether the reaction or the reverse reaction is favored. This information is provided by thermodynamics.
- The rate of the reaction. This information is given by kinetics.

In oxidation, kinetics relates to how fast a metal or an alloy oxidizes. The kinetics of oxidation can be illustrated by plotting the mass change in a sample as a function of time. This results in a plot called mass gain curve. The mass gain is caused by oxygen uptake during oxide formation. There are three main ideal oxidation rate behaviors illustrated by three different mass gain curves: linear, parabolic, and logarithmic (Figure 8). However, a combination of these behaviors is normally required in order to explain the mass gain curves observed in experimental studies. Breakaway behavior is a good example of this phenomenon due to the interaction of the protective oxide scale (primary protection formed at early stages of the oxidation process) with the environment, such as the formation of potassium chromates (see Section 6.2) or the spallation of the oxide scale, which leads to the breakdown of this primary protection and the growth of a faster growing oxide scale (secondary protection).

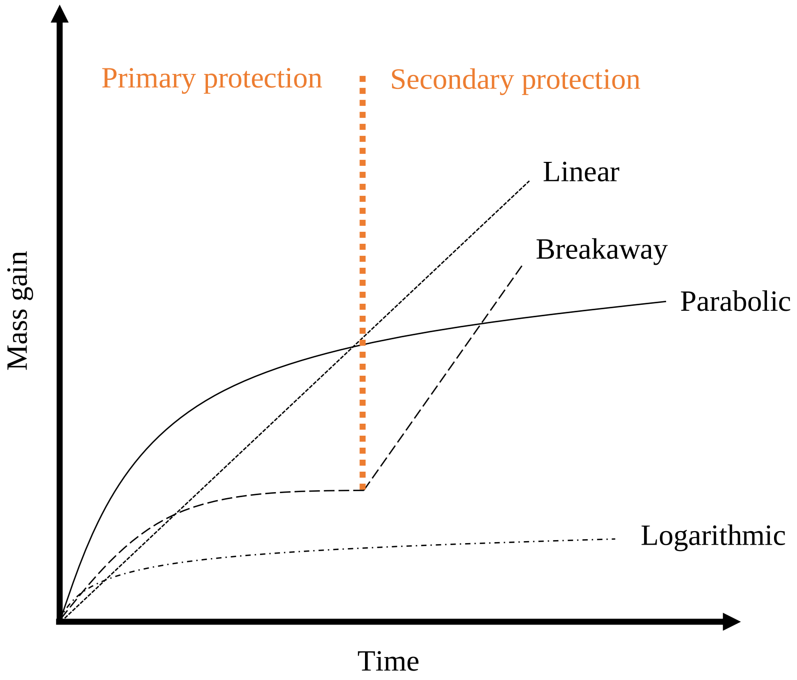

Figure 8: Various kinetic laws of metal oxidation. The primary and secondary protection areas are illustrated only for breakaway behavior.

4.4.1. Linear behavior

Linear behavior exhibits a constant oxidation rate. This is due to the rate-limiting step being a surface or a phase boundary process or reaction, such as the adsorption of oxygen on a metal surface. It is common to observe this behavior at early stages of the oxidation process or in thin or highly porous oxides [48].

This behavior can be expressed by the following equation:

$$x = k_l t \tag{5}$$

where x is the oxide thickness, k_l is the linear rate constant, and t is the time.

4.4.2. Parabolic behavior

Parabolic behavior is the most common behavior observed for metals at high temperature. The rate-limiting step is the transport of ions (or electrons) through an oxide scale. As the thickness of the oxide scale increases, the diffusion rates decrease, resulting in a lower oxidation rate.

This behavior can be expressed by the following equation formulated by Carl Wagner [54]:

$$x^2 = k_p t + C \tag{6}$$

where x is the oxide thickness, k_p is the parabolic constant, t is the time, and C is the integration constant. Carl Wagner based this model on the following assumptions:

- The oxide formed is compact and adherent.
- The transport of ions and electrons is the rate-limiting step.
- Equilibrium is established at both the metal/oxide and oxide/gas interfaces.
- Equilibrium is also established within the oxide.
- The oxide shows only small deviations from stoichiometry.
- Oxygen solubility within the metal can be neglected.

4.4.3. Logarithmic behavior

Logarithmic behavior is commonly observed at low temperatures, generally below 300-400 °C [48]. A fast oxidation rate can be seen in the early stages of the corrosion attack, followed by a drastic decrease in the oxidation rate. The rate-limiting step is still being discussed, but some possible explanations have been suggested, e.g. the transport of ions or electrons due to electric fields [48].

This behavior can be expressed by the following equation:

$$x = k_{log} \log(t + t_0) + A \tag{7}$$

where x is the oxide thickness, k_{log} is the logarithmic rate constant, t is the time, and A is a constant.

4.4.4. Breakaway behavior

Breakaway behavior occurs when an alloy or metal exhibiting either a parabolic or logarithmic behavior loses its primary protection (the protective oxide layer) through the spallation of the oxide layer, cracks within the layer, or the breakdown of the protective layer via interaction with the environment. This results in a fast-growing secondary protection (a fast-growing oxide) leading to accelerated corrosion, as seen by the sudden increase in mass gain. The fast-growing oxide dictates the corrosion behavior of the alloy from that point on. Thus, the oxide layers formed as a result of the breakaway can be labelled as secondary protection.

5. Corrosion products

The interaction between the materials investigated and their surrounding environment led to the formation of corrosion products. Understanding the properties of the corrosion products is relevant in order to increase knowledge about corrosion mechanisms when metals or alloys are exposed to certain environments. The corrosion products mentioned in the following section were observed in both boiler and laboratory environments.

As the materials investigated were different in chemical composition and microstructure, differences in the corrosion mechanisms and the oxide scales formed were observable as well.

5.1. Oxides in high-temperature corrosion

Oxides play a major role in the corrosion resistance of metals and alloys. Depending on the composition, oxides differ in ion diffusivities, crystal structure, and, consequently, corrosion resistance. An oxide is considered protective when it exhibits the following properties [55]:

- Good adhesion to the substrate
- Dense and continuous layer
- Slow growth rate
- Similar thermal expansion coefficients between the substrate and the oxide
- Low electrical conductivity and low diffusion coefficients for metal ions and oxygen
- High melting point
- High-temperature plasticity

The crystal structure of many oxides formed at high temperatures mainly consists of cubic and hexagonal close-packed oxygen ions, with metal ions located at interstitial sites. The properties of the most important corrosion products investigated herein are described below [48]:

Wüstite – $Fe_{1-y}O$

Wüstite exhibits a rock salt structure. This crystal structure consists of iron and oxygen atoms that form sub-lattices of a cubic close-packed type. It is only stable above 570 °C and in low oxygen-activity environments. Wüstite is a highly non-stoichiometric oxide due to metal vacancies, since the non-stoichiometry varies between $Fe_{0.85}$ and $Fe_{0.95}$. Based on previous observations, wüstite is a p-type semiconductor. The presence of many defects results in high mobility for ionic transport [48]. The presence of chromium in an alloy hinders the formation of wüstite.

Magnetite – Fe_3O_4

Magnetite has an inverse spinel structure at and below room temperature. The distribution of the divalent and trivalent iron ions becomes randomized between the octahedral and tetrahedral sites at higher temperatures. At high oxygen activity, magnetite is metal-deficient, which makes it a p-type semiconductor. However, at low oxygen activity, metal excess becomes dominant, making magnetite an n-type semiconductor [48].

Hematite – Fe_2O_3

Hematite has a corundum structure, where the oxygen atoms form a slightly distorted hexagonal close packing, in which two-thirds of the octahedral sites are occupied by iron atoms [48].

The non-stoichiometry of hematite is small with oxygen deficiency, which makes it an n-type semiconductor in the range of 650-800 °C, and a p-type semiconductor at higher temperatures.

General corrosion properties of iron oxides

The formation of these three oxides depends on oxygen activity and temperature. From a corrosion point of view, wüstite is the least protective oxide among the three, magnetite comes in second place, and hematite is the most protective.

Eskolaite – Cr_2O_3

Eskolaite, or chromia, exhibits a corundum structure and is considered to be a p-type semiconductor. Eskolaite is a slow-growing and dense oxide that has a small amount of defects compared to iron oxides, which makes it eligible as a protective oxide [48]. The formation of eskolaite is the reason why chromium is added to steels to obtain corrosion-resistant steels called stainless steels.

General corrosion properties of Cr-containing oxides

Among the stainless steels investigated in this study, eskolaite usually forms a mixed solid solution with hematite, resulting in $(Fe_{1-x}Cr_x)_2O_3$.

Spinel-type solid solution – $(Fe,Cr,Ni)_3O_4$

Oxides based on iron, chromium, and nickel may form solid solutions with a spinel-type structure. This is a complex structure that consists of cubic close-packed oxygen atoms and metal ions that occupy the tetrahedral and octahedral sites. Divalent cations (e.g. Fe, Zn, Ni, Mn, Mg) are located at the tetrahedral sites, and the trivalent cations (e.g. Fe, Cr, Al) are located at the octahedral sites. The composition of a spinel-type solid solution depends on the amount of those elements as well as the oxygen activity at the oxide/metal interface.

General corrosion properties of spinel-type oxides

It has been shown that in the case of 304L at 600 °C in a corrosive environment, the spinel oxide region formed is more complex and consists of regions of spinel oxide and regions of mixed metal/oxide. This characteristic microstructure may influence the properties/oxidation in the following ways [27]:

- A network of interfaces between oxide/metal and oxide/oxide is created and may act as fast transport paths for ions.
- Regions rich in iron and nickel may become voids after functioning as sources of ions for the outward growing oxide [56]. The voids created within the spinel may contribute and cause spallation.

Alumina – Al_2O_3

Alumina exists mostly in two allotropic forms: α-Al_2O_3 and γ-Al_2O_3. α-Al_2O_3 has a corundum structure with oxygen atoms forming a hexagonal close packing, where two-thirds of the octahedral sites are occupied by aluminum atoms.

γ-Al_2O_3 exhibits a cubic structure and usually forms below 900 °C and is a transient oxide (not thermodynamically stable). After 900 – 1000 °C, γ-Al_2O_3 changes to α-Al_2O_3, the only thermodynamically stable form of alumina. α-Al_2O_3 has a high degree of stoichiometry due to its high lattice energy and large bandgap, resulting in a very low concentration of defects [48]. Consequently, the diffusion rates of ions through the oxide are low, leading to a slow growing oxide. α-Al_2O_3 therefore exhibits high corrosion resistance.

Nickel oxide – $Ni_{1-\gamma}O$

NiO is the principal oxide of nickel [57]. Similar to wüstite it exhibits a rock-like structure where the metal ions are located at the octahedral sites and oxygen ions at the lattice sites. NiO is non-stoichiometric due to the presence of metal vacancies. It can be therefore considered as a p-type semiconductor [58].

5.2. Metal chlorides

In a chlorine-containing environment, such as alkali chlorides (KCl, NaCl…), hydrochloric acid, or chlorine, metals can react and form metal chlorides (e.g. $FeCl_2$, $FeCl_3$, $CrCl_2$, $CrCl_3$, and $NiCl_2$). Thermodynamic phase stability diagrams of the systems Fe-O_2-Cl_2, Cr-O_2-Cl_2, and Ni-O_2-Cl_2 at 600 °C are shown in Figure 9. These diagrams show that metal chlorides are stable when oxygen activities are low, which corresponds to the metal/oxide interface conditions where they can be detected [59].

It is believed that metal chlorides play an essential role in severe corrosion according to the “active oxidation” or the chlorine cycle mechanism [13, 16, 60-65]. The details of this mechanism are described in 6.3.

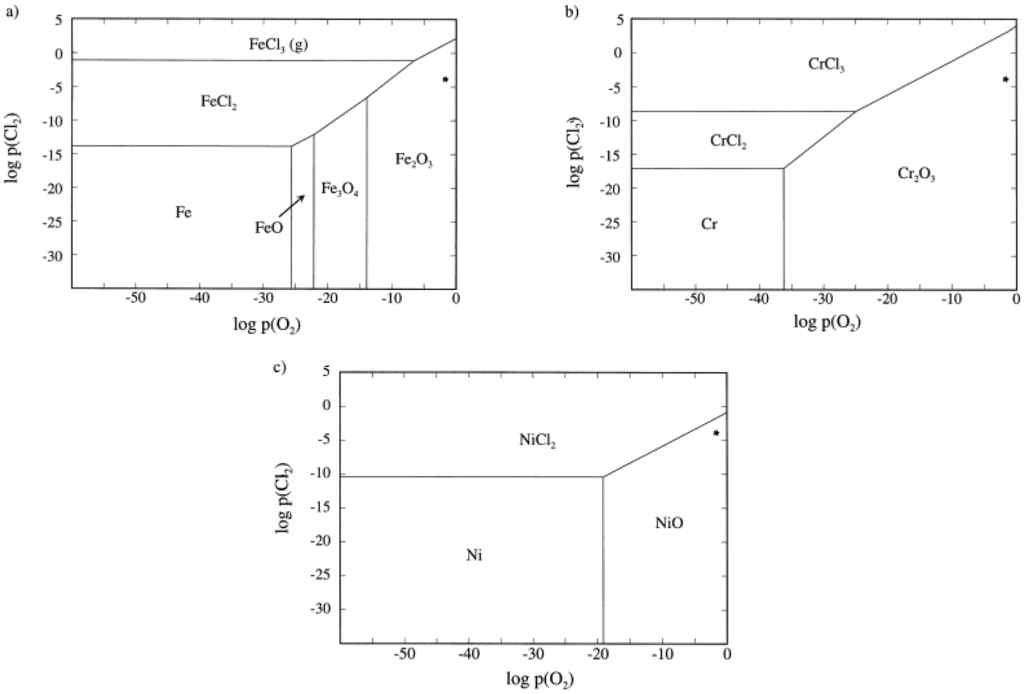

Figure 9:Thermodynamic stability diagrams of the systems Fe-O_2-Cl_2 (a), Cr-O_2-Cl_2 (b), and Ni-O_2-Cl_2 (c) at 600 °C [59].

6. Corrosion mechanisms

Understanding the corrosion mechanisms that occur between an alloy and its surrounding environment is crucial for the development of suitable corrosion mitigation solutions. The corrosion resistance of stainless steels, widely used as superheaters in power plants, is primarily attributed to the presence of chromium in their composition. This results in the formation of a chromium-rich oxide scale on top of the substrate material. This oxide scale is the first protective feature (primary protection) that separates and protects the substrate from the environment.

However, despite this first protective oxide scale, superheaters have exhibited severe corrosion attacks when fossil fuels replaced with renewable fuels such as biomass and waste. The nature of the fuel is the reason behind the deterioration of the protective oxide scale and of the material. This deterioration (breakaway) is caused by the release of many corrosive compounds during the combustion of renewable fuels.

In the following sections, the mechanisms inducing severe corrosion attacks in chromium containing materials are described as all materials investigated in this study rely on a chromium-rich oxide for corrosion resistance.

6.1. Chromium evaporation

The corrosion resistance of stainless steels relies on the formation of a chromium-rich oxide scale (primary protection) on top of the bulk material. This layer is formed when the stainless steel is exposed to a dry atmosphere containing typically 5% O_2 at 600 °C for 24 hours [22]. Introducing water vapor into the environment may deteriorate the protective scale by the reaction below:

$$Cr_2O_3(s) + 2H_2O(g) + 3/2O_2(g) \rightleftharpoons 2CrO_2(OH)_2(g) \quad (8)$$

The formation and evaporation of chromic acid may, therefore, deplete the chromium-rich oxide in chromium. However, the protectiveness of the chromium-rich oxide remains until the depletion of chromium becomes too substantial. This may lead to breakaway corrosion where an iron-rich oxide scale (secondary protection) begins to grow rapidly, instead of the chromium-rich slow-growing scale.

The supply of chromium occurs via grain boundary diffusion at 600 °C, which explains the morphology of the corrosion products observed, for example, after exposure to O_2 and H_2O for 168 hours, as shown in Figure 10 [66]. The surrounding area is more protected than the center of a grain due to the fast transport of chromium at the grain boundaries. This explains the island-like shape of the growing oxides on top of the substrate, where the iron oxide becomes thicker towards the center of the grain and thinner towards the grain boundaries. Figure 10b) shows the cross-section of such an island and its architecture, which consists of an outward-growing scale, hematite (Fe_2O_3), and an inward-growing scale that is a spinel-type oxide ($(Fe,Cr,Ni)_3O_4$) [66]. This effect of water vapor on chromium containing alloys has been intensively investigated in many studies [66-70].

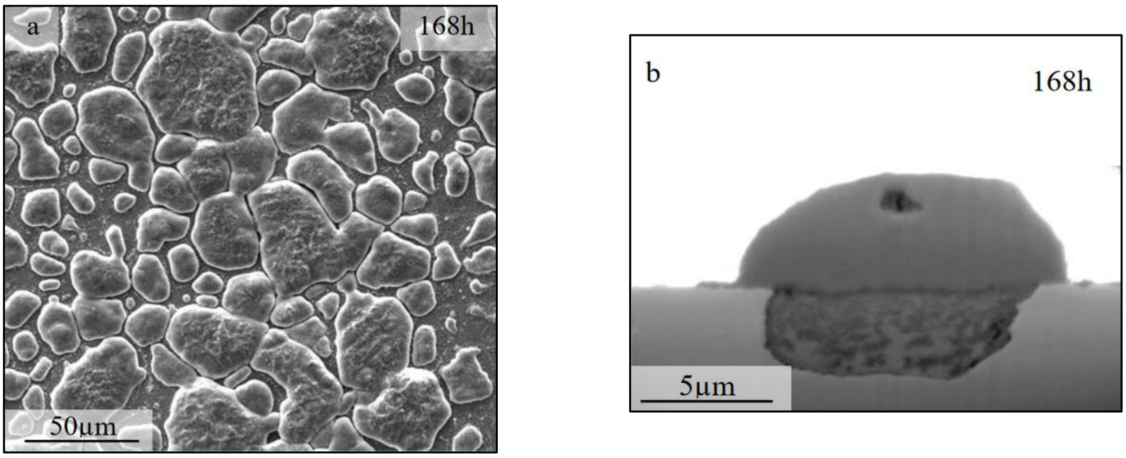

Figure 10: a) SE images of 304L samples exposed to 5% O_2 and 40% H_2O for 168h at 600 °C and b) BSE images of FIB cross-sections of an oxide island [66].

6.2. Alkali chromate formation

The protective chromium-rich oxide scale can also be deteriorated by another mechanism called alkali chromate formation. It has been shown that the breakaway of the protective layer occurs in the presence of alkali compounds [22-24]. This phenomenon occurs due to the reaction between the alkali ion and the chromium-rich oxide, which leads to the depletion of chromium from the primary protection:

$$Cr_2O_3(s) + 4KCl(s) + 2H_2O(g) + 3/2O_2(g) \rightleftharpoons 2K_2CrO_4(s) + 4HCl(g) \quad (9)$$

If the depletion of chromium from the primary protection becomes too substantial, breakaway of the protective layer occurs, leading to the growth of an iron-rich fast-growing oxide scale (secondary protection). The loss of the primary protection followed by the rapid growth of the secondary protection is a rather fast process. Thus, the overall corrosion resistance of stainless steels in alkali-rich environments is often dictated by the properties of the secondary protection. This is a recurring problem in biomass- and waste-fired boilers as the renewable fuels used contain a considerably higher amount of alkali chlorides than fossil fuel [71-73]. The combustion of biomass and waste releases these alkali chlorides in a volatile form, which is part of the flue gas that reaches the superheaters. A typical flue gas composition of biomass- and waste-fired boilers is given in Table 1 [9-13, 42, 43].

6.3. Active oxidation or chlorine cycle

Active oxidation (or the chlorine cycle) is a mechanism that was first suggested by McNallan [62] and was extended by Grabke [16]. It involves the transport of chlorine (Cl_2) from the oxide/gas interface to the metal/oxide interface. Chlorine is considered to be more aggressive than HCl during short-time exposures [60]. The presence of chlorine is obtained through the reaction of alkali chlorides with the oxide scale (considering a chromium containing alloy), or through the oxidation of HCl (the Deacon process) [16]:

$$4NaCl(s) + Cr_2O_3(s) + 5/2O_2(g) \rightleftharpoons 2Na_2CrO_4(s) + 2Cl_2(g) \quad (10)$$

$$2NaCl(s) + Fe_2O_3(s) + 1/2O_2(g) \rightleftharpoons Na_2Fe_2O_4(s) + Cl_2(g) \quad (11)$$

$$2HCl(g) + 1/2O_2(g) \rightleftharpoons Cl_2(g) + H_2O(g) \quad (12)$$

When chlorine gas penetrates the oxide scale and reaches the metal/oxide interface, it reacts with the substrate and forms corresponding chlorides. As the oxygen pressure is supposedly low at this interface, the formation of metal chlorides is favorable:

$$Fe(s) + Cl_2(g) \rightleftharpoons FeCl_2(s) \quad (13)$$

At the temperatures of investigation (500-600 °C), the equilibrium vapor pressure of metal chlorides is considerable (e.g. $p(FeCl_2) = 4.10^{-5}$ bar at 500 °C [16]), which results in their continuous evaporation and diffusion towards the gas/oxide interface through the oxide scale via cracks and pores. The gradient of oxygen pressure between the bulk material and the environment oxidizes the metal chlorides to Fe_3O_4 and/or Fe_2O_3 in regions with a higher oxygen pressure (towards the environment):

$$3FeCl_2(g) + 2O_2(g) \rightleftharpoons Fe_3O_4(s) + 3Cl_2(g) \quad (14)$$

$$2FeCl_2(g) + 3/2O_2(g) \rightleftharpoons Fe_2O_3(s) + 2Cl_2(g) \quad (15)$$

Based on the reactions 13 and 14, the released chlorine may either go through the same process described previously (chlorine cycle) or return to the surrounding atmosphere.

Active oxidation is suggested to explain the acceleration of corrosion in the presence of chlorine-containing species. However, the approach remains theoretical and several aspects of the suggested mechanism exhibit debatable elements such as the diffusion of $Cl_2(g)$ through the oxide scale. It has been observed that active oxidation starts with almost no incubation time after the introduction of HCl or alkali chlorides onto the sample. Therefore, the authors ([16]) have suggested that chlorine must use fast diffusion paths such as cracks and pores. However, if a molecule of chlorine is able to reach the interface via molecular diffusion through these cracks and pores, then the molecule of oxygen (242 pm) should also be able to do so as it is smaller than $Cl_2(g)$ (396 pm). Moreover, the possibility for the oxygen molecule to travel through the oxide scale and reach the metal/oxide interface would decrease the probability of metal chlorides forming as the gradient of oxygen partial pressure through the oxide scale would change. The outward diffusion of metal chlorides is also debatable as metal chloride molecules are larger than $Cl_2(g)$. Another issue is the prediction that metal chlorides must be located at the metal/oxide interface where oxygen activity should be sufficiently low. However, chlorine-rich areas have also been found in the outer part of the scale [65]. For these reasons, other approaches are being investigated such as the one discussed in 6.4.

6.4. Electrochemical approach

This approach [61, 74, 75] considers a flux of anions, cations, and an electronic current as the diffusion mechanism instead of the transport of gaseous chlorine species through an oxide scale. The formation of Cl^- is suggested to occur on the surface of the oxide via the reduction of $Cl_2(g)$ as shown below, and the formation of electrons via metal oxidation:

$$Cl_2(g) + 2e^- \rightarrow 2Cl^-(ads) \qquad (16)$$

$$M(s) \rightarrow M^{n+} + ne^- \qquad (17)$$

Chloride ions may also be produced from HCl and alkali chlorides [76]:

$$2HCl(ads) + 1/2O_2(ads) + 2e^- \rightarrow H_2O(g) + 2Cl^-(ads) \qquad (18)$$

$$2KCl(s) + 1/2O_2(g) + H_2O(g) + 2e^- \rightarrow 2KOH(g) + 2Cl^-(ads) \qquad (19)$$

Considering this approach, the present authors have suggested that chloride ions have high mobility on the surface of the oxide. The grain boundaries of the oxide can be considered as internal surfaces that allow chloride ions to behave in the same way as on a surface [77]. This enables access to the metal/oxide interface and, consequently, the formation of metal chlorides. However, it has been reported that metal chlorides could also be located within the oxide scale [61], which agrees with the findings that metal chlorides are not only located at the metal/oxide interface [65]. Their position is determined by the speed of the inward and outward transports of chloride ions and cations, respectively.

7. Analytical techniques

To gain full understanding of the corrosion mechanisms, it is necessary to use a wide range of analytical techniques. The investigation of the exposed samples from the field and the laboratory were performed using several characterization tools. The following sub-sections describes the different techniques used in this thesis.

7.1. Scanning Electron Microscope (SEM)

Microscopy is a powerful technique of characterization for corrosion science that provides information on grain size, morphology, or chemical compositions. This technique relies on the interaction between an incident beam of electrons and the atoms of a sample. Several types of interactions can occur, generating different types of products of interaction, such as Auger electrons or backscattered electrons, depending on the depth reached in the sample by the incident beam, see Figure 11. The depth depends on the accelerating voltage of the electrons; the higher the accelerating voltage, the deeper the electrons can interact.

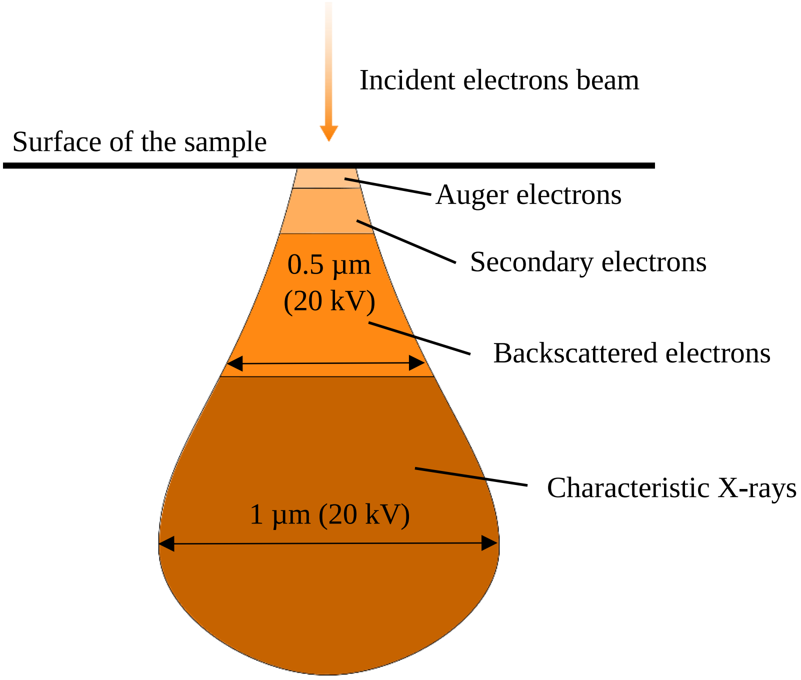

Figure 11: Schematic illustration of the interaction volume and the products of interaction.

- <u>Products of interaction for the signals used in this thesis</u>

<u>Secondary electrons (SE)</u>

This type of electron is produced via inelastic scattering interactions between the incident electron and an electron of the K shell of the atom. The incident electron ejects the electron located at the K shell of the atom, producing a so-called “secondary electron” with lower energy (<50 eV). These electrons are mainly produced near the surface, thus, providing information about the surface such as topography and morphology [78]. In this thesis, SE imaging with an accelerating voltage of 10 kV was mostly used when performing 3D serial sectioning for 3D tomography (see 7.3).

Backscattered electrons (BSE)

This type of electron comes from elastic scattering interactions between the incident electron and the nucleus of an atom. As heavy elements have a higher atomic number, therefore occupying more space, the number of electrons reflected (backscattered) is higher than for light elements. Thus, heavy elements appear brighter (higher amount of BSE detected), and light elements appear darker in SEM images using BSE. Backscattered electrons are used to detect the different phases caused by the differences in chemical composition. An accelerating voltage of 10kV was used for standard BSE imaging and 20 kV was used for BSE imaging in the chemical analyses of this thesis. At 20 kV, this resulted in a resolution of approximatively 0.5 µm (see Figure 11)[78].

Characteristic X-rays for Energy Dispersive X-ray Spectroscopy (EDX)

Another possible interaction is the excitation of an electron from the inner shell of an atom, resulting in its ejection and the creation of an electron hole. The atom is subsequently in an excited state, which is resolved by an electron from the outer shell filling the vacant place. The difference in energy between the outer shell (higher energy) and the inner shell produces an X-ray. As the energy difference between the two shells produces characteristic X-rays of an element, it is possible to establish a spatial distribution of the elements and estimate their relative abundance in the area of interest [78].

The SEM used in this study was an FEI Quanta 200 equipped with an Oxford Instruments X-Max^N 80EDX detector. The accelerating voltage used for imaging was 10 kV (~2-3 nm resolution for SE and ~400-500 nm resolution for BSE), and 20 kV was used for EDX analysis (~1 µm spatial resolution and ~130 eV energy resolution).

7.2. Focused Ion Beam (FIB)

In the field of material science, Focused Ion Beam milling (FIB) is widely used to prepare site-specific cross-sections, metal deposition, patterning, thin FIB lamella preparation for Transmission Electron Microscope (TEM), in-situ research with ion beam, and milling for advanced 3D characterization. The FIB is similar to SEM, which utilizes a focused beam of electrons while a FIB uses a Liquid Metal Ion Source (LMIS) (typically gallium ions). Dual-beam machines, FIB-SEM that incorporate both a FIB and SEM in a single system, are common nowadays. The principles of imaging with ions, site-specific milling, and metal deposition are described below:

- Imaging: upon heating the LMIS reservoir, ions flow towards the tip of a tungsten needle where they are extracted by applying an electric field. The extracted ions are then accelerated and converged into an ion column (52° to electron beam) to produce a focused ion beam. The interaction between the incident ion beam and the sample generates secondary electrons and secondary ions that are collected for image formation.
- Site-specific milling (etching): contrary to a SEM, the FIB technique is destructive to the sample. When high-energy gallium ions are bombarded onto a sample surface, the atoms present on the surface will be sputtered, hence, leading to material removal. This phenomenon is utilized to perform etching at the micro or nanoscale.
- Metal deposition: FIB allows the electron and ion beam assisted deposition of metal to protect the sample surface from destructive ion beam-induced damage [79]. The deposition occurs by the introduction of a precursor gas (platinum-containing gas in this work) into a vacuum chamber. The precursor gas is then decomposed by the beam into volatile and non-volatile components. The non-volatile component, e.g. platinum will remain on the surface as a deposition.

A schematic illustration in Figure 12 illustrates the three applications described previously.

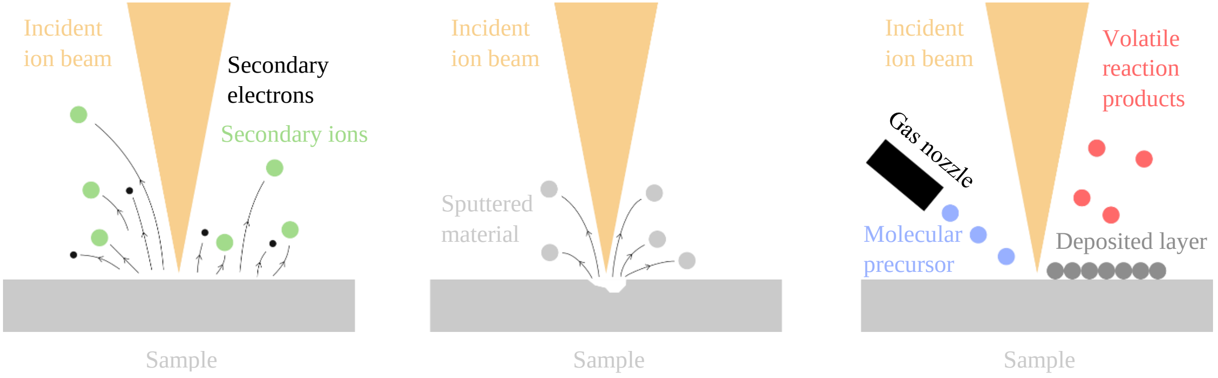

Figure 12: Schematic illustration showing the interactions between the sample and the ion beam for (left) FIB imaging, (middle) etching, and (right) metal deposition.

TEM sample preparation was carried out with FIB milling to prepare thin lamella with a thickness around 100 nm. Figure 13 illustrates the different steps for the preparation of TEM samples using FIB.

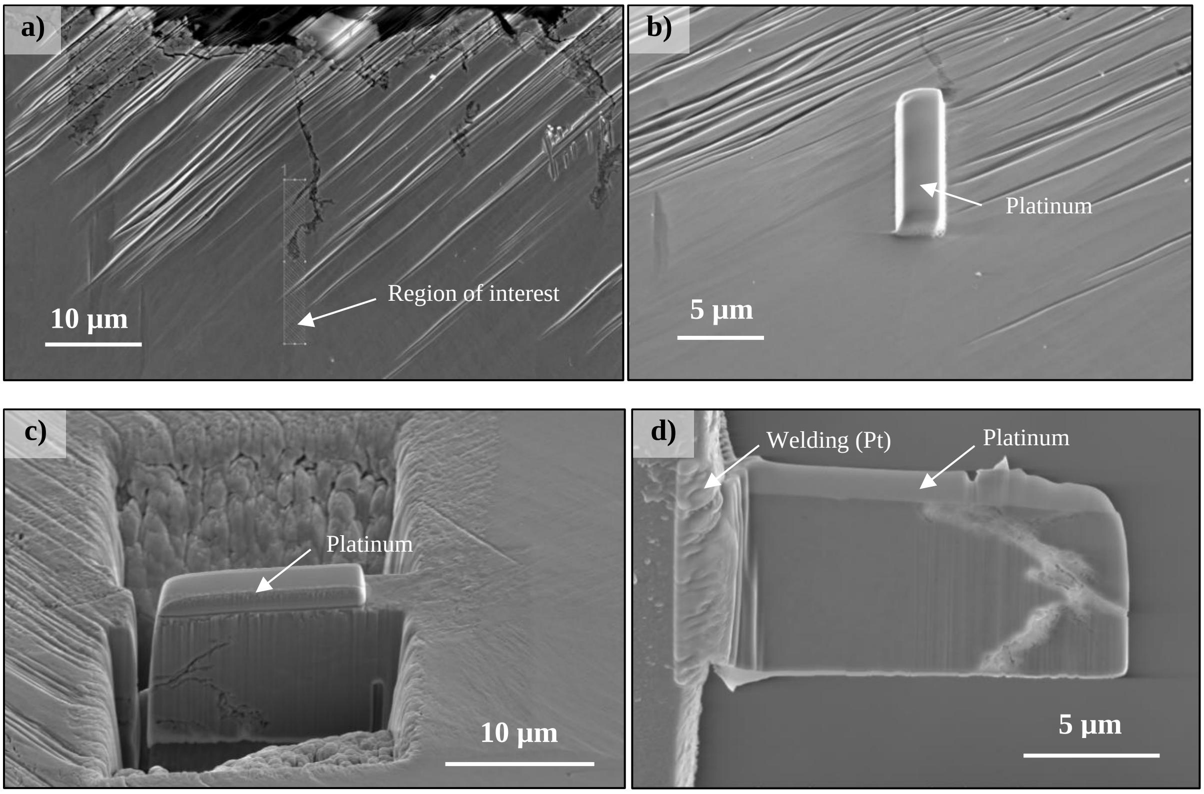

Figure 13: Micrographs illustrating the different steps for TEM lamella preparation using FIB. a) Selection of the region of interest marked with rectangle (0° tilt), b) region of interest after platinum deposition (52° tilt), c) region of interest after milling and U-cut (52° tilt), and d) lamella welded to a half Cu-TEM grid after lift-out (52° tilt). Pictures provided courtesy of Dr. Imran Hanif.

Two different dual beam FIB-SEM machines were used in this thesis. The TEM lamellas were prepared by Dr. Imran Hanif using FEI Versa3D FIB-SEM. First, a protective layer of platinum was deposited with an operating voltage of 30 keV and a current of 0.3 nA. Second, trenches were made using the high current of 30 nA for rough milling. Third, cleaning cross-section pattern (fine milling) was performed using a current of 7 nA. Fourth, the sample was lifted-out with an Omniprobe system. After the lift-out and welding of the lamella to a half Cu grid, the lamella was thinned down with high voltage and low currents starting from 30 keV and 1 nA. The operating voltage and current were subsequently reduced until 8 keV and 30 pA respectively. Low voltage and low current milling were necessary to remove the ion beam-induced surface damage. Lastly, the thin lamella was plasma-cleaned using Fischione 1020 Plasma Cleaner system at 2 keV for 5 minutes. Images were acquired with the integrated SEM using an accelerating voltage of 10 keV.

7.3. 3D tomography

Serial sectioning (or slicing) was performed in order to reconstruct in 3D areas of interest. A schematic illustration of the principle is shown in Figure 14. This was achieved by using a Tescan GAIA3 FIB-SEM system. The work was conducted at an operating voltage of 30 keV and a current of 2.3 nA for platinum deposition, 10 nA for rough milling and 7 nA for fine milling (used for slicing). Images were acquired with the integrated SEM using an accelerating voltage of 10 keV and SE detector. The images were then compiled as an image stack and processed in FIJI (Image J) using the plugin StackReg with "Translation" as the transformation option. The result of the image processing was a stack of well-aligned images in .tiff format.

3D Tomography was performed using the software Dragonfly version 4.1.0.647. The image stack was opened and processed directly within the software. The process, which aims at distinguishing different features of a dataset (image stack), is called segmentation. Several methods for segmentation exist[80, 81] and in this study the method designated "thresholding" was used.

Thresholding is one of the simplest approaches to segmentation and is based on intensity levels of pixels. The corrosion products observed in this experiment are well-known (such as voids or internal oxidation), while the range of intensity levels for thresholding was adapted to isolating the different features of interest. To avoid any faulty selection of regions of interest (ROI) by automatic segmentation due to similar intensity levels between pixels, a manual validation of the ROIs was conducted. This was achieved by using the ROI painter tool that allows accurate selection of ROIs for each slice (image). Once a feature of interest has been highlighted as a ROI in the dataset, it is possible to visualize several aspects of the ROI, such as spatial distribution, connectivity, or number of isolated elements. It is also possible to render a ROI into a mesh for a better visualization of the features of interest. The meshes illustrated in Figure 37 and Figure 44 were rendered in "solid" as filling mode and were smoothed using the Laplacian smoothing method with one iteration.

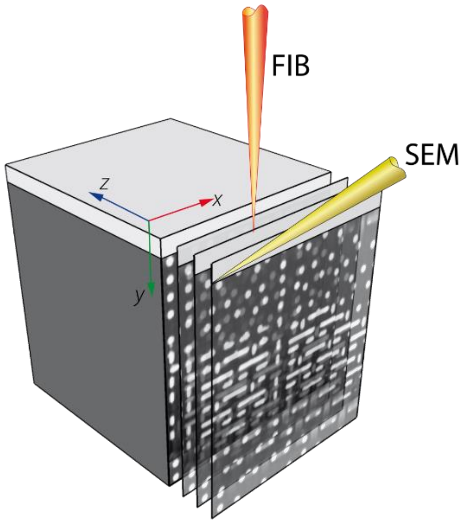

Figure 14: Schematic illustration of the serial sectioning principle.

7.4. Transmission and Scanning Electron Microscope (TEM/STEM)

Transmission Electron Microscope is a powerful tool in the field of material science. The unique and distinctive feature of this tool is the incident electron beam, which is transmitted through the sample instead of scattered on the surface of the sample as in a SEM. TEM investigation require a very thin sample of ≤ 100 nm. The TEM principle is similar to a light microscope but utilizes electrons instead of light. An image is therefore formed from the interaction between the sample and the electrons as the beam is transmitted through the sample. Due to the smaller wavelength of the electrons compared to light, a TEM exhibits image resolutions significantly higher than light microscopes. This makes possible the observation of fine details such as grain boundaries or small precipitates and even in some cases, individual atoms. A brief introduction to this technique is given below:

In TEM, electrons are generated from an electron source and accelerated through a high voltage of typically 60 – 300 keV. A series of electromagnetic lenses are used to focus the beam onto the sample and contribute to forming a final image. After the interaction of the electron beam with the sample, the transmitted electrons pass through an objective lens to form either an image or a diffraction pattern (DP) image on the image plane and back focal plane, respectively. Changing the strength of the intermediate lens changes the focusing position of the image or DP produced by the objective lens. This results in the production of a magnified image on the object plane of the projector lens. Finally, the projector lens forms a magnified image on the scintillator detector, which is usually a phosphor screen (scintillator coupled with a charge-coupled device (CCD)) [82].

Scanning TEM (STEM) combines the principle of TEM and SEM and can be performed on either of these instruments. The technique is similar to SEM and uses a faster scanning of the focused beam of electrons across the sample. However, the difference between SEM and STEM is that STEM requires a very thin sample and much higher spatial resolution. Imaging through the scattered beam of electrons, X-ray micro analysis, and other spectroscopic techniques can be employed.

All TEM investigations were performed by Dr. Imran Hanif using an FEI Titan 80-300 in STEM mode operated at 300 keV under different conditions for microstructural investigations. High angle annular dark field (HAADF) imaging was employed in STEM mode in which the transmitted electrons that scattered through relatively large angles were detected. Figure 15 shows a typical example of an HAADF image of the thin lamella in Figure 13d. In addition, Energy Dispersive X-ray spectroscopy (EDX) was carried out to determine the chemical compositions of the investigated features using quantification, line scan, and elemental mapping. The micrographs and EDX data were processed using Image J and FEI's Tecnai Imaging and Analysis (TIA) software, respectively.

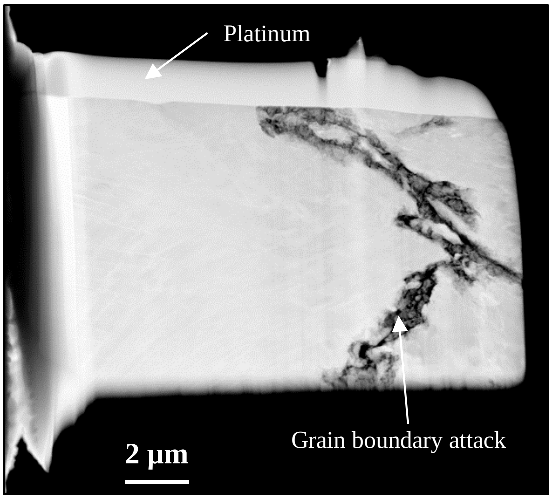

Figure 15: TEM image using high-angle annular dark-field (HAADF) of a grain boundary attack. Picture provided courtesy of Dr. Imran Hanif.

7.5. Broad Ion Beam (BIB)

The BIB technique was used to prepare cross-sections of the exposed samples. BIB provides high quality cross-sections using a mild milling with argon ions. The main asset of this technique lies in the obtainment of a large area of interest after milling (2-3 mm), while still exhibiting a quality of milling similar to the FIB technique. Compared to the mechanical polishing technique, the BIB technique avoids any mechanical stresses, degradation of oxide scales, and clogging of pores/voids. It relies on three individual ion sources whose beams are concentrated on an area. The sample is prepared by gluing a piece of silicon wafer on top of the sample to protect the surface, then it is preliminarily cut using a low speed saw to expose a cross-sectional area of interest. The sample is then attached to the sample holder of the BIB and adjusted so that the desired area is located at the intersection of the three ion beams. This is achieved by setting the length of the sample protruding from a mask covering and protecting the rest of the sample. The ion beams perpendicularly hit the mask and the sample, see Figure 16.

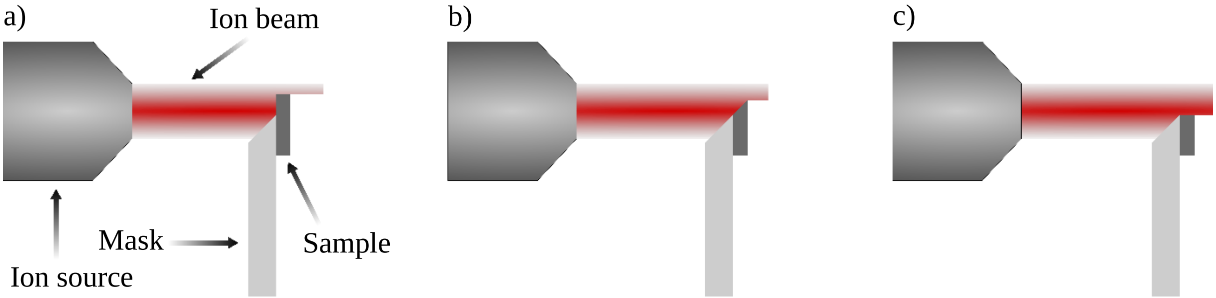

Figure 16: Schematic drawing of the BIB principle. a) Starting conditions, b) during milling, and c) milling completed.

The BIB used was a Leica TIC 3X, and the sessions were operated at 6.5 kV for a duration of 12 hours.

7.6. X-Ray Diffraction (XRD)

This technique is used to determine the crystalline phases present in a sample. It relies on the principle of coherent elastic X-ray scattering. A beam of incident monochromatic X-rays is generated and orientated towards the sample where the beam interacts with the crystal structure of the sample. The X-rays then scatter in several directions but diffract in some specific directions due to the periodicity of the crystal. The scattered X-rays can either have destructive or constructive interferences. Constructive interferences are produced when the conditions of Bragg's law are satisfied, resulting in the diffraction of the incident beam. This law relates the wavelength of electromagnetic radiation to the diffraction angle and the lattice spacing in crystalline samples via the following equation [83, 84]:

$$n\lambda = 2d\sin(\theta) \tag{20}$$

where d is the spacing between the diffracting planes, λ is the wavelength of the incident X-ray beam, θ is the incident angle, and n is an integer. A schematic drawing of the phenomenon is shown in Figure 17:

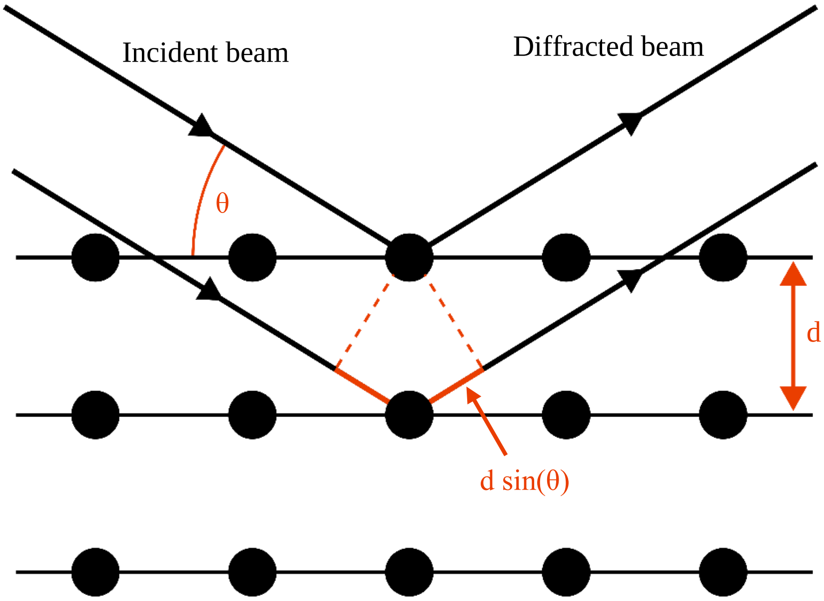

Figure 17: Representation of Bragg's law.

As the wavelength of the monochromatic beam of X-rays is fixed, the incident angle θ is the varying parameter during measurements. A standard setup for XRD analysis consists of one source of X-rays, a sample location, and a detector. Such a setup is called Bragg-Brentano geometry (Figure 18). It is possible to adjust the different parameters of a setup for a specific purpose, e.g. the grazing incidence setup is used to acquire information of mostly thin films by choosing a low angle of incidence for the X-rays.

An XRD analysis consists of measuring the intensity of the diffracted beam as a function of 2θ, resulting in diagrams called diffraction patterns. The patterns are compared with a database in order to identify the different phases.

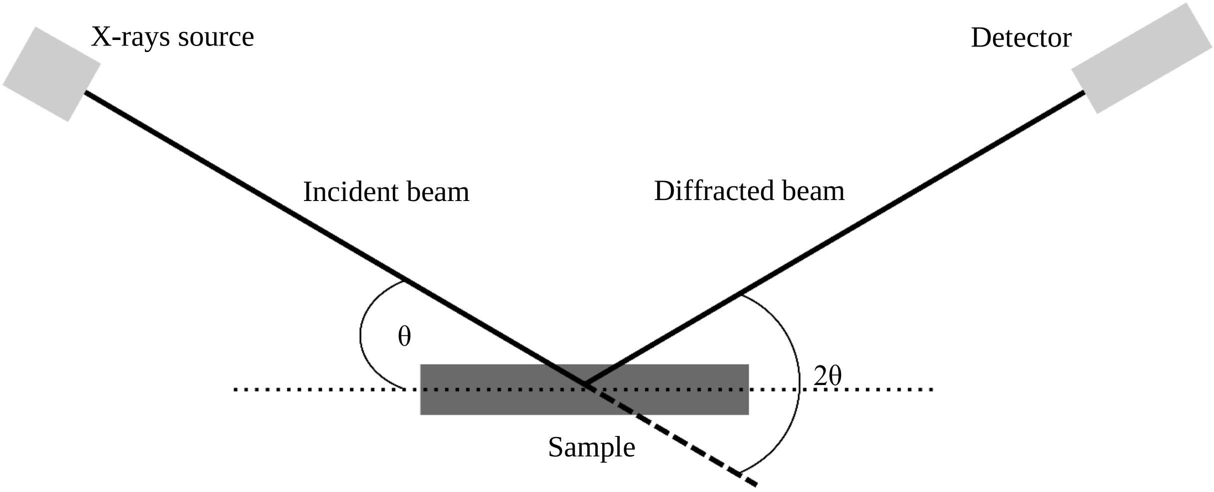

Figure 18: Schematic representation of a diffractometer with Bragg-Brentano geometry.

The diffractometer used for the XRD characterization was a Siemens D5000 with a Göbel mirror. The wavelength used was a specific Cu K_α ($\lambda = 1.54178$ Å) and was generated by a copper anode X-ray tube. The incident angle was 7.5°, and the measuring range was [10° - 80°].

7.7. Ion Chromatography (IC)

The Ion Chromatography technique allows the quantification of water-soluble ions, such as Cl^- or SO_4^{2-}. The technique was mostly used during the field investigations to study the influence of different parameters (e.g. type of fuel combusted) on the number of ions found in the deposits.

The exposed samples were first leached in a known volume of MilliQ water to dissolve the ions. The obtained solution was then pumped with an eluent through a column containing a stationary phase. This stationary phase separated the different ions present in the solution. The separation was based on the charge and size of the ions. The ions that exhibited less affinity with the stationary phase were less retained in the column, which resulted in a fast elution time. The ions that exhibited more affinity with the stationary phase were more retained in the column and therefore had a slower elution time. A detector located at the end of the column recorded the conductivity of the total solution as a function of time and compared it to a standard solution with a known concentration.

This technique analyzes cations and anions separately, depending on the column used. Only anions were considered in this study. A schematic representation of the technique is shown in Figure 19.

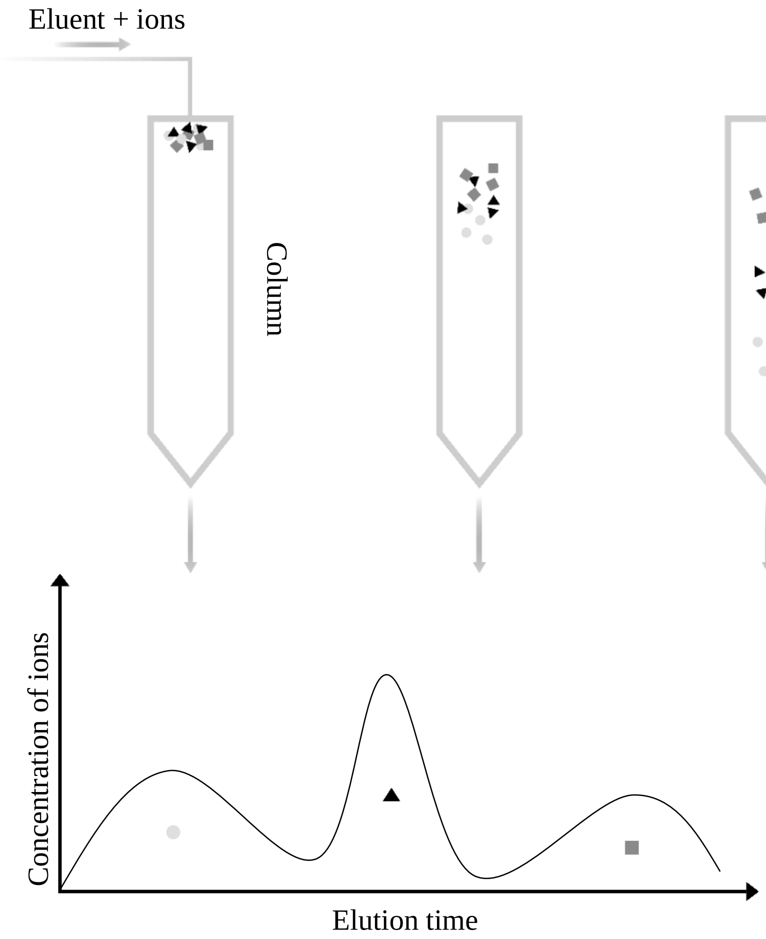

Figure 19: Schematic representation of the ion chromatography technique (top). Signal of the detected ions as a function of time (bottom).

The equipment used was a Dionex ICS-90 Ion Chromatography (IC) system with an IonPac AS4A-SC analytic column. The eluent used was a 1.8 mM sodium carbonate/1.7 mM sodium bicarbonate solution, and the flow rate was 2 mL/min. The samples were leached in 100 mL Milli-Q water and placed in an ultrasonic bath for 10 minutes

7.8. Ultrasonic measurements

During field investigations, material loss measurements were performed as well to characterize the corrosion rate of the samples. The thickness of each sample was measured at eight different points on the ring before exposure using an Olympus 27MG ultrasonic thickness gage with a 0.01 mm resolution.

8. Principles and methods

The corrosion of critical parts in biomass- and waste-fired boilers has been demonstrated and studied many times [6, 7, 13, 14, 16-21, 23, 24, 40, 41, 60-65]. However, the path towards suitable solutions for the mitigation of high-temperature corrosion is intricate. The complexity of the environment present in these boilers makes the field studies alone delicate to decipher. It is therefore necessary to conduct combined investigations in both simple (laboratory) and complex (field) environments. Investigations performed in laboratory allow a more simplified and well-controlled environment, while field investigations allow direct observation of the corrosiveness in a boiler environment. Thus, laboratory investigations allow the study of single parameters, such as water vapor content or a specific salt, to understand the role of each in the corrosion mechanisms that occur in biomass- and waste-fired boilers. Both types of investigation aim to increase knowledge about corrosion mechanisms and to develop solutions for corrosion mitigation.

8.1. Laboratory investigations of corrosion mechanisms

Laboratory investigations are essential to increase the understanding of corrosion mechanisms. However, a considerable difference in corrosion rates between field [17, 85] and laboratory [25, 86, 87] exposed samples was observed. Field samples encountered a considerably accelerated corrosion attack compared to laboratory samples. A novel laboratory setup was therefore developed to better mimic the corrosiveness of a boiler environment.

This thesis investigates in three different ways the corrosiveness of a setup allowing the continuous deposition of KCl via condensation of the salt on samples during exposures. In all cases, the novel setup was used to perform the exposures. First, a comparative study of four different commercial alloys (T22, 304L, Sanicro 28 and Inconel 625) was performed. Second, an in-depth study of grain boundary attacks was conducted on the stainless steel 304L, combining 3D reconstruction and TEM. Lastly, a collaboration between the Technical University of Denmark (DTU) and Chalmers University of Technology (CTH) was carried out. A part of this collaborative work aimed at comparing the influence of the method of applying KCl (pre-deposited vs continuous condensation) on the corrosion attack of a chromium-rich nickel-based alloy. The chemical compositions of the materials investigated are listed in Table 2.

- Exposures and characteristics of the setup

The exposures under continuous KCl deposition were performed in an atmosphere of 5 % O_2 + 20 % (15 % for the collaborative work with DTU) H_2O + N_2 (bal.). The desired water vapor content was achieved using nafion membranes FC 125-240-5MP from Perma Pure. The flow rate used was 2.5 cm/s, and was measured with a flowmeter Definer 220 from Bios. A 3-zone furnace ETF 80/12-III, from

Entech Energiteknik AB equipped with a 70-mm diameter silica tube from Quarzglas Komponenten und Service QCS GmbH was used. An alumina boat with KCl from VWR BDH Chemicals was placed upstream at 700 °C where the calculated vapor pressure of KCl was 65.9 ppm, while the samples were placed downstream at 600 °C where the calculated vapor pressure of KCl was 3.4 ppm. Therefore, the condensation of salt in the sample area was achieved during the exposures. The vapor pressures of KCl(g) at these two temperatures were calculated using the software FactSage 7.2 and the FTsalt database. The positions of the KCl boat and the samples remained consistent for all exposures. The silica tube was cleaned before each exposure by using water to remove any remnants of deposited KCl from the previous exposure. The standard duration of the exposures was set to 24 hours. A schematic illustration of the setup is shown in Figure 20.

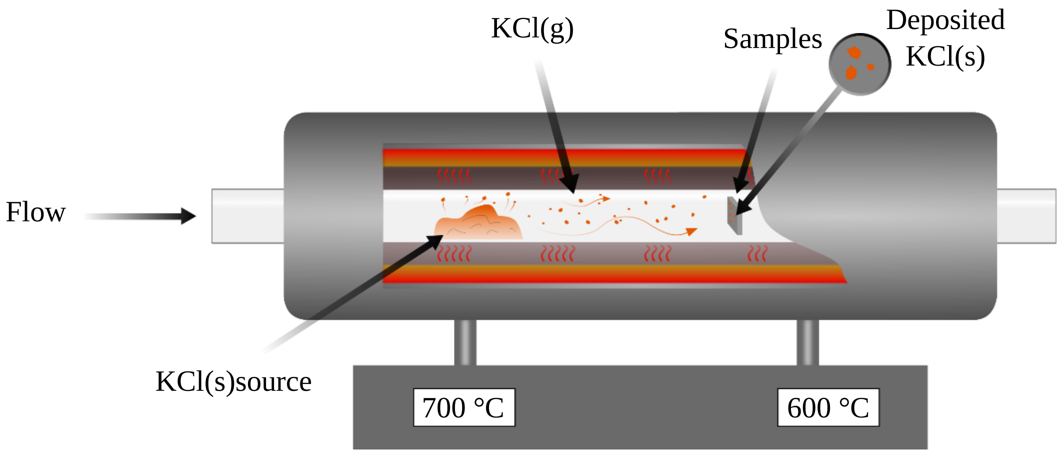

Figure 20: Schematic illustration of the experimental setup.

A similar experimental setup using a tube furnace with three individual heating segments was used to study the condensation of KCl and NaCl[88].

The temperature gradient profile in the furnace is shown in Figure 21. The gradient was measured two times in order to find the temperature variance between the two experiments as the furnace must be turned off for cleaning purposes before each exposure. The measurements were performed by moving a thermocouple 20-25301000 from Pentronic forward every 1 cm from one side of the tube to the other side for a total length of 75 cm, see Figure 22. The position of the thermocouple remained consistently at the center of the furnace (co-axial). It can be seen in Figure 21 that the temperature gradient between the source of KCl(s) and the samples remained stable between the two experiments, once the temperatures at each specific location had been reached.

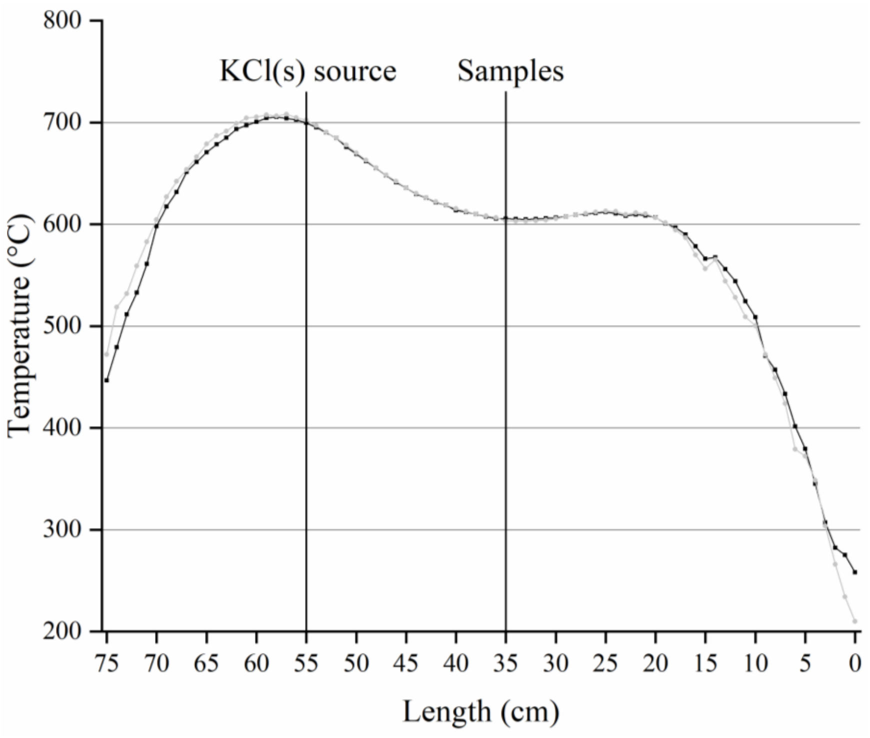

Figure 21: Temperature profile for the 3-zone heating furnace measured twice with a shutdown in between.

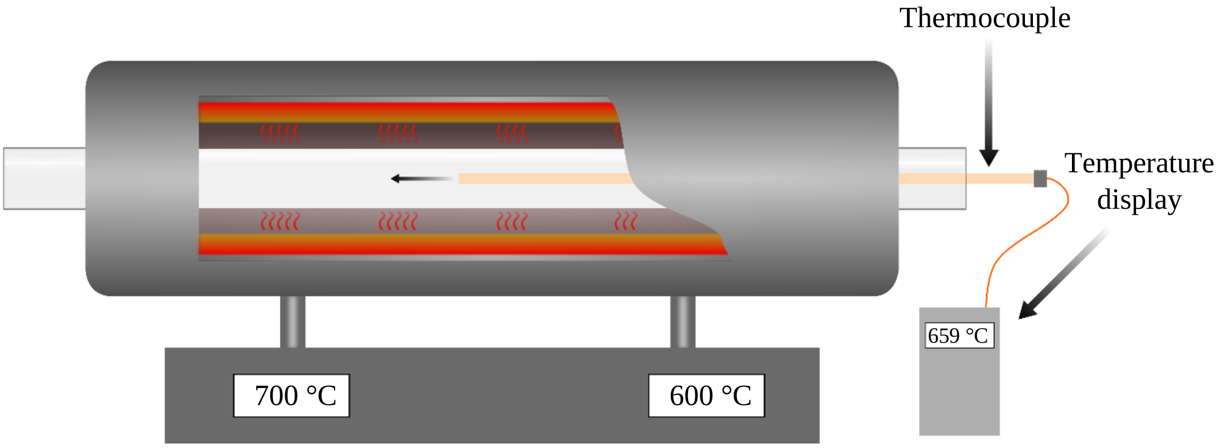

Figure 22: Schematic illustration of profile temperature measurements.

Due to the diameter of the tube and the laminar flow, a temperature spread of ± 2.5 °C was considered. This uncertainty was empirically confirmed by an average of measurements performed with shifting a thermocouple 1 cm in one direction, from the center, during the measurement of the profile temperature. The highest temperature was localized at the original measurement point, which was on the rotation axis of the tube, while the measurements performed by shifting the thermocouple 1 cm in one direction exhibited a lower temperature of maximum 2.5 °C, see Figure 23. Considering the location of the samples exposed at 600 °C, such a temperature difference will induce a variation in the vapor pressure of KCl(s) of ± 0.4 ppm, which is negligible.

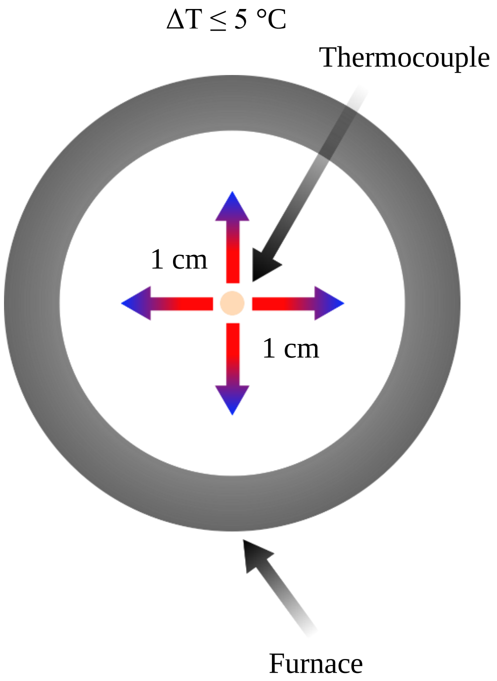

Figure 23: Schematic illustration in a cross-sectional view of the temperature uncertainty observations.

The amount of KCl deposited during the exposures is shown in Figure 24. The side positions averaged half the amount of KCl deposited at the middle position. The amount of KCl deposited every 24 hours for one week remained relatively consistent, with an average of 0.95 mg/cm^2 ± 0.31 mg/cm^2 per day at the middle position, and 0.44 mg/cm^2 ± 0.11 mg/cm^2 at the sides. In other words, this laboratory setup showed a reproducible KCl deposition for every experiment.

The measurements were performed using two parallel gold foils with which the mass gains of KCl were measured discontinuously every 24 hours for one week. Every 24 hours, the two gold foils were taken out of the furnace and weight measured, while a set of two new gold foils were placed for the next 24 hours. One of the gold foils was aligned with the axis of the tube furnace (middle position), while the second gold foil was located at one of the sides in order to replicate the position of future samples at the same locations. The side positions were located 1.8 cm apart from the middle position, and 1.5 cm apart from the walls of the tube furnace. Figure 25 shows a schematic illustration of the positions of the samples in the furnace.

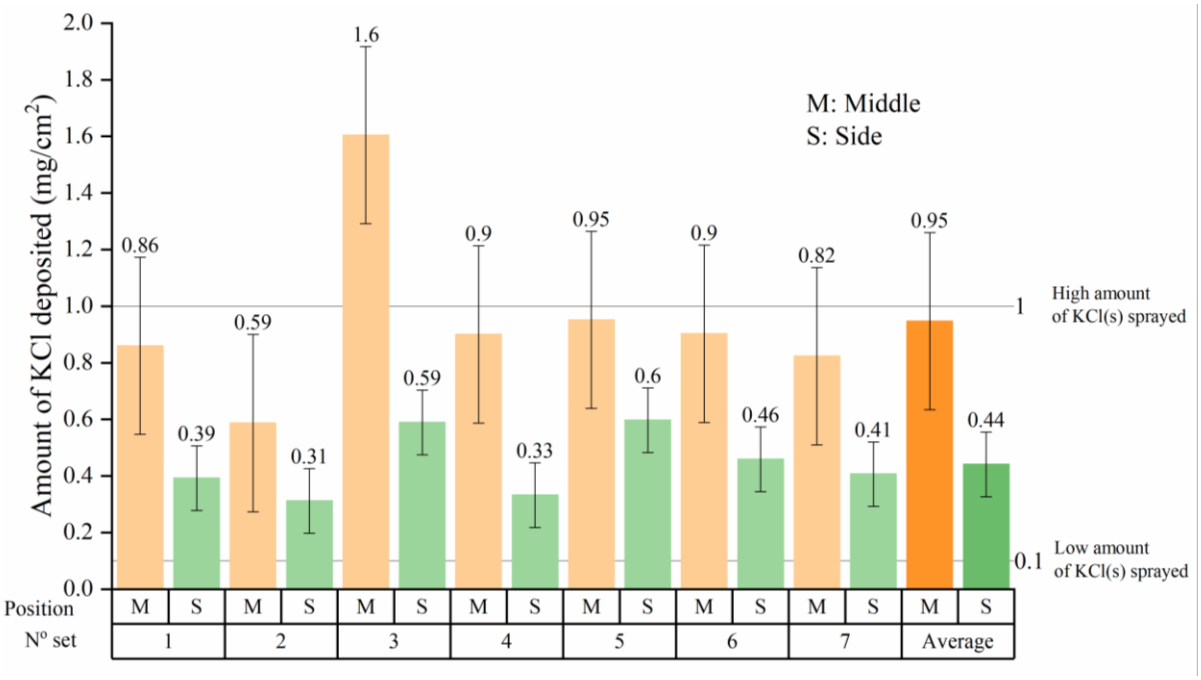

Figure 24: Amounts of KCl deposited on gold foils every 24 hours for one week at two sample positions. The reference lines represent the two different amounts of KCl(s) sprayed onto the samples prior to exposure (pre-deposited method).

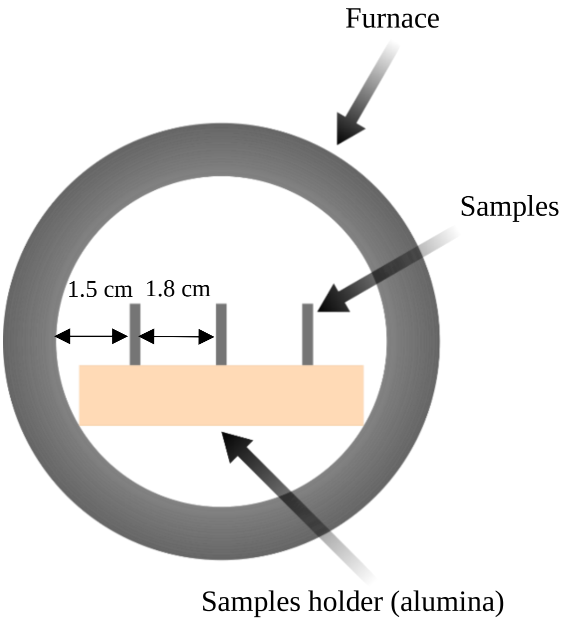

Figure 25: Schematic illustration of the sample positions within the furnace in a cross-sectional view.

- High-temperature exposures of commercial alloys with increasing nickel content: a comparative study

This study focused on the influence of alloying elements on the high-temperature corrosion resistance of alloys. In the harsh environment created by the experimental setup, all investigated materials rapidly reached breakaway oxidation. This implies that the primary protection was lost (i.e. the chromium-rich corundum oxide initially formed) and that the alloys could only rely on the secondary protection for the mitigation of the corrosion attack (i.e. the resulting oxide scale formed, e.g. Fe_2O_3 on top of a $(Fe,Cr,Ni)_3O_4$). In this corrosion mode, the role of nickel was specifically investigated for this study. The influence of alloying elements, such as chromium or nickel, on the high-temperature corrosion resistance of alloys when the primary protection has been lost is not fully understood. Moreover, a synergetic effect between the different alloying elements can occur, leading to a more complex corrosion behavior of the material.

Thus, understanding the influence of the addition of alloying elements is crucial for the development and optimization of corrosion-resistant alloys.

Four different commercial alloys with increasing nickel content used in biomass- and waste-fired boilers were selected: T91/P91- 0 wt.%. Ni, 304L – 10 wt.%. Ni, Sanicro 28 – 30 wt.% Ni and Inconel 625 ->58 wt.% Ni. The alloys were exposed in the referred setup at 600 °C to an environment containing 20% H_2O + 5% O_2 + N_2 (bal.) for 24 hours under continuous KCl deposition. The materials were then analyzed and compared using microscopy and XRD.

- In-depth investigation of grain boundary attack on a 304L-type alloy

This study focused on the advanced characterization of grain boundary attacks on a stainless steel. The corrosiveness of alkali chlorides towards stainless steels is well-known and has been explained by the “chromate formation” [17-19, 22-24, 27, 89, 90] or “active oxidation” [13, 16, 60-65] mechanisms. However, the active oxidation mechanism exhibited debatable elements as discussed in 6.3, which led to the search for other possible mechanisms, as suggested in 6.4. Nowadays, the complete chlorine-induced corrosion mechanism in stainless steels remains uncertain. Traditional microscopy-based investigations of intergranular corrosion are usually performed using techniques such as STEM, SEM and EDX. These techniques are powerful for analyzing the chemistry of the investigated features and material information from the micro to nano scale. However, the two-dimensional aspect of these investigations can result in hasty and faulty conclusions, e.g. if the investigation is conducted at the tip of a grain boundary attack or not.

Thus, this study aimed at providing more accurate representations and new insights into intergranular corrosion in stainless steels by using a FIB-SEM system to perform 3D reconstruction of grain boundary attacks. However, this method exhibited limited resolution as well as a lack of elemental analysis. A parallel TEM investigation was therefore performed in order to complete the morphological analysis of the grain boundary attack. With these two techniques in combination, the 3D-FIB was employed to give an overview and localize areas of interest for in-depth investigations with TEM. In such a way, the TEM results could be directly linked to the overview image, which is normally complicated when using TEM.

The investigation focused on the stainless steel 304L exposed for 1 hour and 24 hours at 600 °C in an 5% O_2 + 20% H_2O + N_2 (bal.) environment under continuous KCl deposition.

- Influence of microstructure and environment on the KCl-induced corrosion attack

During service at high temperature, materials can be subjected to a phenomenon called thermal ageing. Thermal aging refers to long-term, irreversible changes in the structure, composition, and morphology of materials exposed to temperatures that they are typically likely to encounter in service. In steels, these changes can be represented by phase transformations, phase precipitations, and grain boundary segregation. When thermal ageing is not desired (contrary to heat treatment), this can result in a decrease in the mechanical and corrosion properties of the steel, which can lead to failure of the material. The effect of thermal ageing on steels has been investigated thoroughly [91-97].

For chromium-rich steels or alloys, an important microstructural change induced by thermal aging is the evolution of chromium-rich phases such as carbides, σ-phase or α-Cr. It is therefore crucial for the design of materials for biomass- and waste-fired boilers to understand how alkali chlorine-induced corrosion can be affected by a change in microstructure. Thermally aged superheater alloys can exhibit chromium-rich precipitates in their microstructure that would be more selectively attacked compared to as-received superheater materials [28]. Some studies have investigated the effect of chromium-rich phases on chlorine-induced corrosion in iron-based alloys [28, 98, 99], however, the amount of research that has been carried out on nickel-based alloys is scarce. In the work performed by DTU [100], the main focus was to show the influence of α-Cr precipitates on the KCl-induced corrosion of nickel-based alloys that had been thermally aged. More specifically, two different grades of nickel-based alloys (Ni35Cr4Nb and Ni45Cr4Nb, see Table 2) were exposed to two different heat treatments to obtain different volume fractions of α-Cr:

- Solution-treated: 1100 °C for 1 hour → water quench → 700 °C for 9 hours → water quench.
- Aged: 650 °C for 6000 hours → air cooling.

The two heat treatments were selected based on a previous detailed characterization of the alloys [101]. The collaborative work between DTU and CTH formed a foundation from which to study the combined influence of KCl deposition and alloy microstructure. The work within this thesis is therefore focused on the Ni35Cr4Nb alloy exposed to KCl in two different ways: pre-deposited prior to exposure and continuous condensation during exposure.

Sample preparation

The materials were received as sheets that were cut into coupons with the following dimensions: 15x15x2 mm^3 with a hole of 1.5 mm diameter drilled at 2 and 7.5 mm from the edges. All samples were ground with 500 grit SiC from Struers and then polished to a mirror-like surface with 9, 3, and 1 µm diamond solutions DP-Suspension P using DP-Lubricant Yellow. As a final step, the samples were cleaned in acetone and then ethanol using the ultrasonic bath Elmasonic P from Elma.

The samples investigated in the collaborative work between DTU and CTH were prepared according to the method described in the respective article [100].

8.2. Approaches to mitigate high-temperature corrosion

Mitigating the high-temperature corrosion that occurs in biomass- and waste-fired boilers is crucial in order to reduce maintenance costs and reach the highest electrical efficiency possible. Superheaters experience severe corrosion in such environments, therefore, the solutions investigated were focused on this issue.

It is possible to mitigate high-temperature corrosion in two ways: improve the materials or alter the surrounding environment of the materials.

8.2.1. Mitigation of high-temperature corrosion by improving materials: the use of coatings

It is possible to improve the materials in two ways: the design and development of new alloy compositions and/or the utilization of coatings. Coatings have been widely as protective layers used through the years for many applications. However, coatings often exhibit issues such as high levels of porosity, poor adhesion to the substrate, and oxide formation during thermal spraying [102, 103]. These issues lead to failure of the coatings as protective layers. Moreover, in biomass- and waste-fired boilers, the presence of corrosive species, such as water vapor and alkali chlorides, make the presence of defects within the coating pernicious. Consequently, it is essential to reduce the presence of defects in order to enhance the performance of the coatings. A novel spraying technique named HVAF (High Velocity Air Fuel) has been developed and has exhibited better adhesion between the coating and the substrate as well as low levels of porosity [104-106].

The present study focused on the corrosion behavior of three nickel-based coatings HVAF-sprayed onto a low-alloyed steel substrate exposed to a mild (5% O_2 + 20% H_2O + N_2 (bal.)) and harsh (5% O_2 + 20% H_2O + N_2 (bal.) + pre-deposited KCl on the samples) environment. The chemical compositions of the coatings and substrate are given in Table 2.

Sample preparation

The substrate was the low-alloyed steel 16Mo3 in the shape of a rod with a diameter of 25 mm.

Prior to thermal spraying, the 16Mo3 substrate was grit blasted with alumina particles with a size of 63±10 µm. The purpose of this step was to clean the surface and make it rougher in order to achieve better adhesion between the substrate and coating.

A 16Mo3 rod of half a meter was set in a horizontal rotating mandrel during the spraying. A HVAF gun M3^{TM} Supersonic from Uniquecoat was used to spray the coatings. The parameters used during the operation are shown in Table 3 and were determined based on preliminary coating tests to decrease the porosity of the coating. The rod was then cut into pieces of 5 mm thickness, and the uncoated surfaces were also sprayed. The average thickness of the coating sprayed was approximatively 250 µm. After spraying, the samples were ground and polished down to 4000 grit with SiC paper, reaching a final thickness between 215 and 260 µm.

Table 3: Spraying parameters.

Nozzle type	3L2G
Air pressure (MPa)	0.8
Fuel 1 Pressure-Propane (MPa)	0.7
Fuel 2 Pressure-Propane (MPa)	0.7
Carrier gas Pressure-N2 (MPa)	0.4
Feed rate (g/min)	150
Pass velocity (m/min)	50
Pass spacing (mm/rev)	5
Spray distance (mm)	300
Number of passes	8

Exposures

The samples were weighed before and after exposure using a Sartorius^{TM} balance with five-decimal accuracy. KCl was deposited on the samples by spraying a solution of water-ethanol (20/80) containing the salt. The samples were subsequently dried with warm air. The total amount of salt deposited on each sample was 1.0 mg/cm^2.

The samples were then exposed in a horizontal silica tube furnace to two different environments:

- 600 °C – 20%H_2O – 5%O_2 - 168h – With 1 mg/cm^2 KCl (harsh environment)
- 600 °C – 20%H_2O – 5%O_2 - 168h – Without KCl (mild environment)

The water vapor content was established using nafion membranes FC 125-240-5MP from Perma Pure, and the flow was calibrated using a flowmeter Definer 220 from Bios in order to reach 3.1 cm/s.

Two samples were mounted vertically in an alumina boat parallel to the flow for every experiment.

8.2.2. Mitigation of high-temperature corrosion by altering the environment

In parallel with laboratory studies, it is necessary to investigate the corrosion behavior of materials directly in boiler environments. It is also crucial to correlate laboratory and field investigations to enhance the understanding of corrosion mechanisms.

Two field investigations were performed in this thesis. The first study focused on the potential of a new location for superheaters in a grate-fired boiler, while the second study investigated the influence of a novel technique named "sulfur recirculation" on corrosion memory. Both studies aimed at mitigating the high-temperature corrosion experienced by superheaters.

- First investigation: Steamboost superheater

The superheaters used in this investigation were called Steamboost and were located over the last part of the grate. The idea is that corrosive species are released over the first part of the grate, which makes the flue gas less corrosive in the last part of the grate, where the Steamboost superheaters are located. This position was suggested using Computational Fluid Dynamics (CFD) calculations [107].

AffaldPlus Combined Heat and Power (CHP)

The field exposures were performed in an AffaldPlus Combined Heat and Power (CHP) plant located in Næstved, Denmark. This is a 27 MW grate-waste-fired boiler. Its nominal capacity is 8 tons/h. The combustion system was based on the latest state-of-the art technology from Babcock & Wilcox Vølund, a combination of the technologies from the Vølund systems, CFD calculations, and combustion technologies. A schematic drawing of the plant showing the location of the performed tests is presented in Figure 26.

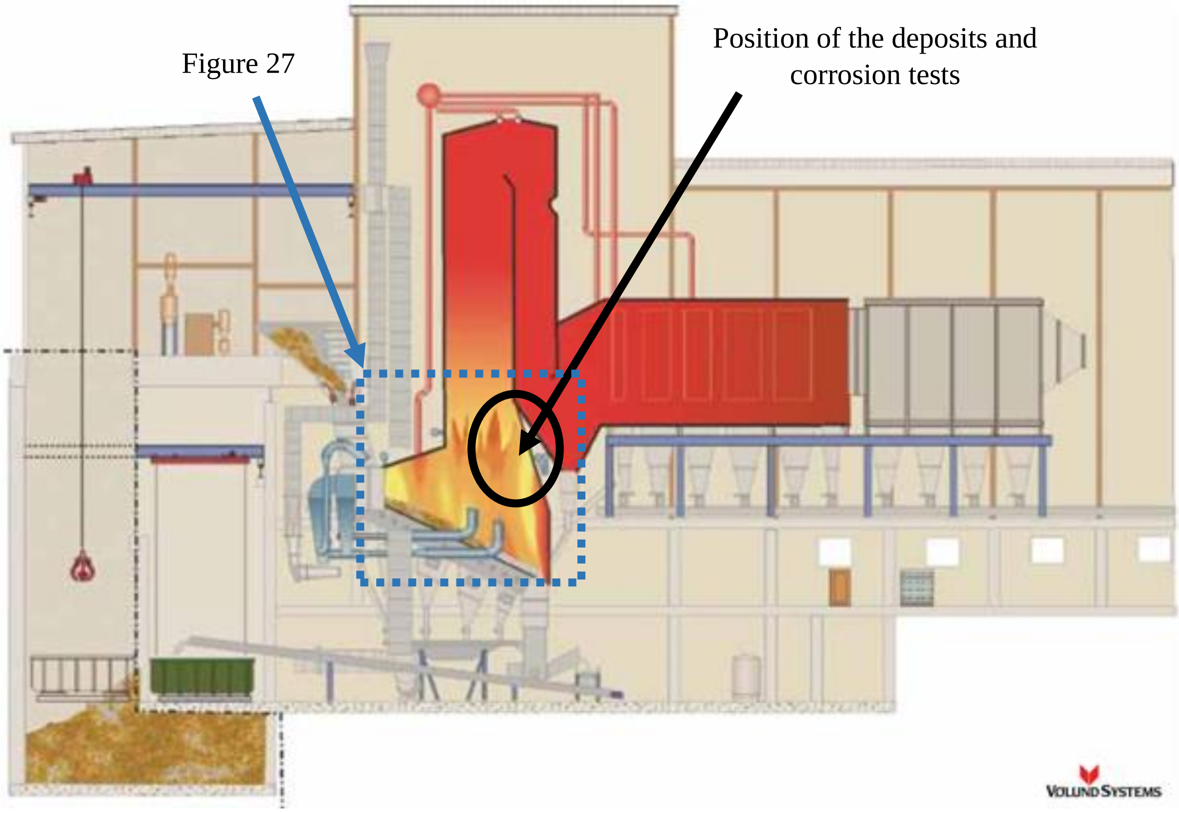

Figure 26: Schematic drawing of the combined Heat and Power plant AffaldPlus in Denmark [107, 108].

The investigation consisted of two parts:

- Deposit test: different ways of operating the boiler were tested in order to study the influence on the deposit’s composition at the Steamboost position using an air-cooled probe.
- Corrosion test: a corrosion probe (not investigated in the present thesis) and a fixed installation with various material grades connected to the main steam of the plant were installed at the Steamboost position.

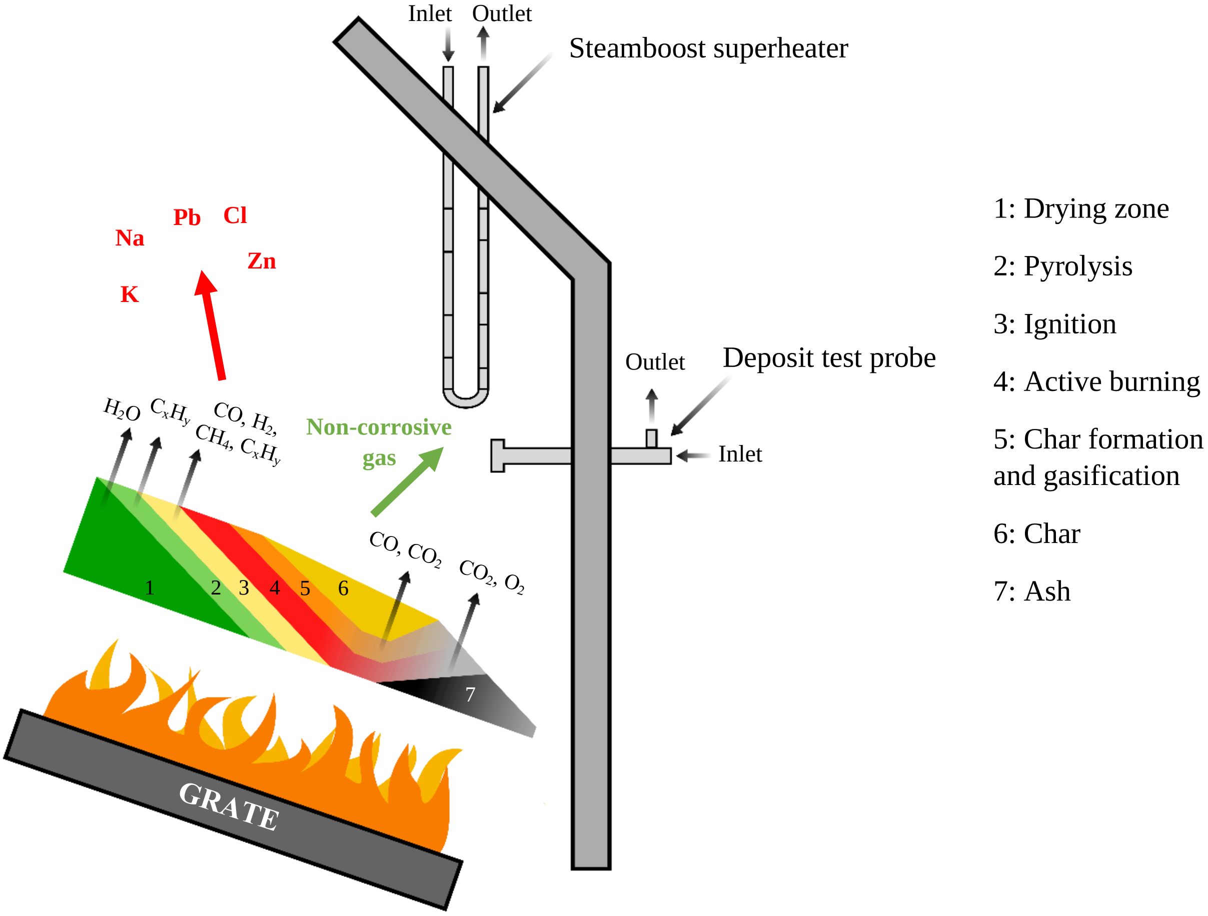

Figure 27: Schematic drawing of the principle of the Steamboost.

Figure 27 presents a schematic drawing of the principle of the Steamboost. Corrosive species are released over the first part of the grate, which results in a less corrosive environment over the last section of the grate.

Deposit tests

The purpose of the deposit test was to study the influence of operating the boiler with different air flow settings on the deposits at the Steamboost position. The duration of each exposure was 2 hours per setting for a total of 29 settings tested. Every setting had a different distribution and amount of air combined with grate operation. According to the CFD calculations (Figure 27), the corrosive species were released over the first part of the grate so that the corrosiveness of the flue gas released from the last part of the grate was lower. The air-cooled probe inserted carried nine samples, three per location on the probe, see Figure 28. Two temperatures were investigated: 525 °C and 700 °C.

The exposed samples were rings of the high-alloyed stainless-steel Sanicro 28. The reason for this choice was to avoid the influence of a large amount of corrosion products forming during the deposit tests. The samples were stored in desiccators with a drying agent, Sicapent® from Sigma-Aldrich after exposure. The deposits were analyzed using the Ion Chromatography technique described in 7.7.

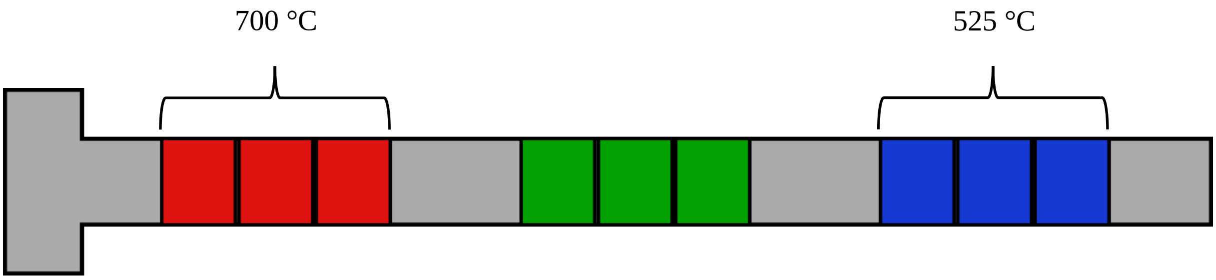

Figure 28: Schematic drawing of the probe carrying the nine samples for the deposit tests (only two temperatures investigated).

Corrosion tests

The Steamboost superheater was composed of three loops of several materials welded together and exposed for 8000 hours. Each loop carried the exact same materials the difference was the steam temperature, which was increased from the first loop to the last loop. The Steamboost superheater was connected to the main steam of the plant, which had an inlet temperature of 340 °C at the entrance of the installation, and an outlet temperature of 470 °C at the exit. This resulted in a metal temperature of approximatively 525 °C. The material loss of the materials was quantified by measuring the original thickness using ultrasound technique (described in 7.8) before exposure, and the remaining thickness of the uncorroded bulk material was quantified using SEM (an average of 8 different measuring points along the tube) after exposure.

- Second investigation: Sulfur recirculation and corrosion memory

MEC (Måbjerg Energy Center) Waste-to-Energy

This investigation was conducted at MEC, Denmark. The plant consists of two grate-waste-fired boilers supplied by Babcock & Wilcox Vølund A/S. The nominal capacity of each boiler is 11 tons/h of waste, producing 28 MW of continuous electrical power and 84 MW of district heating. The fuel consists of mainly household waste with some addition of industrial waste and sludge. Both boilers operate with the same fuel mix from one bunker. In addition, the two boilers are separated by only 10 m with manholes installed at the superheater position on both, allowing field investigations using probes. The Sulfur Recirculation system was installed in one of the line/boiler [109].

Sulfur recirculation and corrosion memory

The corrosiveness of different combusted fuels towards superheaters has been investigated thoroughly, however, these investigations have often used clean and uncorroded materials as starting conditions. An aspect to be considered when dealing with high-temperature corrosion in boilers is the corrosion history of the materials or the so called “corrosion memory”. The normal operation of a boiler is usually interrupted by shutdowns for maintenance, which can induce thermal fatigue in materials. In addition, the combusted fuels can inherently show some variations in their compositions, leading to different chemical compositions in the flue gas and, therefore, in the deposits that build on the surface of the materials. How a corrosion attack is influenced by the corrosion history of a material (i.e. previous deposit build-up and oxide scale formation) is an aspect that has not been studied exhaustively.

This study investigates how a corrosion attack is affected by inducing a corrosion history in the materials via two full-scale Waste-to-Energy lines/boilers using fuel from the same bunker, one operating with sulfur addition and one without. The beneficial effect of sulfur addition on high-temperature corrosion has been investigated extensively [12, 23, 85, 110-113]. The advantage of adding sulfur to the boiler environment (via elemental sulfur, a sulfur-rich additive, or co-combustion, e.g. sludge and coal) is the sulfation of the corrosive alkali chlorides. The alkali reacts with SO_2/SO_3 to form alkali sulfates, which are less corrosive than alkali chlorides, while chlorine is released as HCl. Several studies have investigated the interaction between alkali chlorides and sulfur containing species [23, 112].

However, adding sulfur usually leads to additional sulfur-rich ashes/residue in the flue gas treatment, which require specific handling. To overcome this issue, a technique named “sulfur recirculation” has been developed and installed full-scale at MEC. The difference with the conventional method is the absence of these additional sulfur-rich ashes/residue. As a result, it is possible to retain the beneficial effect of sulfur addition without the drawbacks that are associated with. This is achieved by recirculating sulfur from the wet flue gas back to the boiler. Sulfur Recirculation was first developed and tested in pilot scale by Hans Hunsinger at Karlsruhe Institute of Technology (DE) in 2007 [114]. The first permanent full-scale Sulfur Recirculation Technology was then installed in 2016 at MEC.

Sulfur Recirculation consists mainly of a storage vessel and a dosage system for hydrogen peroxide (H_2O_2), a raw gas analyzer for SO_2, equipment for transport, and dosage of sulfuric acid into the furnace (see Figure 29). The process of Sulfur Recirculation occurs as follows: SO_2 is separated from the flue gas in the wet scrubber using H_2O_2, producing a 15-25 wt% H_2SO_4 solution that is injected into the boiler, producing SO_2. Hence, a sulfur loop is created [109].

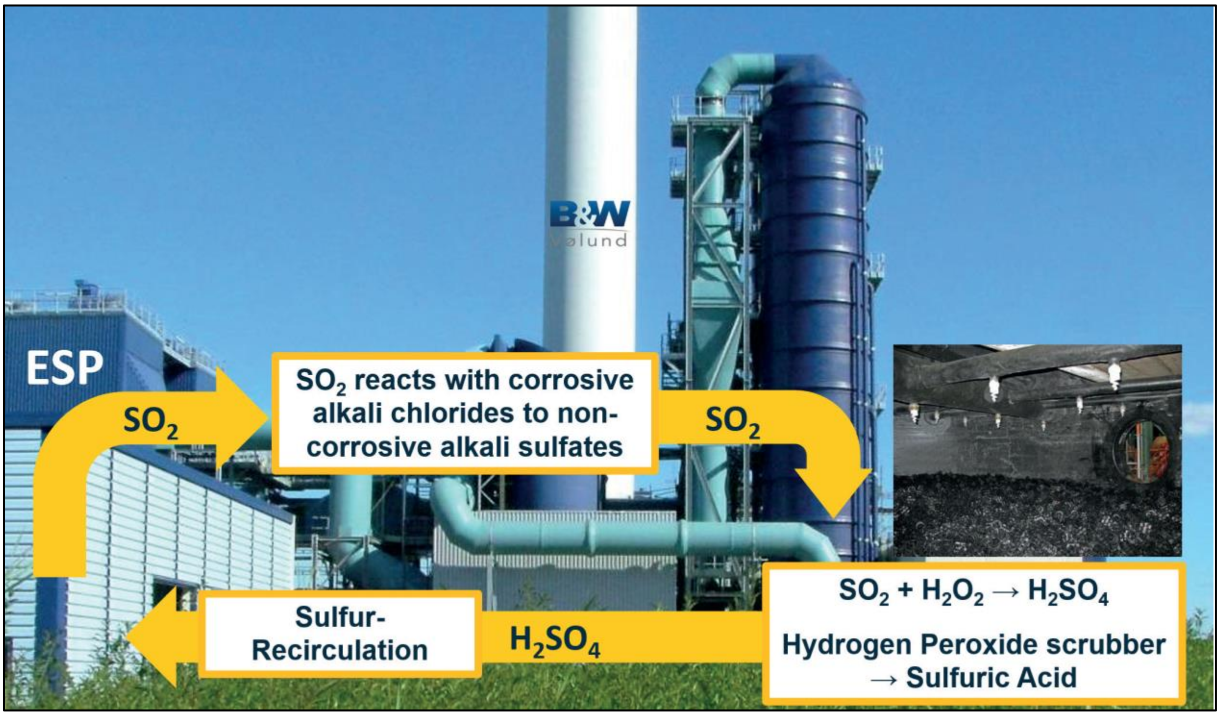

Figure 29: The flue gas treatment of MEC consists of an ESP (Electrostatic Precipitator), an HCl scrubber, a multistage scrubber for SO2 removal, dioxin removal using ADIOX[115], and flue gas condensation[109].

The sulfuric acid is sprayed through nozzles with atomization air, producing a fine mist that evaporates rapidly. The dosage rate is controlled by a regulator that maintains a fixed SO_2 setpoint.

Corrosion tests

The corrosion memory effect was investigated using two different lines and four different probes. The first line (Line 1, labelled “Rec”) generated a less corrosive environment due to Sulfur Recirculation while the second line (Line 2, labelled “Ref”) was used in a normal operating mode as a reference.

The exposures were performed using air-cooled probes similar to the one used in the first investigation (see Figure 28) with two different temperature zones, 450 and 525 °C. The setup of the probes was the following:

- Two probes remained in their respective line during the whole duration of the exposure. “Ref” was only exposed in the reference line and “Rec” only in the line using Sulfur Recirculation.
- Two probes labelled “corrosion memory probes” were switched after half of the duration of the total exposure. “RefRec” refers to the probe first exposed to the reference line and then to the Sulfur Recirculation line, while “RecRef” refers to the other way around.

The total duration of the exposure was 2000 hours, and the position of the corrosion memory probes was switched after 1000 hours of exposure.

The exposed samples were rings of stainless steel 347H. Only the samples exposed at 525 °C were included in this investigation as the samples exposed to 450 °C exhibited very little material loss. The chemical composition of the 347H of this investigation is similar to the one mentioned in Table 2 with the exception being a Niobium content of 1.10 wt%. The material loss of the materials was quantified by measuring the original thickness of the samples before exposure with a digital screw micrometer (0.0001 mm resolution) and the remaining thickness of uncorroded bulk material was measured using SEM after exposure (an average of 8 different measuring points along the ring for both measurements).

Deposit tests

Samples of the deposits on each probe were also analyzed using the Ion Chromatography technique described in 7.7.

9. Results and discussions

9.1. Laboratory investigations of corrosion mechanisms

9.1.1. High-temperature exposures of commercial alloys with increasing nickel content: a comparative study

In the harsh KCl-rich environment typical for certain types of biomass and waste, the corrosion attack is often very fast and breakaway corrosion usually starts within hours or days. In this process the primary protection oxide scale, e.g. the thin and slow-growing chromium-rich oxide that forms on stainless steels, is destroyed and the resulting oxide scales will influence the further corrosion attack. This type of oxide scale has recently been denoted as a secondary protection oxide scale [116]. Thus, from a boiler corrosion perspective optimizing the corrosion resistance properties of this, secondary protection oxide scale, is probably of great importance for the lifetime of the material. However, systematic studies targeting the secondary oxide (i.e. the oxide scale after breakaway corrosion) is scarce in the literature.

In this study, four commercial alloys (T91/P91, 304L, Sanicro 28 and Inconel 625) exposed in a harsh environment with continuously depositing KCl was in focus. To simulate a KCl-rich environment, a setup developed and presented in [117] was used in order to mimic the continuous deposition of KCl(s) that occurs in biomass and waste fired boiler environment. The investigated materials were selected in such way that they represents a broad range of material classes (from ferritic/martensitic stainless steel T91/P91 to the austenitic stainless steels 304L and Sanicro 28 to the austenitic nickel based alloy Inconel 625) but also to contain an increase amount of nickel (T91/P91: 0 wt.%. Ni, 304L: 10 wt.% Ni, Sanicro 28: 30 wt.% Ni and Inconel 625: 62 wt.% Ni).

The results showed that the corrosion attack, both in extent and in character, differ between the materials. However, despite this, the corrosion attack could always be defined by “general corrosion attack” and/or “steel grain boundary attack”. The discussion of the results is therefore divided into two subchapters, namely “General corrosion – Oxide scales” and “Steel grain boundary attack”.

General corrosion – Oxide scales

Overall, the material T91/P91 exhibits the thickest oxide scales among the investigated materials. The materials can be ranked based on the total thickness of oxide formed (both outward- and inward-growing oxides) as the following: T91/P91 [15-29] µm > 304L [4-15] µm > Sanicro 28 [3-9] µm > Inconel 625 [0.2-5] µm (see Figure 30 - Figure 33). As such, the ranking could also be group as ferritic/martensitic stainless steel (0 wt.% Ni) > austenitic stainless steel (10 wt.% Ni) > austenitic stainless steel (30 wt.% Ni) > austenitic nickel-based alloy (62 wt.% Ni). In a mild environment (e.g. the corresponding dry environment in the absence of KCl(s)) all these materials perform well, forming a chromium rich oxide in the submicron range. This oxide may be referred to the primary protection of the steel as it is slow-growing, adherent and protects the underlying steel from accelerated corrosion in this environment. However, in more aggressive environments, e.g. in the presence of KCl + H_2O or O_2 + H_2O, this thin protective oxide is deteriorated according to reaction (7) and (8) , and breakaway corrosion occurs with high corrosion rates [17-19, 22-24, 27].

The oxide thicknesses of the exposed materials in this study indicates that all materials have reached breakaway corrosion after 24 hours under these experimental conditions. The chromium-rich oxide initially forming have for all these alloys reacted with the KCl-rich environment forming K_2CrO_4 (potassium chromate) and fast-growing oxide scales. The resulting oxide scale is referred to the secondary protection of the alloy, i.e. this oxide scale serves as the protection towards further corrosion attack.

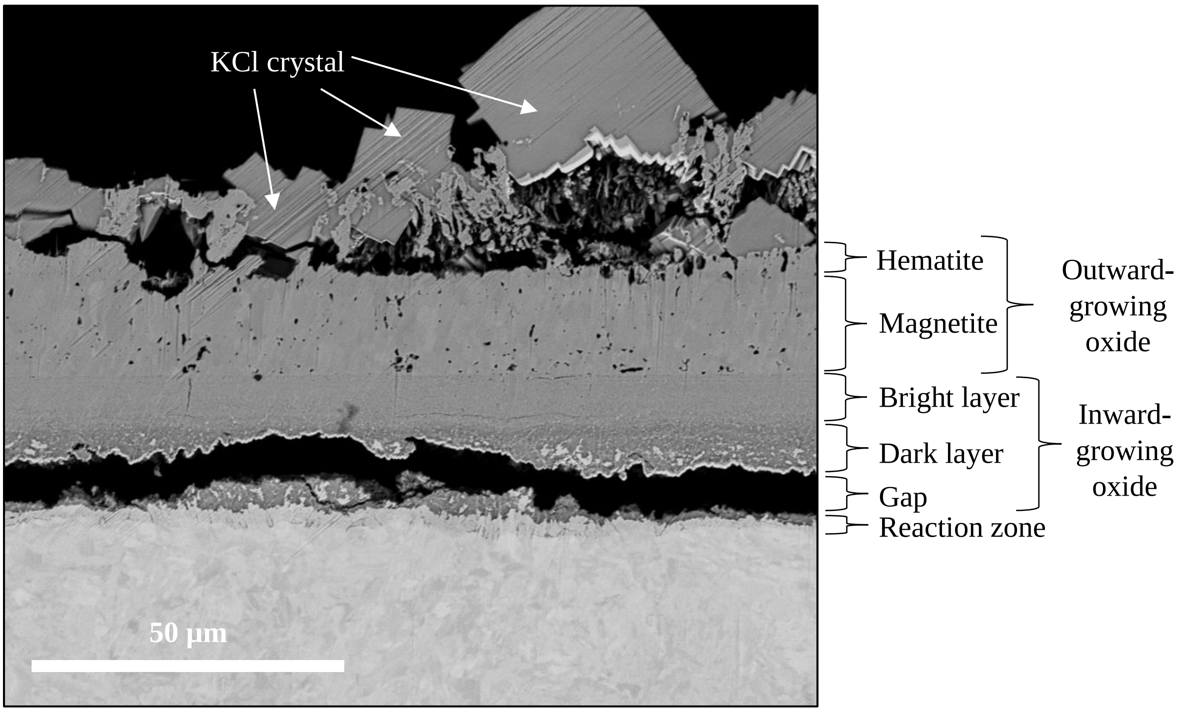

Figure 30: SEM images using BSE of a cross-section of T91/P91 exposed to 5% O_2 + 20% H_2O + N_2 (bal.) under continuous KCl deposition at 600 °C for 24 hours.

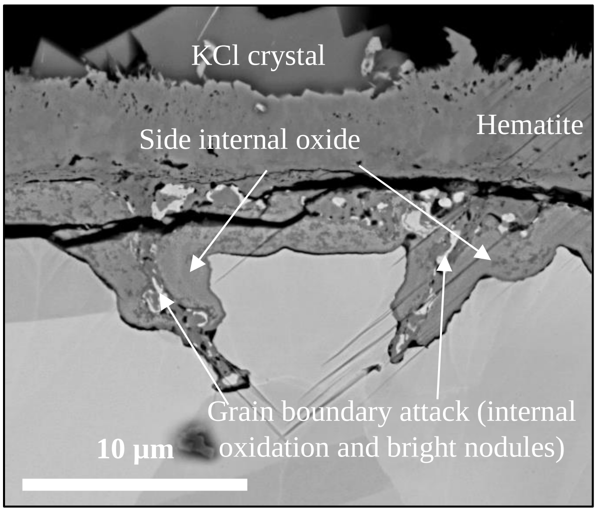

Figure 31: SEM images using BSE of a cross-section of 304L to 5% O_2 + 20% H_2O + N_2 (bal.) under continuous KCl deposition at 600 °C for 24 hours

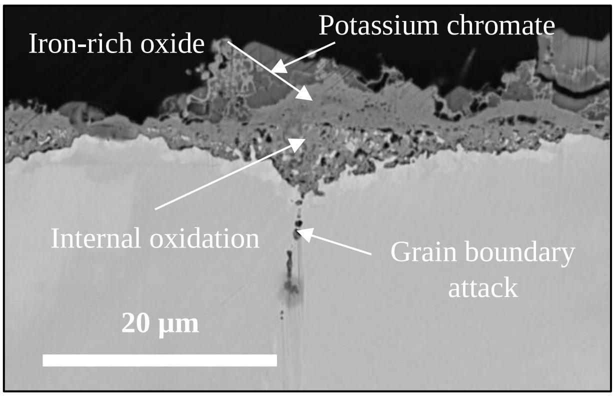

Figure 32: SEM images using BSE of a cross-section of Sanicro 28 to 5% O_2 + 20% H_2O + N_2 (bal.) under continuous KCl deposition at 600 °C for 24 hours.

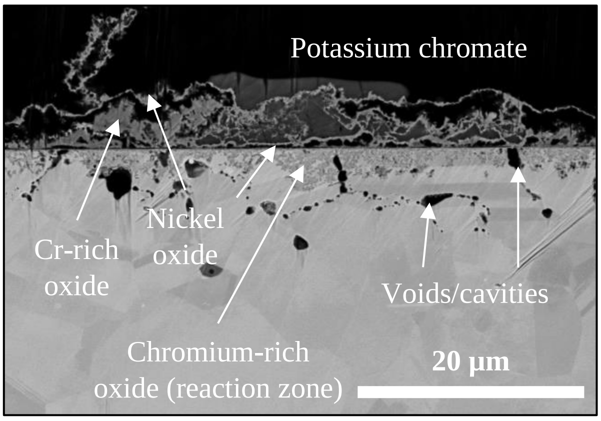

Figure 33: SEM images using BSE of a cross-section of Inconel 625 to 5% O_2 + 20% H_2O + N_2 (bal.) under continuous KCl deposition at 600 °C for 24 hours.

The overall trend in general corrosion attack between the four investigated materials shows that by increasing the amount of alloying elements, e.g. nickel or chromium, the total oxide thickness becomes thinner. The transition between primary/secondary regime was fast for T91/P91, 304L and Sanicro 28, all three materials showed an accelerated corrosion attack already after 1 hour. For Inconel 625, it is unclear how fast the transition was as this material was only exposed for 24 hours. The fast transition from primary to secondary regime indicates that the difference in oxide thicknesses is due to different properties of the secondary protection oxide of the alloys. In a recent study, Ni content and alloy microstructure were suggested to improve the corrosion properties of the secondary oxide scale [116]. With Ni 0 wt.% such as T91/P91, the general corrosion is defined by a thick outward-growing oxide scale made of hematite and magnetite, and an iron- and chromium-rich inward-growing oxide scale being a reaction zone. Increasing the nickel content to 10% and 30 wt.%. leads to the stainless steels 304L and Sanicro28 respectively. An increase of nickel content (to 10 wt.% and 30 wt.%, i.e. 304L and Sanicro28) results in a drastic reduction of the total oxide thickness in both materials compared to T91/P91. However, this decrease is much more prominent when going from 0 to 10 wt.% Ni (23 µm to 9 µm total oxide thickness) than from 10 to 30 wt.% Ni (9 µm to 6 µm total oxide thickness) which results in a smaller reduction of the total oxide thickness. A nickel-based alloy such as Inconel 625 with 62 wt.% Ni lead to the formation of an approximately 250 nm NiO scale on top of the substrate material and a shallow chromium-rich inward-growing oxide scale (see Figure 34), emphasizing the influence of nickel on the general corrosion behavior.

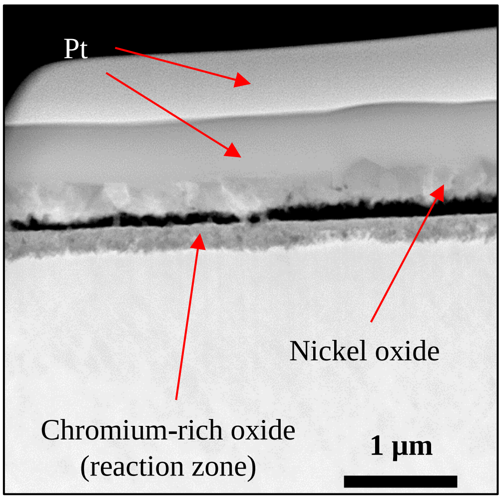

Figure 34: TEM image using High Angle Annular Dark Field (HAADF) of lift-out of an area of Inconel 625 where only the thin oxide was present. Picture provided courtesy of Dr. Imran Hanif.

Thus, it is a clear trend that an increased nickel content in the alloy decreased the total thickness of the oxide scales formed. However, this study included four commercial alloys, one ferritic/martensitic and three austenitic, and besides nickel also other alloying elements like e.g. iron and chromium varies between the materials. It has earlier been suggested that the corrosion resistance of a steel/alloy can be related to the Cr/Fe ratio in the steel/alloy [70]. From the setup of this study, using commercial alloys, it is not possible to deduce exactly which parameter that is mostly contributing to the corrosion protection of the alloy. In order to fully elucidate the role of nickel in the secondary regime in the presence of KCl (i.e. corrosion after breakaway oxidation has occurred), model alloys need to be investigated where other factors besides the nickel content can be controlled better.

Steel grain boundary attacks

The extent of steel grain boundary attack differed substantially between the four investigated materials. For the ferritic/martensitic T91/P91, containing no nickel, there is only small indications of steel grain boundary attack, see e.g. Figure 35.

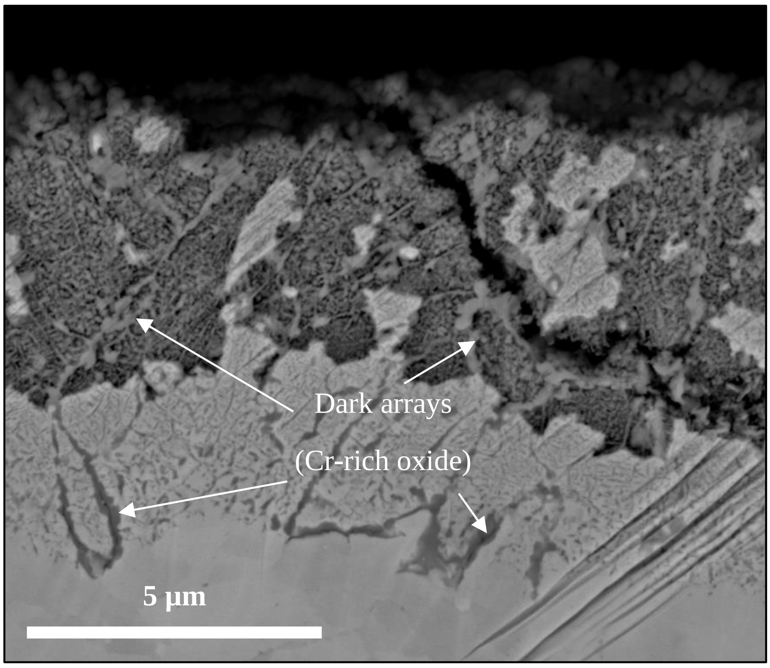

Figure 35: High magnification SEM image using BSE of the inward-growing oxide and reaction zone at the metal/oxide interface.

For the austenitic stainless steels and nickel-based alloy (304L, Sanicro 28 and Inconel 625) the steel grain boundary attack is much more pronounced, in relation to the general corrosion attack. The observed steel grain boundary attack on the four investigated materials showed that an increase in nickel content in the alloy does not lead to a mitigation nor an avoidance of grain boundary attacks. Contrary to the general corrosion, the steel grain boundary attack remains present in all four materials. However, the morphology or type of grain boundary attacks were rather different. With T91/P91 (0% Ni), the grain boundary attack is represented by dark arrays (being chromium-rich oxide) forming at the steel grain boundaries, showing no signs of porosity (see Figure 35). For 304L and Sanicro 28 (18 wt.% and 30 wt.% Ni, respectively), the grain boundary attack changed its corrosion morphology. For both materials, the attack was defined by a narrow internal oxidation and the presence of nickel-rich nodules at the grain boundaries (see Figure 31 and Figure 32). In addition, some small voids were observed in the grain boundary attack, slightly more pronounced for Sanicro 28 compared to 304L. There were also indications of the grain boundary attack of 304L being the initiation point for oxidization of the bulk grain, i.e. the grain boundary attack is no longer defined by a narrow oxidation zone but instead the grows laterally. As this was mostly observed at the part of the grain boundary attack closer to the surface, the grain boundary attack seems to be diffusion controlled. In contrast to the three other materials, the steel grain boundary attack of Inconel 625 is primarily defined by void formation at the grain boundaries instead of internal oxidation (see Figure 33). The reasons behind such a change in the morphology of the attack due to an increase of nickel content in the alloy are still unknown.

It can be observed that in the absence of nickel, T91/P91 exhibits really shallow grain boundary attacks compared to the three other materials. When adding nickel in the alloy, the depth of grain boundary attacks increases. However, considering only the nickel-containing alloys, even if the grain boundary attacks observed are deeper than in the case of T91/P91, increasing the amount of nickel seems to mitigate the depth of grain boundary attacks. From a maximum depth of 50 µm for 304L to 18 µm for Sanicro and 11 µm for Inconel 625, this indicates that increasing the nickel content reduces the extent of the attack as well.

Regardless of material, chlorine was detected in connection to the grain boundary attack. However, the exact distribution and role of chlorine in the grain boundary attack is hard to elucidate with the methods used within this paper. In order to improve the understanding of the role of chlorine in this type of attack, it is suggested to include TEM investigations.

As for the general corrosion attack, the grain boundary attack of the investigated steels and alloys cannot be deduced to solely be an effect of nickel content as other parameters (e.g. other alloying elements and crystal structure) are changed as well. Instead, this study shows the performance of four commercial steels/alloys in a harsh KCl-rich environment and how this effects the extent and type of corrosion. The role of nickel in the secondary regime, i.e. the corrosion properties of the oxide scale formed after breakaway corrosion, is suggested to be performed with model alloys where better control can be achieved of other parameters.

9.1.2. In-depth investigation of grain boundary attack on a 304L-type alloy

Intergranular corrosion or grain boundary attack is a sign of severe corrosion attack (or accelerated corrosion) frequently observed on steels in biomass- and waste-fired boilers [17, 118]. It was recently shown that adding KCl from the gas phase in laboratory exposures may lead to grain boundary attack in a 304L-type stainless steel [117]. However, the mechanism driving the intergranular corrosion is not known. One reason is that traditional microscopy-based investigations of intergranular corrosion are usually performed using techniques such as scanning transmission electron microscopy (STEM), scanning electron microscope (SEM), and energy dispersive x-ray spectroscopy (EDX). These techniques are efficient for analyzing the chemistry of the features of interest and material information from the micro to nano scale. However, the two-dimensional aspect of these investigations makes it hard to systematically investigate the corrosion front of a grain boundary attack.

This study aims at increasing the understanding of the grain boundary by providing more accurate representations of and new insights into intergranular corrosion in stainless steels by using a FIB/SEM to perform 3D reconstruction/tomography of grain boundary attacks linked to a TEM.

The focus of this work was on the initiation (1-hour exposure) and the first step of the propagation (24-hour exposure) of intergranular corrosion of the stainless steel 304L in the presence of KCl. The samples were exposed to a 5% O_2 + 20% H_2O + N_2 bal. environment under continuous KCl deposition for 1 hour and 24 hours at 600 °C. For this reason, the discussion of the results is divided into two sub-sections based on the duration of exposure.

Due to the experimental setup, heterogeneous deposition of KCl occurred on a sample's surface [117]. Most of the deposition took place on top of the sample that stood in the furnace, while little deposition was found at the bottom of the sample. The top of the samples therefore exhibited a more severe corrosion attack (as well as intergranular corrosion) than the bottom parts. All characterizations were consequently performed in areas located on the top of samples where the corrosion attack was more severe and intergranular corrosion was present.

Initiation of a grain boundary attack (1-hour exposure)

The SEM-BSE/TEM images show that the initial corrosion attack consisted of an outward-growing iron oxide scale on top of an inward-growing Fe,Cr,Ni oxide scale (see Figure 36), i.e. indicating an ion diffusion controlled secondary protection. Beneath this scale, the grain boundary attack had reached a depth up to ~3 µm after only 1 hour.

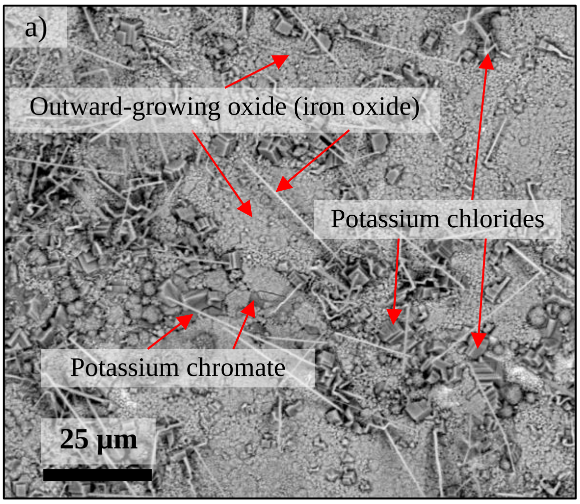

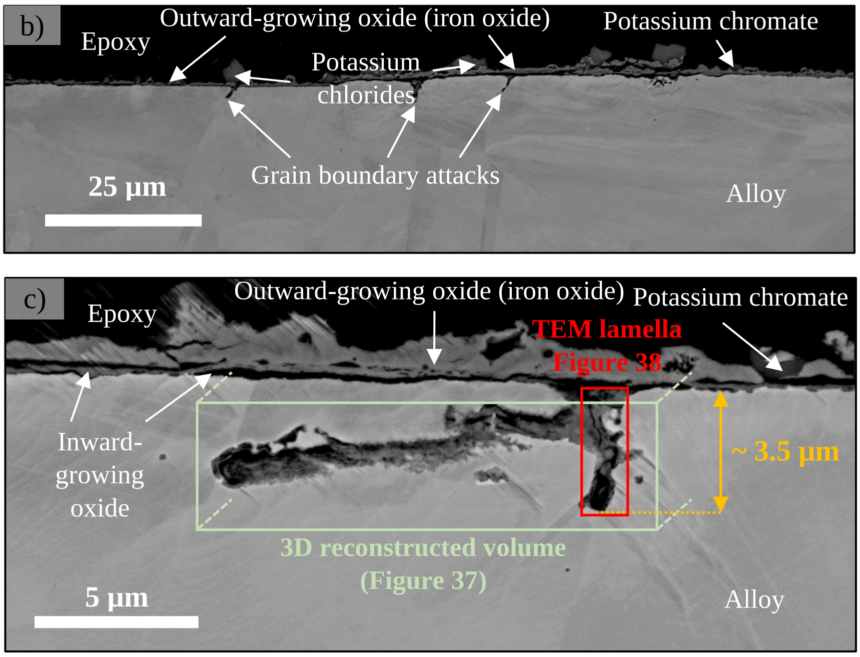

Figure 36: SEM images using BSE of a) plan view, b) low magnification, and c) high magnification cross-sections of a 304L sample exposed to 5% O_2 *+ 20%* H_2O *+* N_2 *(bal.) under continuous KCl deposition at 600 °C for 1 hour. The marked region (green box) refers to the area and volume investigated via 3D tomography (see in Figure 37). The marked red box labelled "TEM lamella" refers to a typical grain boundary attack investigated via TEM (see Figure 38). The yellow measurement annotation refers to the maximum depth of the grain boundary attacks in this area.*

The 3D-FIB/TEM investigation showed that the grain boundary attack during the initial attack was characterized by voids with very little oxidation/chlorination, especially at the apparent tip of the attack (see Figure 39). The 3D tomography analysis (see Figure 37) revealed that 96% of these voids were directly connected to the metal/oxide interface (represented as the green mesh), which can be interpreted as fast pathways for the gas transport and/or ion diffusion of species on the surfaces surrounding the voids. The open, connected pore network in the grain boundary regions, the absence of large oxide formation in the same regions, and the expected increase in Cl load below the deposited KCl regions can indicate the presence of the volatile iron/chromium chlorides associated with the active oxidation mechanism [13, 16, 60-65].

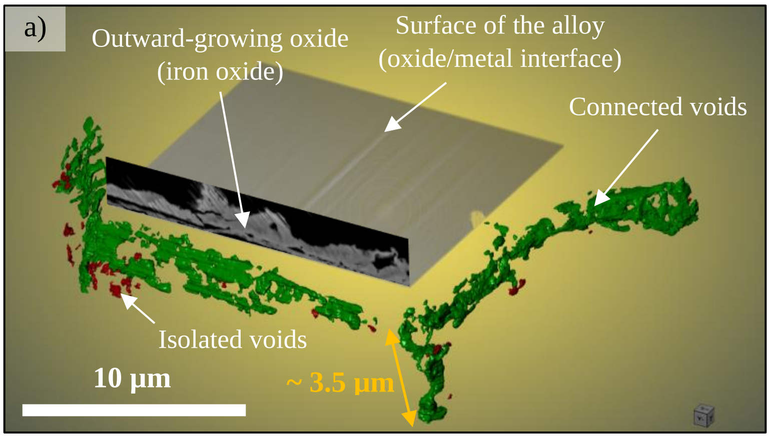

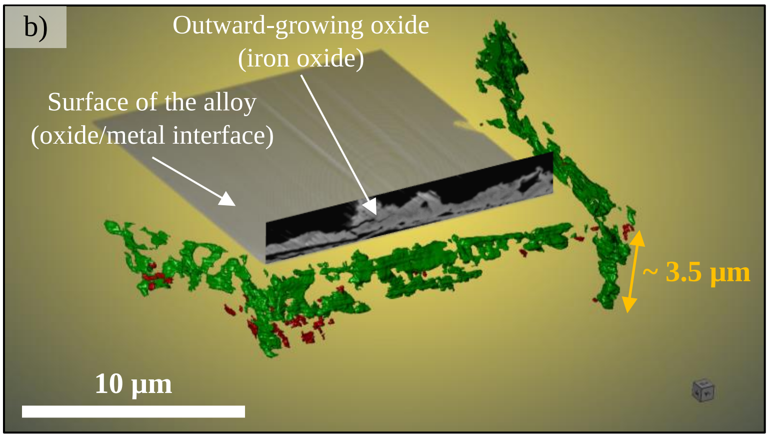

Figure 37: a) 3D tomography of the voids from the area highlighted by the green box in Figure 36c, and b) the same illustration from a different angle. The green mesh represents the voids connected to the surface (oxide/metal interface) and the red mesh represents the voids not connected to the surface (isolated).

At one position (outer void in the TEM investigation), higher levels of Cl (about 10 at.% associated with Fe/Ni) were observed, see Figure 38b. However, no local accumulation of iron oxide was detected in these regions. Instead, the investigation revealed an intact secondary oxide scale that seemed to remain diffusion controlled as no severe degradation of the oxides was observed, i.e. indications of cracks and/or accumulation of oxide pores, see Figure 38.

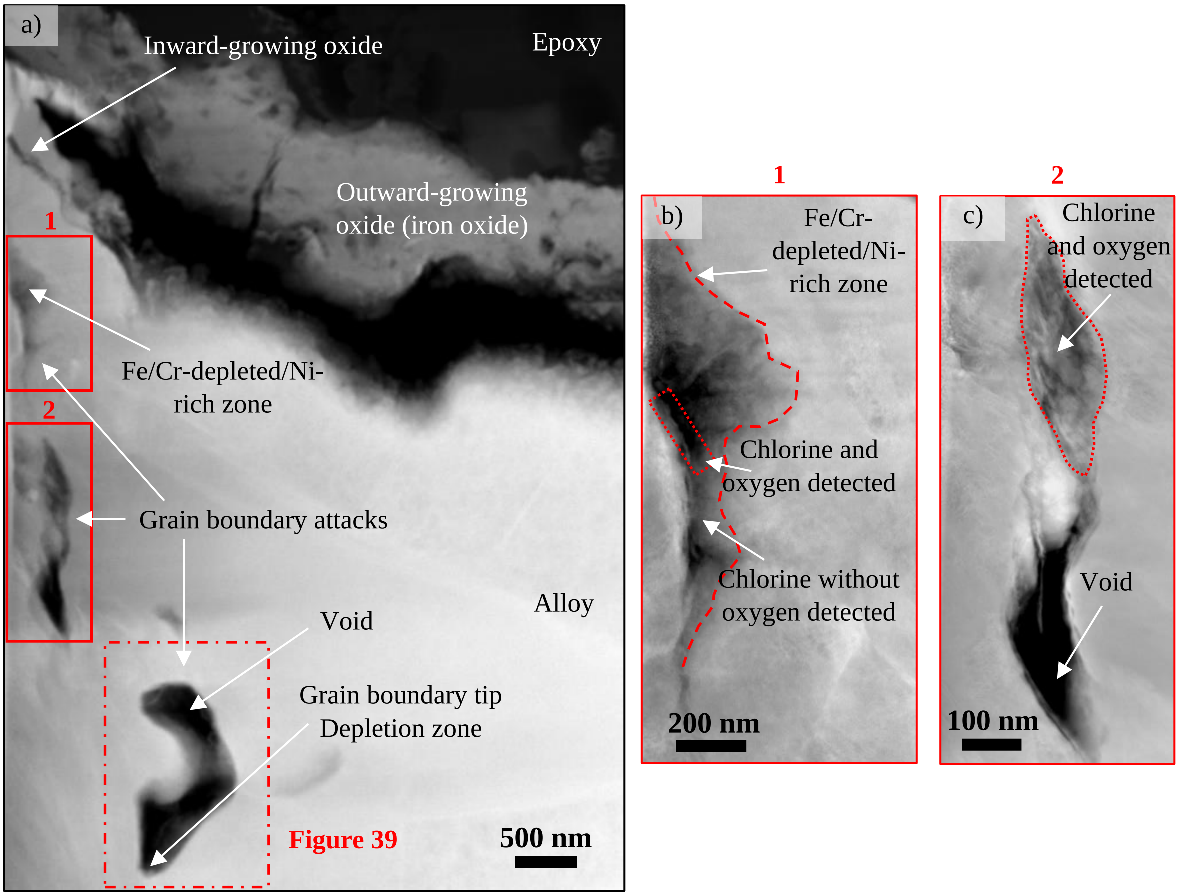

Figure 38: a) Micrograph showing the HAADF image of thin FIB lamella lifted out from a grain boundary attacked region from a 304L sample exposed to 5% O_2 + 20%H_2O + N_2 (bal.) under continuous KCl deposition at 600 °C for 1 hour (red box labelled "TEM lamella" in Figure 36c; b) High magnification image of the beginning of the grain boundary attack, close to the metal/oxide interface; c) High magnification image of the apparent middle section of the grain boundary attack.

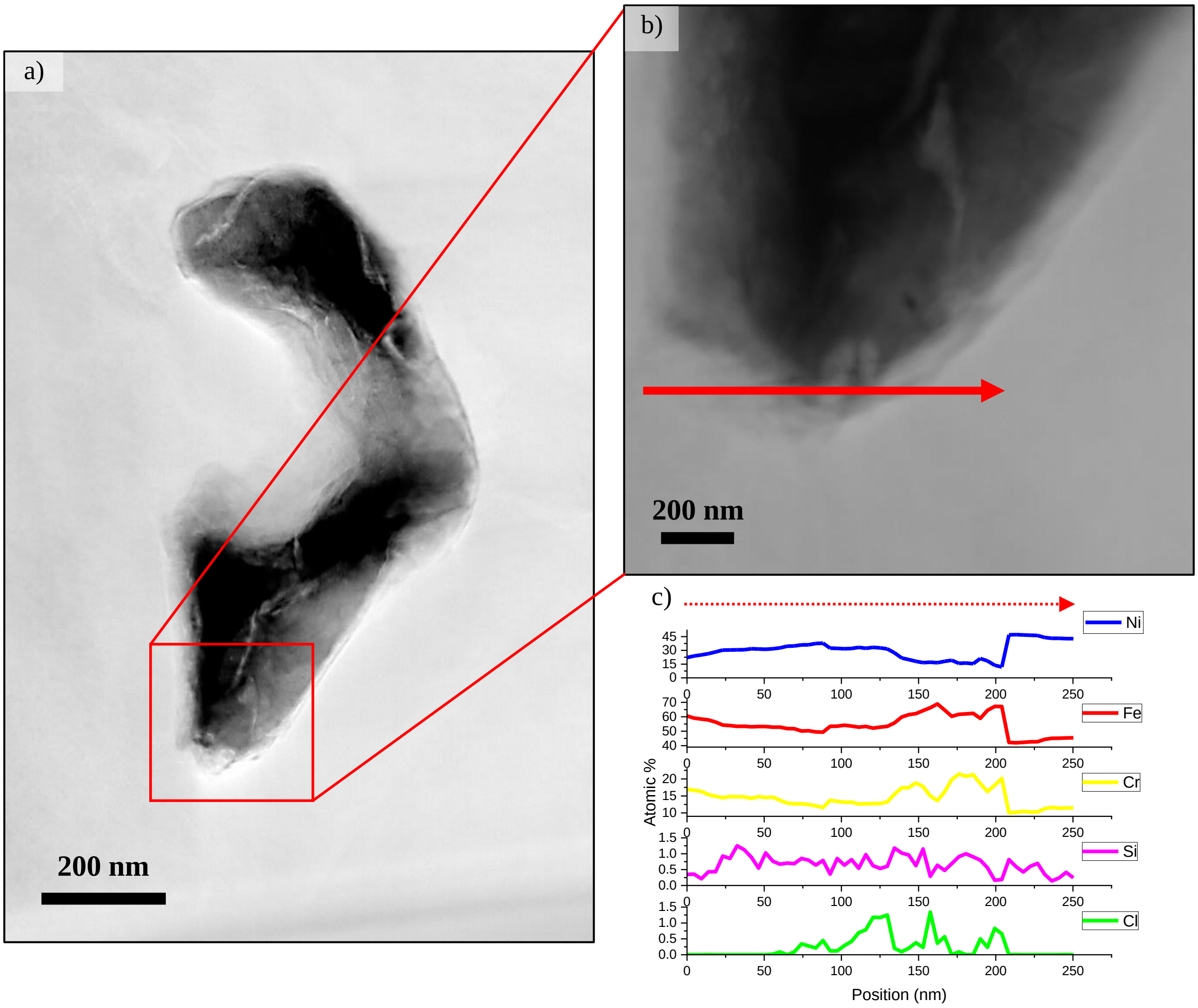

Figure 39: a) High magnification image of the lower region of the grain boundary attack in Figure 38a (dotted red square); b) high magnification image of the apparent tip of the grain boundary attack showing a STEM-EDX line scan with the red arrow, and c) result of the STEM-EDX line scan (at.%)

The detailed TEM analysis showed the presence of surprisingly long depletion zones in the vicinity of the grain boundary attack. These zones were larger close to the metal/oxide interface (300-600 nm, see Figure 40) and shorter close to the tip of the grain boundary attack (110-300 nm, see Figure 41).

The 2D representation of the 3D voids can somewhat overestimate the length of the depletion zones. A large number of analysis were therefore performed and interpreted to verify the approximate lengths. It should be noted that the depletion zones were associated with very small levels of Cl. The presence of Cl was identified by investigating the EDX data (peaks/noise ration) and not by quantification, even though the results are presented as at.% in the line scans in order to illustrate the presence of Cl. Both iron and chromium were depleted, and nickel accumulated in these regions. Several alloy grain boundary regions ahead of the corrosion front were investigated, and their composition was found to be similar to the original composition of the alloy even if some Cl could be detected in the grain boundary ahead of the corrosion front. Similar large depletion zones of iron and chromium have previously been reported for the stainless steel Sanicro28 after exposure to a similar environment [119].

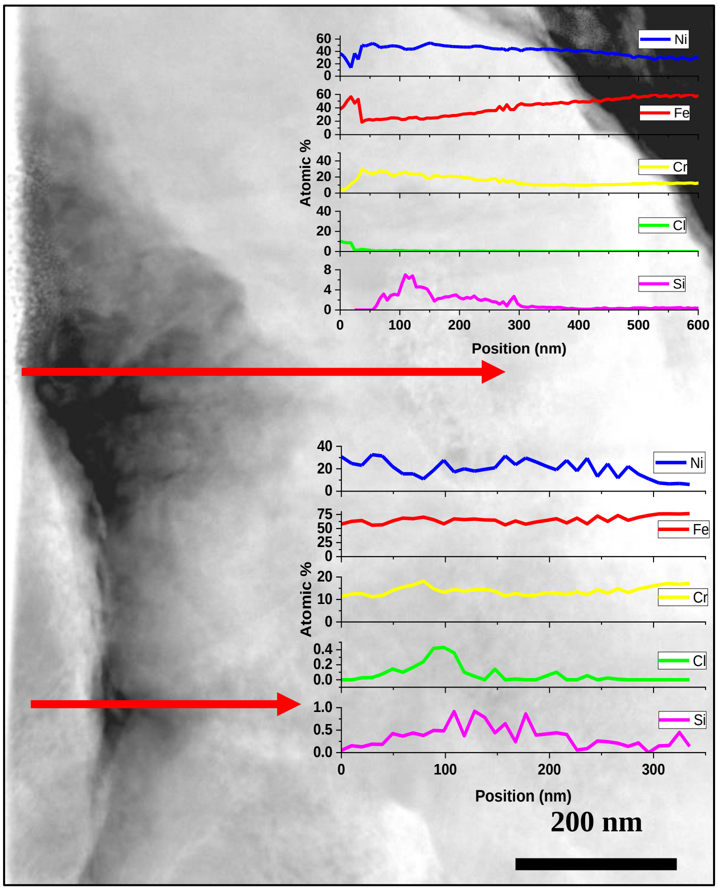

Figure 40: High magnification image of Figure 38b showing two STEM-EDX line scans with the red arrows(at.%).

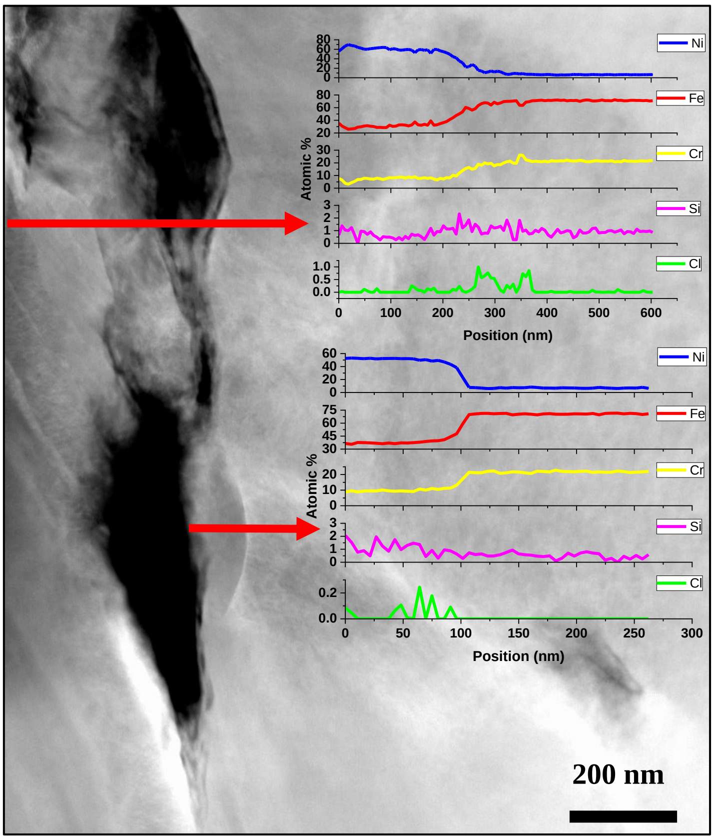

Figure 41: High magnification image of Figure 38c showing two STEM-EDX line scans with the red arrows(at.%).

The bulk diffusivity of chromium in 304L at 600 °C was predicted using data depletion zones from a stainless steel at different temperatures to interpret the depletion zones. After a one-hour exposure at 600 °C, the calculated depletion zone was in the range of a few nanometers, i.e. several orders of magnitude lower than the depletion zones measured in this study, i.e. from the grain boundary region and into the neighboring alloy grain. The length of the depletion zones in connection to the grain boundaries of the 304L in this study, i.e. exposed to a KCl-rich environment at 600 °C, can be compared to the behavior of materials exposed to higher temperatures where the diffusivity would be higher. Very similar type of microstructure, i.e. large empty voids at alloy grain boundaries, could be observed without the presence of Cl, at 800 °C see e.g. [120]. Thus, the results indicate that a local enrichment of Cl at the grain boundary regions may increase the diffusivity of alloying elements. Initially increasing the diffusivity in grain boundary regions promotes the formation of voids and new surfaces where even faster surface diffusion is expected. Accumulations of Cl (metal chlorides) on top of grain boundary regions has earlier been observed with TEM during the initial oxidation of a stainless steel exposed at 500 °C in the presence of HCl [61]. A similar sample preparation/handling approach was used in this study, which found that no large amounts of metal chlorides were lost during sample preparation. The results of the microstructural investigation gave a good representation of the Cl distribution at the grain boundary attack.

Propagation of a grain boundary attack (24-hour exposure)

The SEM-BSE/TEM investigation found the presence of a thicker scale after a 24-hour exposure with the same type of microstructure covering the alloy as earlier (dual oxide scale), i.e. secondary protection. The thickness of the secondary oxide scale was in the same range as an oxide scale formed on regions without any alloy grain boundary attack [117]. However, the inward-growing oxide scale on top of the alloy grain boundary regions exhibited two domains: a top part that was a homogeneous oxide layer attached to the outward-growing oxide scale, and another part that was heterogenous with a chromium/iron-rich matrix with large nickel-rich nodules, see Figure 43. This type of morphology has been observed in the corrosion front of the 304L stainless steel after 24-hour exposures to several environments (i.e. Fe-Ni metal mixed with the internal oxidation of Fe-Cr oxide) on a much smaller scale [27, 121]. The SEM/BSE images indicate the presence of this type of microstructure (light grey part of the inward-growing oxide scale) in the middle of alloy grains, see Figure 42c. However, TEM is required to reveal the fine details of the microstructure.

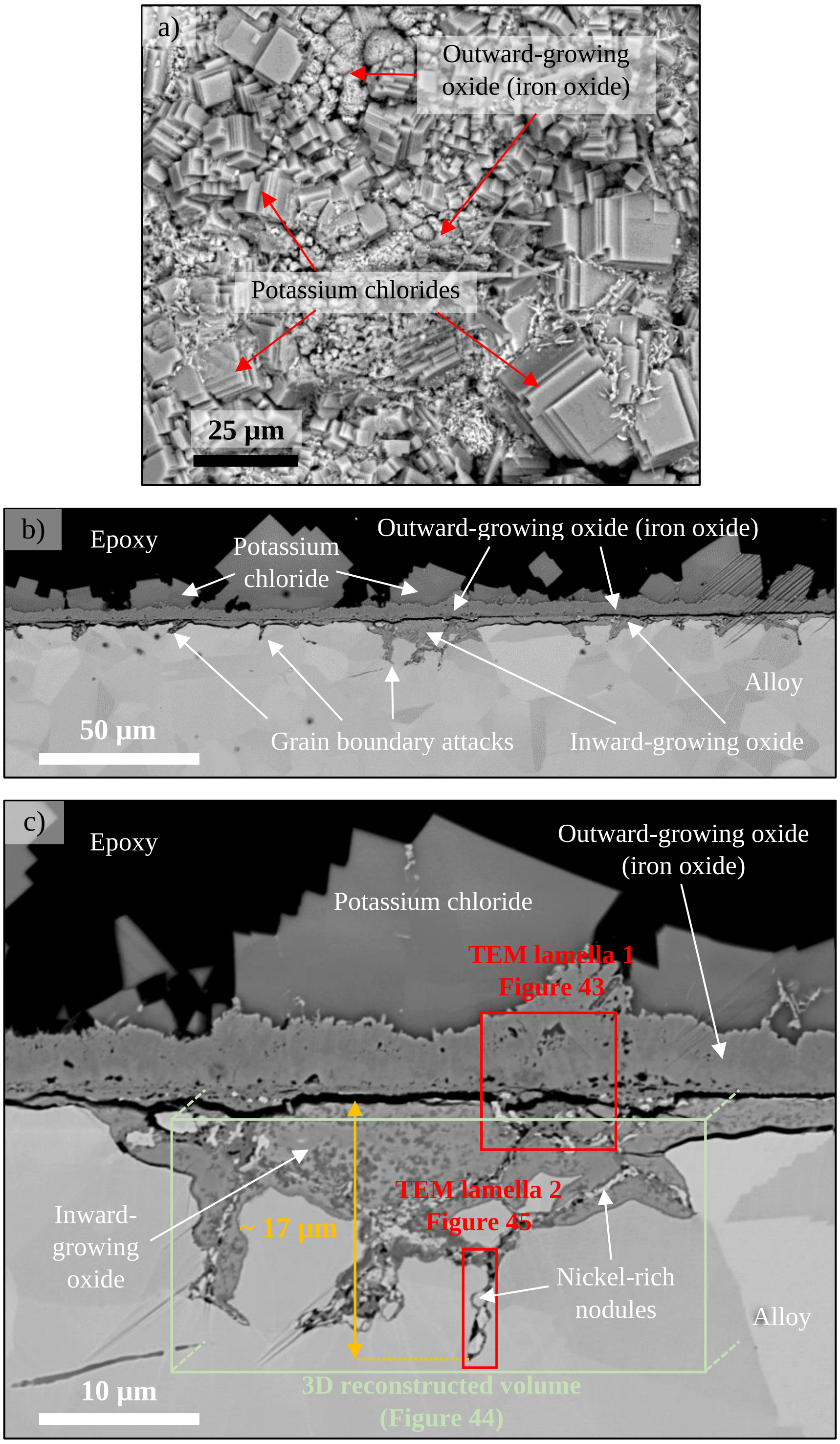

Figure 42: SEM images using BSE of a) plan view, b) low magnification, and c) high magnification cross-sections of a 304L sample exposed to 5% O_2 + 20% H_2O + N_2 (bal.) under continuous KCl deposition at 600 °C for 24 hours. The marked region (green box) refers to the area and volume investigated via 3D tomography (see Figure 44), while the marked red box labelled "TEM lamella 1" refers to a typical metal/oxide interface area investigated via TEM (Figure 43). The marked red box labelled "TEM lamella 2" refers to a typical grain boundary attack area investigated via TEM (Figure 45). The yellow measurement annotation refers to the maximum depth of the grain boundary attacks in this area.

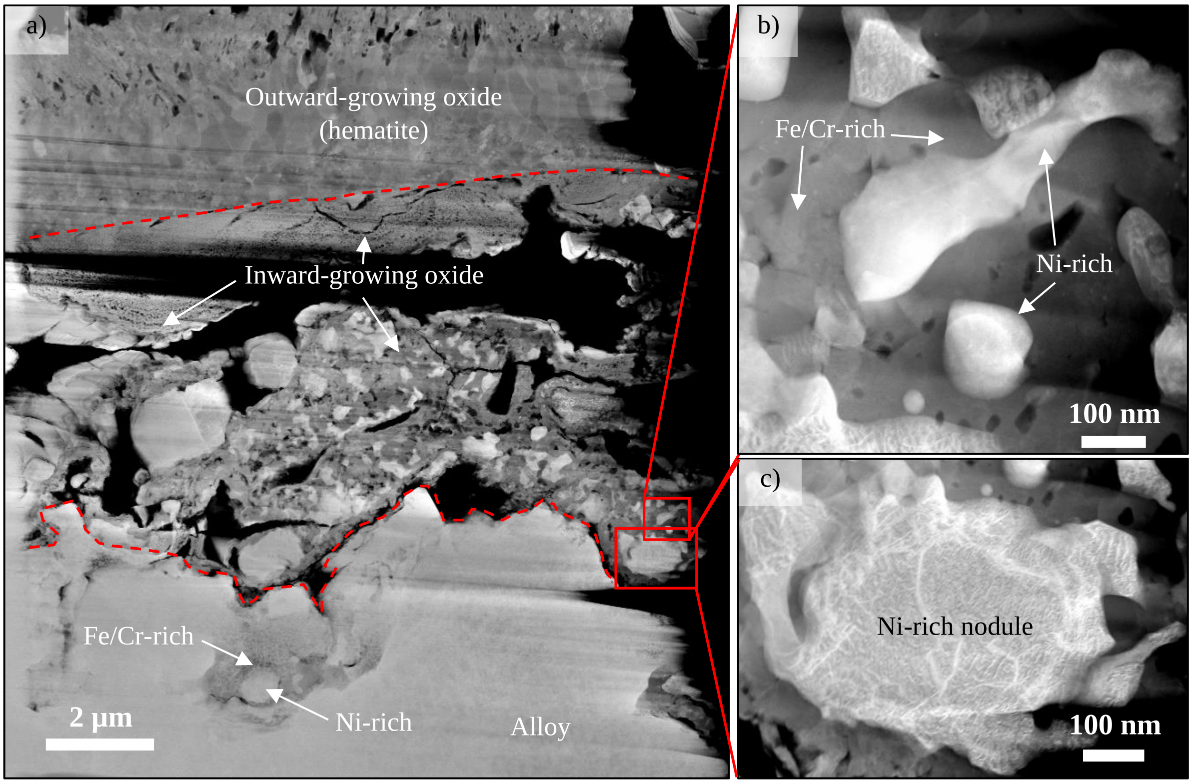

Figure 43: a) Micrograph showing the HAADF image of a thin FIB lamella of 304L sample exposed to 5% O_2 *+ 20%*H_2O *+* N_2 *(bal.) at 600 °C for 24 hours under continuous KCl deposition (red box labelled "TEM lamella 1" in Figure 42c; b) high magnification image of the typical inward-growing oxide region showing Cr-rich (in grey) and Ni-rich nodules (in bright), and c) high magnification of a Ni-rich nodule.*

After 24 hours, the grain boundary attack showed a wide range of depths (8 to 50 µm, see Figure 42 and [117]). The growth rate of the grain boundary attack after initiation (1 hour) remained high even if it was challenging to determine a typical growth rate due to the complex 3D structure of a grain boundary. After the initial hour of exposure, a grain boundary attack that was up to 3 µm down from the surface was observed, while the attack had reached 50 µm after 24 hours. The 3D tomography analysis revealed the presence of voids close to the interface of the alloy/secondary oxide scale and at the tips of grain boundary attack (approximatively at 17 µm from the interface of the secondary oxide scale), see Figure 44a. However, no clear connections between these two clusters of voids was observed after 24 hours as the middle/upper parts had been oxidized. This contradicted the potential of connected voids to be considered as fast pathways for the diffusion of species. The middle part of the grain boundaries was filled with brittle/shattered oxide and nickel-rich nodules. The network of Ni-rich nodules was observed in the 3D representation, see Figure 44b, that covered a large fraction of the grain boundary regions. The TEM analysis showed that the Ni-rich nodules contained some iron and that the oxide found in the grain boundaries was heterogeneous in composition, i.e. either iron- or chromium-rich, see Figure 45. The presence of trace amounts of Cl was once more detected with oxygen within such a grain boundary. The absence of nickel in the oxide of the grain boundary regions indicates an activity of oxygen below 10^{-21}(using thermodynamic calculations) in these regions [27]. This implies that the secondary oxide scale on top of the grain boundary regions as intact as the oxygen activity remained low below this scale.

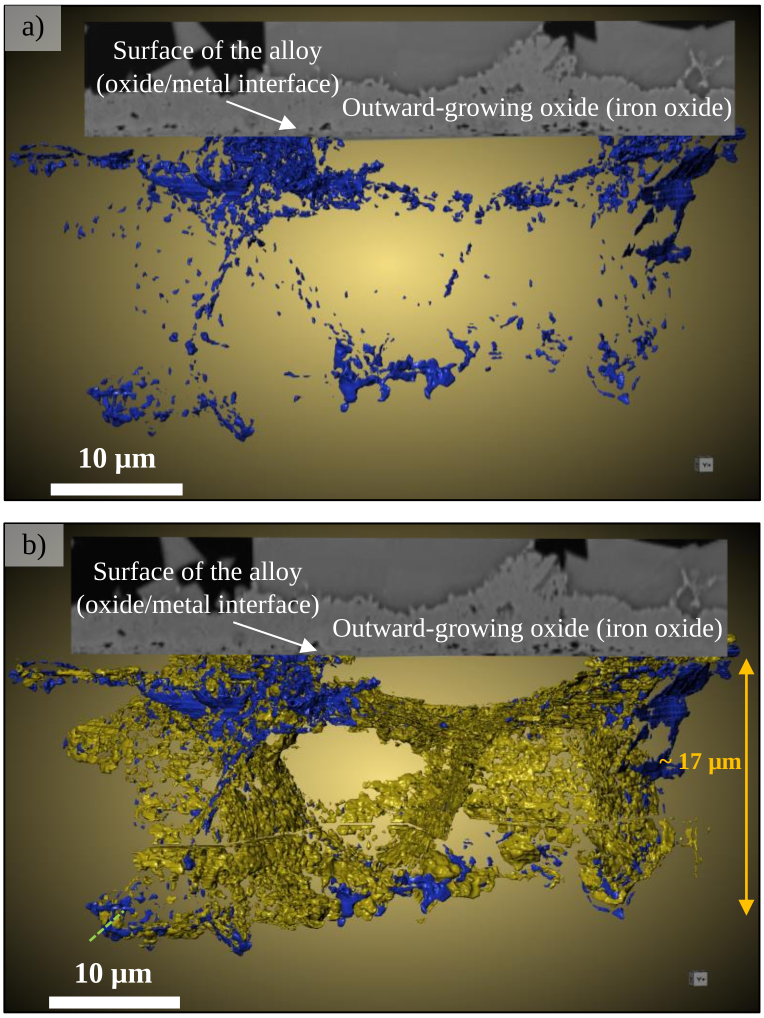

Figure 44: a) 3D tomography of the voids from the area highlighted by the green box in Figure 42c, and b) the same 3D tomography with the addition of bright nodules (nickel-rich).

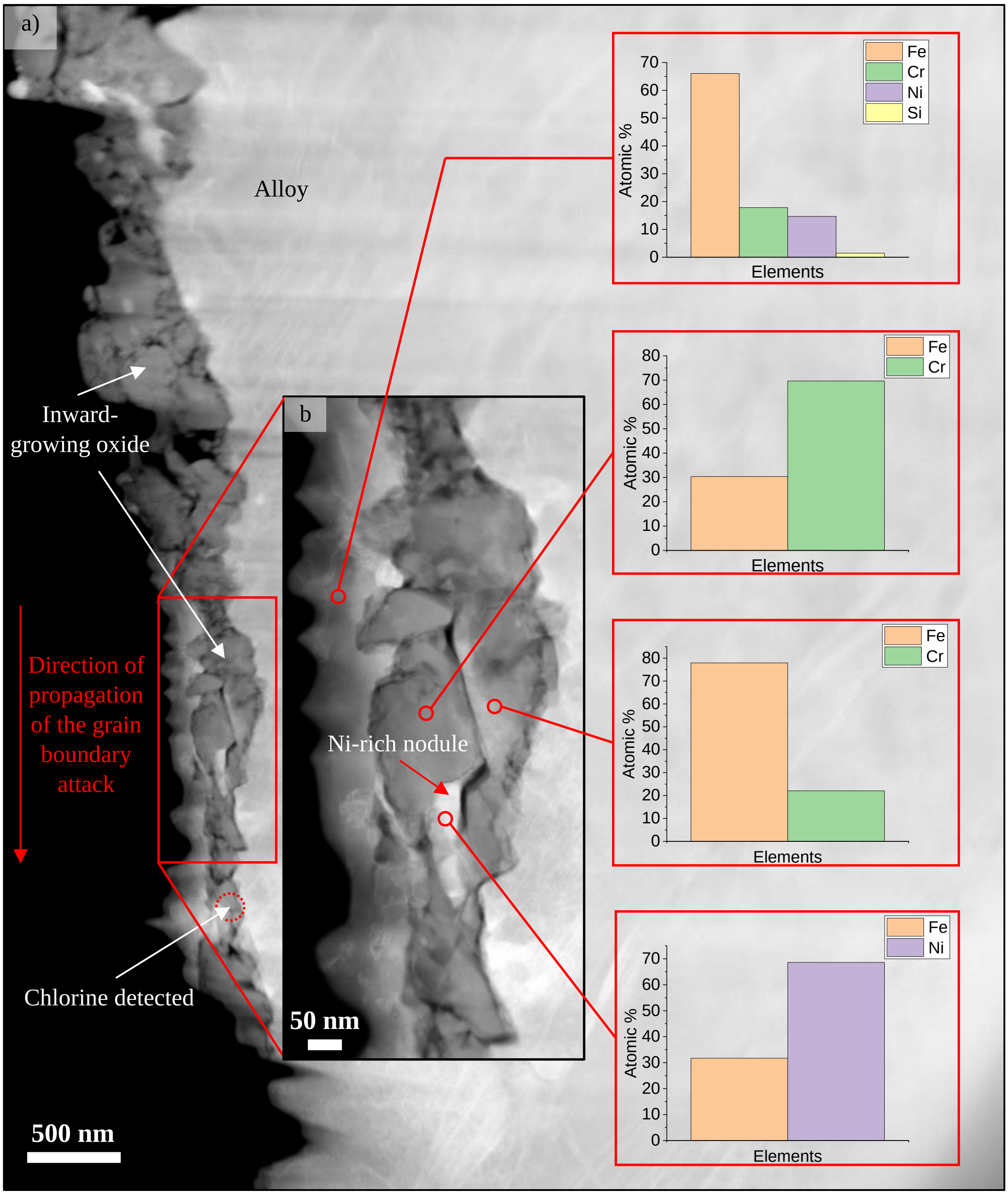

Figure 45: Micrograph showing the HAADF image of thin foil (a) lower, and b) higher magnification image of a grain boundary attack from a 304L sample exposed to 5% O_2 + 20%H_2O + N_2 (bal.) for 24 hours at 600 °C under continuous KCl deposition (red box labelled "TEM lamella 2" in Figure 42c. Locations of quantitative analyses and their corresponding results are represented in at.%.

The investigation of the alloy grain boundary regions after a 24-hour exposure showed a microstructure indicating fast diffusion (larger expected features in a diffusion-grown microstructure) at and in the vicinity of the alloy grain boundaries, see Figure 42c. The 3D information in addition revealed large Ni-rich regions (Ni/Fe metal shown with TEM). The 3D analysis indicated that voids were present at the grain boundary corrosion front. The microstructure of the oxide scales formed in the formerly empty grain boundary regions indicates a diffusion grown scale with varying Cr/Fe ratios. This would be expected since some parts of the 1-hour exposure must have been depleted of Fe/Cr prior to oxidation, see results from 1-hour exposure. Cl was again found close to the corrosion front as well as in the grain boundary ahead of the corrosion front even if the presence of Cl was harder to determine after longer exposure times due to the complex structure and the small amounts. The results in addition showed that after trace elements (Si and S) from the alloy had accumulated at the alloy grain boundaries after 24 hours, see Figure 46a and b. This would be expected after longer exposure times at higher temperatures, and this accumulation would be expected to increase the diffusivity at grain boundaries. However, no indications of any Cr-rich phases (e.g. carbides) were observed.

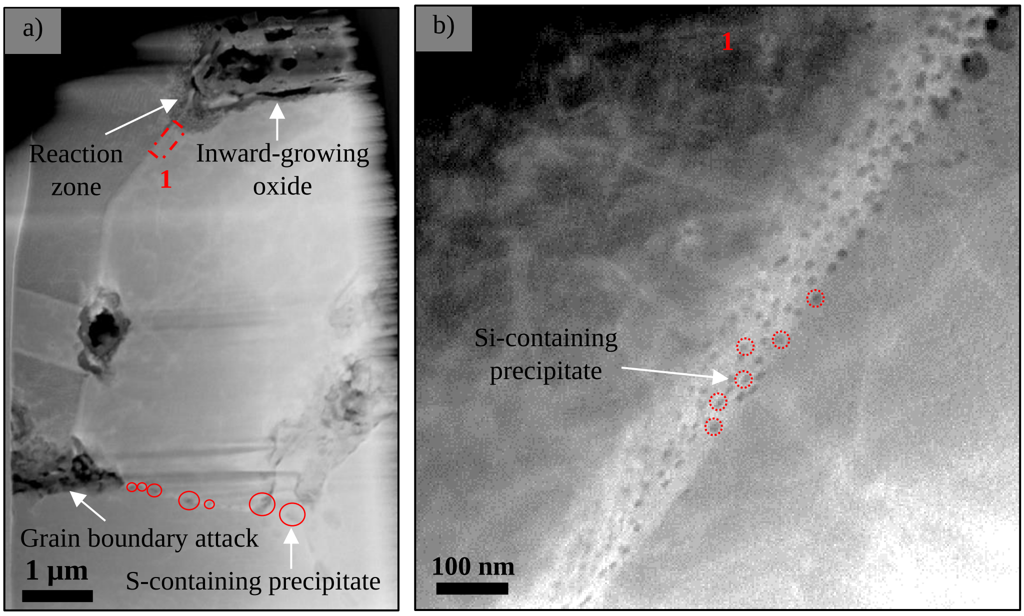

Figure 46: a) Micrograph showing the HAADF image of thin foil and b) showing the segregation of Si precipitates at a non-attacked grain boundary.

A deep grain boundary attack can drastically increase material degradation due to the loss of sound material, even if a grain has not been fully oxidized, see e.g. [118]. A deep grain boundary attack implies that other corrosion mechanisms are involved in the corrosion attack, i.e. another regime of corrosion has begun. The literature survey in combination with the present findings indicate that this type of material degradation can be caused by high temperature ([120]) or a combination of temperature and environment. The ageing of material and the formation of, e.g. a Cr-rich precipitate, have been suggested to cause a selective attack (see 9.1.3). However, no indication of this behavior was found in the present study [100].

The oxide microstructure formed after breakaway has been described to be generic for a wide set of FeCr, FeCrNi and FeCrAl alloys [116]. This implies that corrosion after breakaway can be modeled similarly for many Fe-based alloys using generalized modeling tools. However, the very localized material degradation below an intact secondary scale described in the present study must be accounted for. It is necessary to improve the understanding of the corrosion mechanisms in corrosion beyond the secondary corrosion regime in order to better predict the corrosion behavior of materials. However, the very localized and complex geometry and/or small scale of the corrosion attack makes this a challenge to study.

This study shows that a combined 3D-FIB/TEM investigation has a great potential in investigating and characterizing such a complex corrosion attack. The initiation (1-hour exposure) and propagation (24-hour exposure) of the grain boundary attack occurred very rapid below an intact secondary protection. In addition, the presence of large depletion zones associated with large features of the microstructure indicate a fast diffusion of ion species.

9.1.3. Influence of the microstructure and environment on the KCl-induced corrosion attack

It is well-known that laboratory investigations allow the study of different parameters due to a well-controlled environment. However, some parameters may remain a challenge to investigate. For instance, KCl can be introduced in various ways to the surrounding environment to simulate a more corrosive one. The salt can be applied by spraying a salt-containing solution onto a vertical sample [86], or it can be deposited as a slurry on top of a horizontal sample [100], or even introduced as a gas phase by placing a sample above a KCl-containing crucible [18]. In this study, two ways of introducing salt into the environment (pre-deposited slurry onto samples vs continuous condensation onto samples) were employed to investigate the effect of α-Cr precipitates on the KCl-induced corrosion attack, i.e. to investigate a combination of environment/material ageing. This difference in methodology resulted in differences in the morphology of the corrosion attack.

The full study performed by DTU [100] investigated two nickel-based materials with different chromium contents: Ni35Cr4Nb and Ni45Cr4Nb (see Table 2). Two heat treatments were performed as well to generate different amounts of α-Cr. The aim was to study the influence of α-Cr on the KCl-induced corrosion attack. The summary of the research strategy of this paper is described in 8.1. However, within the scope of the collaboration between DTU and CTH, the study was focused only the material Ni35Cr4Nb and a comparison between the two methods of applying salt onto samples to investigate the KCl-induced corrosion attack, i.e. to investigate a possible combined effect of changes in microstructure/environment.

- Microstructure prior to exposure [100]

Thermodynamic calculations, heat treatments, and microstructural investigations were performed by DTU to predict the different amounts of α-Cr phases generated during the different heat treatments. A single main phase (FCC) was predicted for the solution treatment temperature (1100 °C), and three main phases (FCC, α-Cr and δ-Ni_3Nb) were predicted for the aging temperature (650 °C). The calculated fractions of α-Cr and δ-Ni_3Nb were, respectively, approximatively 0 wt.& (both phases) for the solution-treated sample and 12.2 % and 10.9 wt.%. for the aged sample. The short-term aging performed after the solution treatment (700 °C for 9 hours) was not considered in the thermodynamic equilibrium calculations.

These thermodynamic equilibrium calculations were performed using Thermo-Calc software version 2017b with the TT Ni-alloys v4.0 (TTNi4) or TCNi5 databases.

The observations in the SEM images were in good agreement with the thermodynamic calculations. The solution-treated sample (and short-term aged one) did not exhibit any tremendous amount of α-Cr nor δ-Ni_3Nb (see Figure 47a)). However, a little precipitation of these two phases occurred at the grain boundaries due to the thermal aging that followed the solution treatment. The precipitates that were darker than the matrix were α-Cr and the precipitates that were brighter were δ-Ni3Nb. For the thermally aged sample, FCC, α-Cr and δ-Ni_3Nb were observable (see Figure 47b)). The microstructure displayed heterogeneities in the distribution and size of the precipitates. The presence of fine and coarse α-Cr, granular and needle-shaped α-Cr, and the development of coarse α-Cr particles adjacent to the δ-Ni_3Nb phase were some of the microstructural heterogeneities observed. From a diffusion perspective, the presence of a precipitate generates an interface between the surrounding matrix (or other precipitates) and the precipitate. This interface can then be considered as a small pathway allowing fast diffusion of species, as a grain boundary would act. The high amount of observable precipitates in the heat-treated sample may therefore suggest the presence of numerous pathways for fast diffusion within the grains. In a similar way, the few observable precipitates gathered at the grain boundaries in the solution-treated sample may as well enhance the fast diffusion properties of the grain boundaries by contributing with new interfaces and therefore "broadening" the grain boundaries.

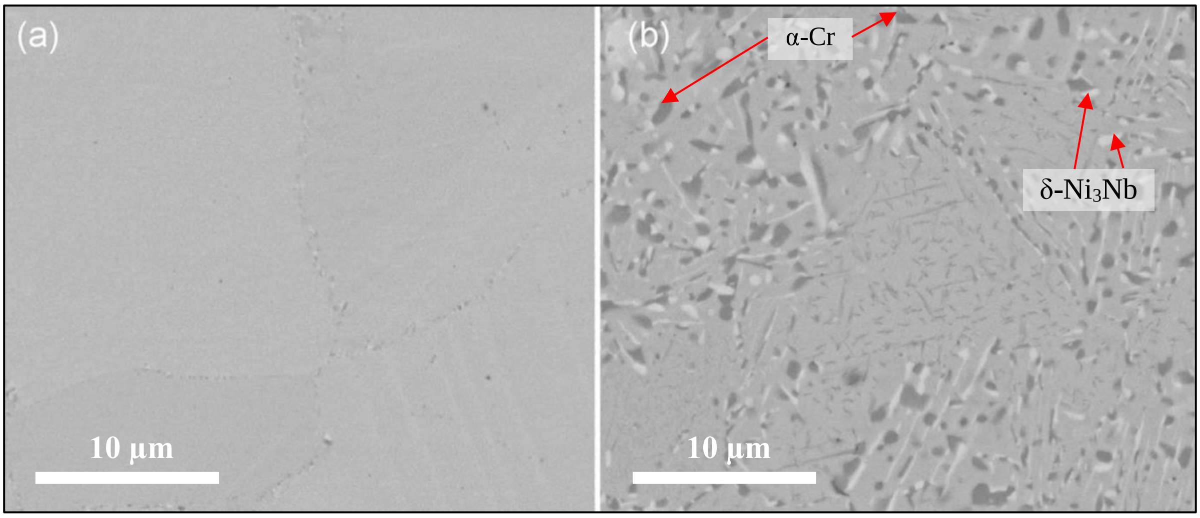

Figure 47: SEM images using BSE of the plan view of Ni35Cr4Nb a) solution-treated and b) aged [100].

- Microstructure after exposure

Pre-deposited KCl exposures (168-hour exposures)[100]

The standard way of depositing KCl was first investigated by DTU. For the solution-treated sample, the cross-section revealed that the outer scale consisted of a layer of potassium chromate and the inner scale of alternate layers of Ni-rich and Cr-rich oxides. It was suggested that oxidation of each metal chlorides occurred due to the preferential oxidation/chlorination of chromium. As the chromium was more homogeneously distributed in this sample, the corrosion front consisted of an area uniformly enriched in nickel and depleted in chromium.

The cross-section of the aged sample revealed a different morphology. The outer layer consisted of a potassium chromate layer mixed with "threads" of Cr_2O_3. Similar threads of iron oxides have been observed in a 18%Cr steel [122].

However, the internal attack on the aged sample displayed two different morphologies: a selective attack on α-Cr and dissolution of α-Cr. The selective attack can be explained by the high amount of chromium in α-Cr precipitates, which may react with chlorine. When a selective attack occurs, the presence of chlorine in the area would support the vulnerability of α-Cr precipitates towards chlorination (see Figure 48). The selective attack resulted also in the formation of pores/voids.

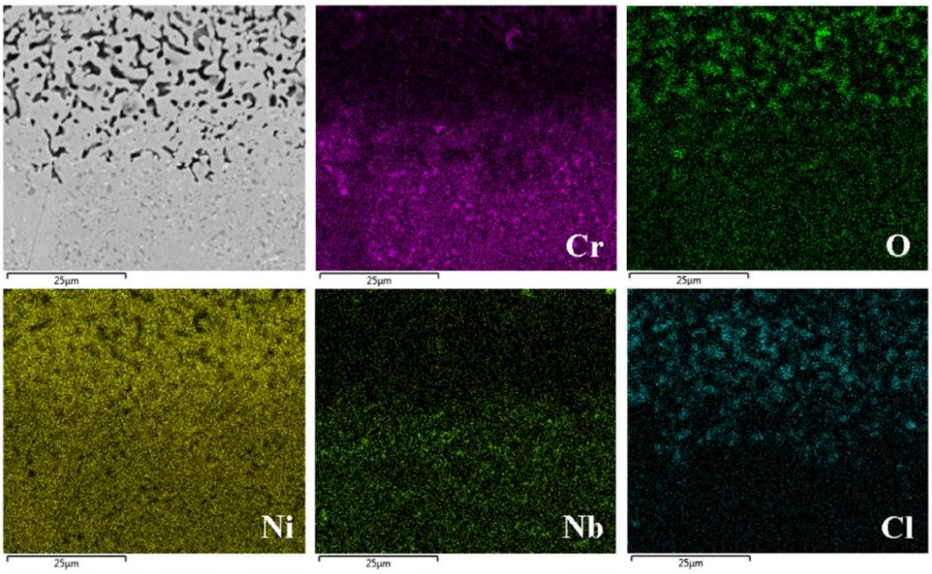

Figure 48: SEM image using BSE and EDX maps at the corrosion front of the aged Ni35Cr4Nb alloy exposed with pre-deposited KCl for 168 hours at 600 °C in 5% (vol/vol) O_2 (g) + 15% (vol/vol) H_2O + N_2 (g; balance) atmosphere [100].

The second morphology of internal attack observed was the phase dissolution of α-Cr precipitates. This phenomenon occurs in multiphase alloys when the main reactive solute of a precipitate is depleted from the matrix, e.g. to form corrosion products, or when the content of the main reactive solute in the matrix decreases until it reaches below the solubility limit of the solute in the matrix. The precipitates become unstable leading to dissolution [123]. Thus, in some areas of the aged sample, the α-Cr precipitates were no longer observable after exposure.

The existence of these two morphologies of internal attack may be due to the heterogeneities in the distribution and size of the precipitates. For instance, coarse precipitates would be more prone to selective attack due to their large supply in chromium, while fine particles would be easier to dissolve. A similar trend was investigated on the size of chromium carbides for their dissolution in the high-temperature oxidation of iron-based alloys [124].

Overall, the two heat treatments in the case of the alloy Ni35Cr4Nb resulted in two different microstructures: one approximated to α-Cr free in the matrix (solution-treated) and one with a 12.2% volume fraction of α-Cr in the matrix (aged). In both cases, the corrosion attack was initiated by the formation of potassium chromates and is suggested to advance via active oxidation. However, more investigations are required to confirm the clear occurrence of active oxidation.

Exposure under continuous deposition of KCl (24-hour exposures)

Severe spallation of the outer layer was observed on the solution-treated sample. This layer consisted of a layer of potassium chromate on top of a layer of chromia, see Figure 49a). This implies that 24 hours were sufficient to initiate accelerated corrosion. The corrosiveness of the environment simulated by this setup was demonstrated previously in another study (see 9.1.1) and is in good agreement with this study. The internal attack was represented by a porous region reaching down to 10 µm that was depleted in chromium (Figure 49b)). The reasons behind this morphology remain uncertain as it cannot be explained by a selective attack on chromium due to the lack of α-Cr precipitates. However, the EDX map in Figure 49c clearly shows an area depleted in chromium where this morphology is observable. This was also observed in the previous study (see 9.1.1) where the nickel-based alloy Inconel 625 exhibited an internal attack via void formation. This chromium depletion in alloy Ni35Cr4Nb resulted in an enrichment of nickel in the attacked area. These observations have been previously reported in other studies [18, 125, 126]. The two-dimensional aspect of the analysis cannot reveal if the voids/pores were connected, which would make them gas permeable channels. A combined 3D tomography and TEM characterization could be considered for future characterizations to unravel the connectivity and nature of these voids, as demonstrated in the investigation in 9.1.2.

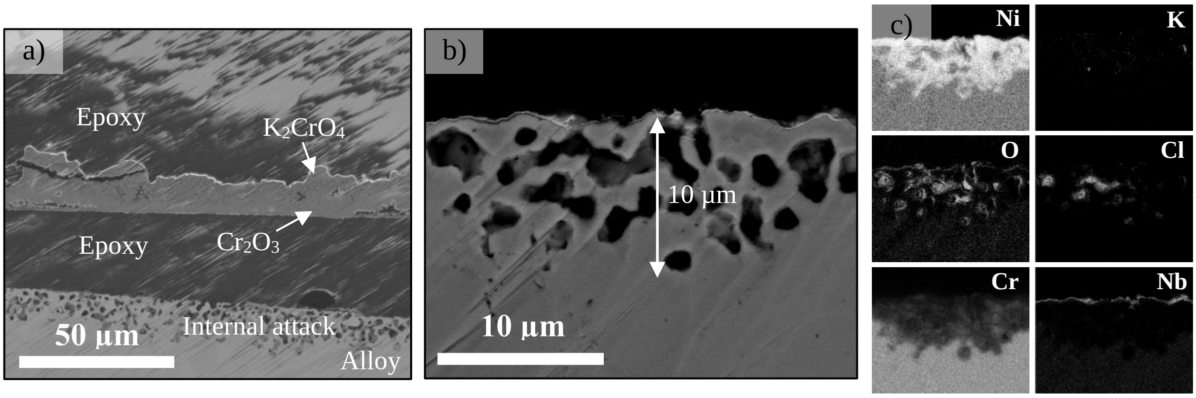

Figure 49: a) and b) BSE images of the solution-treated Ni35Cr4Nb exposed for 24 hours under continuous KCl deposition in5% (vol/vol) O_2 (g) + 15% (vol/vol) H_2O + N_2 (g; balance) atmosphere. c) EDX maps of b) [100].

The outer layer of the aged sample consisted of a thick layer of potassium chromate with threads of chromia as previously observed by DTU. The thicknesses of the outer layers were somehow similar between the solution-treated and aged samples (20-25 µm). However, the depth of the internal attack was three times deeper for the aged sample (~ 30 µm) than for the solution-treated sample (~ 10 µm). The internal attack also differed in uniformity. The solution-treated sample exhibited an internal attack nearly uniform, while the aged sample exhibited a high irregularity (see Figure 50 with red dashed zone). This can be explained by the difference in microstructure between the two samples. The solution-treated sample displayed a microstructure free from α-Cr precipitates, which resulted in an even distribution of the chromium within the matrix. However, the aged sample displayed a microstructure with approximatively 12.2% (volume fraction) of α-Cr precipitates, which resulted in a selective internal attack. Both samples underwent a preferential internal attack towards chromium, which resulted in void formation. However, the attack occurring in the solution-treated sample was mainly due to the removal of chromium from the uniform matrix, while the selective attack of the chromium from the α-Cr precipitates occurred in the aged sample.

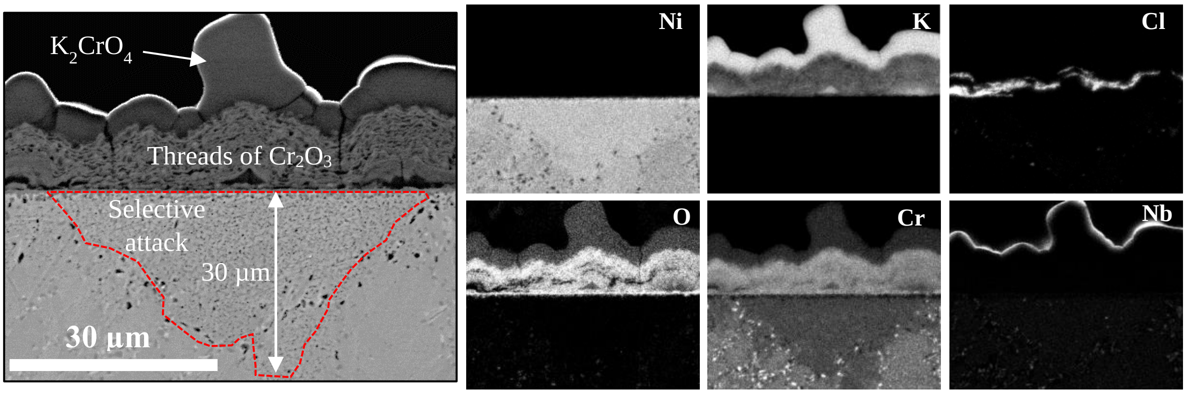

Figure 50: SEM image using BSE and EDX maps of the aged Ni35Cr4Nb exposed for 24 hours under continuous KCl deposition in5% (vol/vol) O_2 (g) + 15% (vol/vol) H_2O + N_2 (g; balance) atmosphere. The Nb signal could be a false signal that overlaps with sputtered gold.

Comparison of the results between the two methods of applying salt

Overall, the two methods of applying salt led to similarities in corrosion attack as well as some interesting differences. One of the similarities was the comparable outer layer. In both cases, a build-up of potassium chromate was observed on top of the chromia (solution-treated) or embedded in it as threads (aged). This indicates the occurrence of alkali chromate formation and consequently, the initiation of accelerated corrosion. The major difference is in the internal corrosion attack.

When KCl was pre-deposited onto the solution-treated sample, this resulted in an internal attack represented by a uniform depletion of chromium. When KCl was added continuously via condensation, this also resulted in a uniform depletion zone but paired with void formation. This difference can be explained by the higher amount of KCl surrounding the alloy, thus inducing a higher flux of chromium towards the metal/oxide interface as well as a stronger presence of chlorine species (HCl or Cl_2). This combination could lead to an even more accelerated corrosion attack.

Differences in the severity and morphology of corrosion attacks between laboratory experiments with relatively small differences in parameters resulted in major differences [18, 127, 128]. However, the referred studies have reported that the exposures performed with KCl in gaseous phase via sublimation resulted in a more severe ([18]) or milder ([127, 128] corrosion attack compared to pre-deposited KCl. The exposures were performed in a static lab air environment to allow for the presence of gaseous KCl around the samples. A continuous gas flow was used in this stud instead with a source of KCl heated to 700 °C and samples heated to 600 °C. This allowed the continuous supply of KCl due to the flow towards the sample but also, and the thermal gradient acted as a driving force for the deposition of KCl onto the samples via condensation, thus inducing a more corrosive environment. This method better mimics the phenomenon occurring in a boiler that causes a more severe corrosion attack than pre-deposited KCl exposures [117].

The aged sample also exhibited some differences regarding the selective attack and dissolution of α-Cr. Mainly, both types of internal attack (selective attack and phase dissolution) occurred when KCl was pre-deposited while only the selective attack occurred when KCl was added continuously. This could be explained by the higher aggressiveness of the setup where phase dissolution could not occur fast enough to meet the demand for chromium (necessary for alkali chromate formation). However, the shorter duration of the exposure under continuous KCl deposition (24 hours) compared to the pre-deposited exposure (168 hours) could also explained the absence of phase dissolution. Thus, longer exposures under continuous KCl deposition are needed for a better comparison between the two methods.

The difference in simulating a corrosive environment resulted in a variation of the internal attack of both heat-treated samples. A chromium depletion zone paired with void formation was observed in the solution-treated sample exposed to a continuous deposition of KCl while only chromium depletion was observed when KCl was pre-deposited. The selective attack and phase dissolution of α-Cr precipitates were observed in the aged sample with pre-deposited KCl while only a selective attack was observed when the sample was exposed to continuous KCl deposition.

This collaborative work emphasizes the importance of the correlation between microstructure (the presence of α-Cr precipitates) and environment (the method of applying KCl).

9.2. Approaches to mitigate high-temperature corrosion

9.2.1. Mitigation of corrosion by improving materials: the use of coatings

It is well known that high-alloyed steels, considered as good corrosion-resistant materials, are more expensive than low-alloyed steels, which are considered as low-corrosion-resistant materials. The costs and the properties of a material are directly linked to the different alloying elements added during the fabrication of the material. However, the addition of alloying elements such as Cr, Si, Al, and Ni, to improve the corrosion properties of the final material also have an impact on the mechanical properties of the material, usually in a negative way [129-131]. This results in shorter lifetimes, lower pressure-bearing capabilities, and reduced fabricability. A solution to this problem can be the use of high-alloyed steels as coatings, instead of solid materials. The combination of the good corrosion properties of a high-alloyed steel as a coating with the good mechanical properties of a low-alloyed steel as a substrate could lead to an adequate solution, both technically and economically.

The use of coatings for corrosion resistance has been thoroughly investigated. Coatings are usually produced by using different thermal spraying techniques, such as arc spray or High Velocity Oxy Fuel (HVOF). The characterization of the produced coatings, however, revealed numerous problems regarding porosity, oxide formation during spraying, and poor adhesion of the coating on the substrate. Such issues usually result in coating failure towards corrosion resistance [102, 103]. Porosity plays a major role in coatings; the denser the coating, the better its performance. More recently, a new thermal spraying technique called High Velocity Air Fuel (HVAF) has been developed. This technique can produce coatings with low porosity, reduced oxide formation during spraying, and elemental loss [104, 132]. These advantages are achieved due to lower temperatures and higher particle velocities [106, 132, 133].

The present study investigated the protectiveness of three different HVAF-sprayed nickel-based coatings (NiAl, NiCr and NiCrAlY) exposed in two different laboratory environments: a mildly corrosive environment (consisting of $O_2 + H_2O$) [104] and a highly corrosive environment (consisting of $O_2 + H_2O + KCl$)[134]. The study was performed using gravimetry and microstructural analyses. As these coatings were designed for biomass- and waste-fired boiler purposes, environments with high levels of water vapor and corrosive species were laboratory replicated to mimic the conditions generated in these boilers.

An M3^{TM} HVAF gun was used to spray the three different coatings onto a 16Mo3 substrate. Grit blasting using aluminum oxide was performed prior to the thermal spraying in order to enhance the adhesion between the coating and the substrate. The remaining aluminum oxide could be observed at the coating/substrate interface.

Mildly corrosive environment: 5% O_2 + 20 %H_2O + N_2

In the absence of KCl, the samples exhibited mass gains between 0.1 and 0.2 mg/cm^2, see Figure 51. A sample of bulk 304L was also exposed to this environment (without KCl) as a reference and showed lower mass gains than the coated samples. The mass gains of the coated samples decreased slightly from NiCr to NiAl and finally NiCrAlY. The oxide thicknesses calculated from the mass gains were considered to be between 0.6 and 1.0 µm, considering nickel oxide (NiO) as the only oxide. However, the surfaces of the coated samples had a shiny appearance, the sign of a thin oxide in the range of 50 and 200 nm. This difference implies that oxidation within the coating occurred as no thick oxide could be found on the surface.

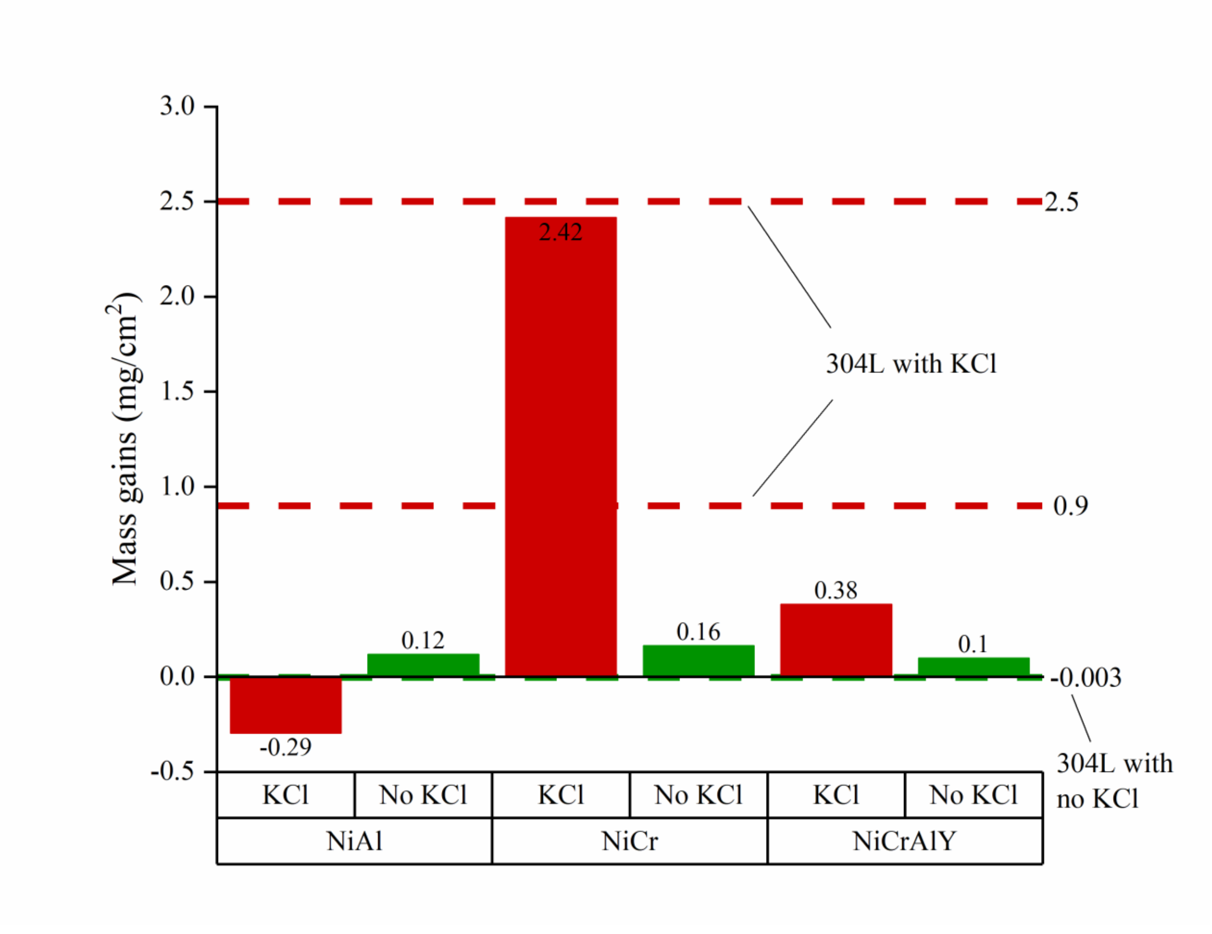

Figure 51: Mass gains of the coated samples after 168-hour exposure to 5% O_2 + 20% H_2O + N_2 at 600 °C with and without KCl. The dashed reference lines represent the mass gains of 304L in the presence of KCl (red dashed lines) and without it (green dashed line). The mass gains of 304L were calculated based on oxide thickness..

NiCr did not form a thick oxide on the surface, but oxygen was detected in the coating down to the coating/substrate interface (see Figure 52). As no oxygen was detected in the coating of a non-exposed sample (Figure 53), it can be concluded that oxide was formed during exposure and not during thermal spraying. The exposures of NiAl and NiCrAlY resulted in no signs of oxide formation within the coating (except for the aluminum oxide residues from the grit blasting). This implies that the mass gain measured was probably caused by flaws in the coatings that induced local corrosion attacks (Figure 54 and Figure 55).

Consequently, NiCr cannot be considered as a good potential coating because oxide formation occurred within the coating in this mildly corrosive environment. In contrast, NiAl and NiCrAlY were more promising due to the thin and protective oxides observed on the surface of the coatings as well as the absence of oxide within the coatings.

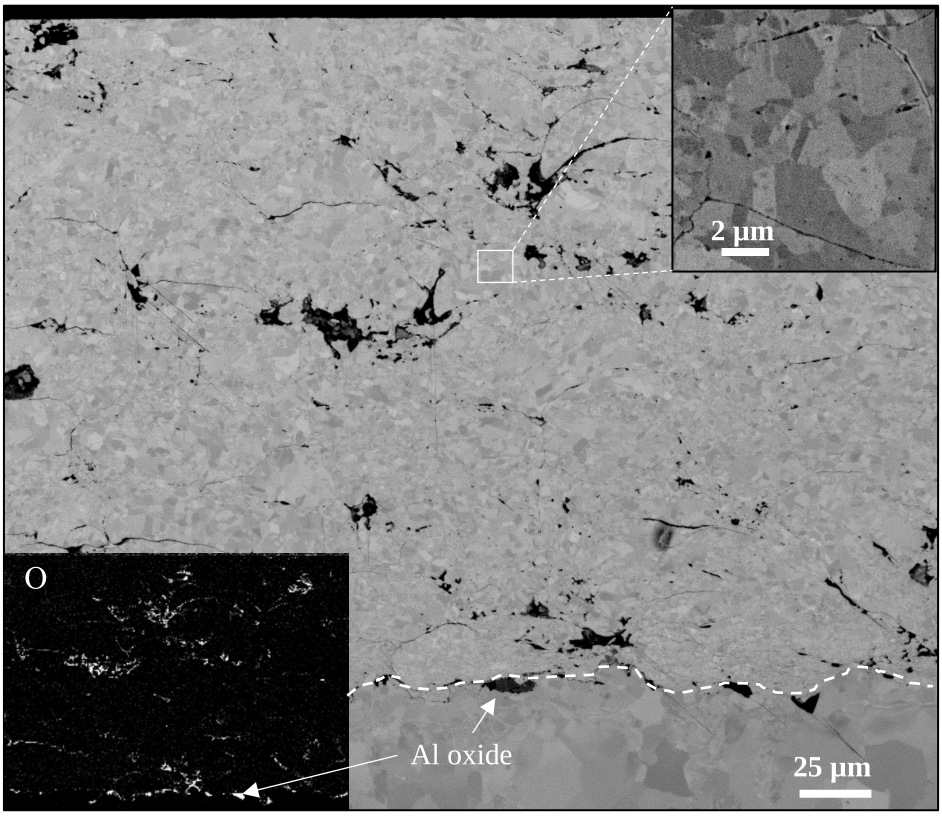

Figure 52:SEM image using BSE of a cross-section of a NiCr-coated sample after exposure to 5% O_2 *+ 20%* H_2O *+* N_2 *at 600 °C for 168 hours. The signal for oxygen from the EDX analysis is located at the bottom left of the picture. A higher magnification of a section of the coating is shown at the top right. The dashed line represents the coating/substrate interface.*

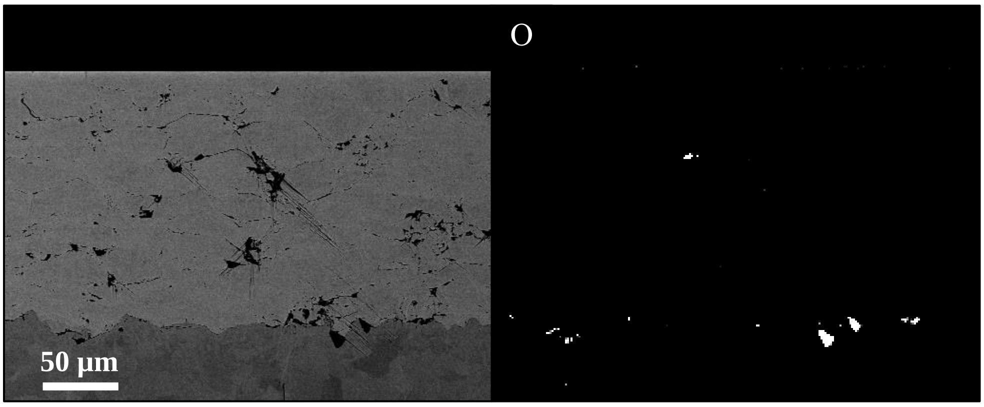

Figure 53: SEM image using BSE of a cross-section of a non-exposed NiCr-coated sample (left) and the signal for oxygen from the EDX analysis of the area (right).

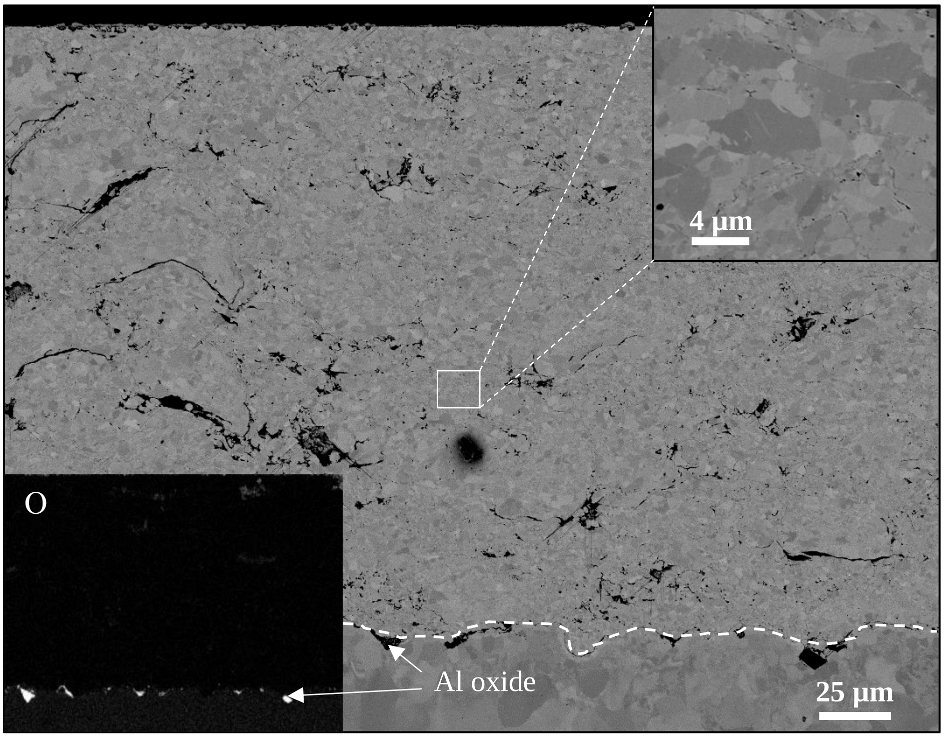

Figure 54: SEM image using BSE of a cross-section of a NiAl-coated sample to 5% O_2 *+ 20%* H_2O *+* N_2 *at 600 °C for 168 hours. The signal for oxygen from the EDX analysis is located at the bottom left of the picture. A higher magnification of a section is shown at the top right. The dashed line represents the coating/substrate interface.*

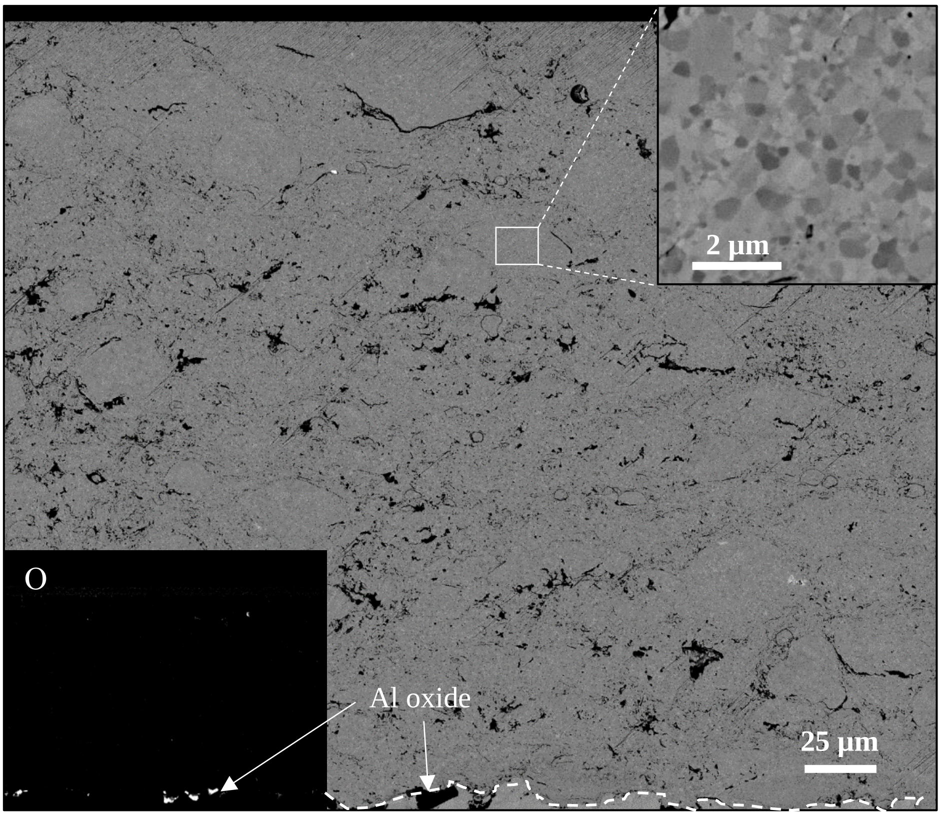

Figure 55: SEM image using BSE of a cross-section of a NiCrAlY-coated sample to 5% O_2 *+ 20%* H_2O *+* N_2 *at 600 °C for 168 hours. The signal for oxygen from the EDX analysis is located at the bottom left of the picture. A higher magnification of a section is shown at the top right. The dashed line represents the coating/substrate interface.*

The microstructures of the coatings were quite similar with some porosity. The NiCr coating exhibited larger pores, mostly distributed along the splat boundaries. NiAl and NiCrAlY displayed smaller pores evenly distributed within the coating. It is well known that porosity plays a major role in corrosion resistance, as pores act as fast pathways for corrosive species. The number of open or connected pores is an important parameter. It was assumed that a high number of closed pores would result in less severe corrosion than a large number of open pores, as the penetration of the corrosive species would be more tedious. The use of 3D tomography in future studies could unravel the connectivity of the pores after thermal spraying, as demonstrated in 9.1.2.

The grain sizes differed somewhat within the three coatings (Figure 52, Figure 54, and Figure 55). NiCr and NiAl exhibited grain sizes between 0.5 and 5 µm while NiCrAlY showed sizes between 0.2 and 1 µm. Smaller grains influence the diffusion of chromium and/or aluminum towards the surface of the coating and consequently the formation of chromia (Cr_2O_3) and alumina (Al_2O_3). Small grains imply more grain boundaries than large grains, resulting in a higher flux of species that could then form and feed a protective oxide, e.g. the flux of chromium to form a chromium-rich oxide.

A common problem with coating applications at high temperatures is the interdiffusion of alloying elements from the coating to the substrate [135]. This phenomenon not only leads to a depletion of elements that enhance the corrosion resistance of the coating (such as chromium and aluminum), but also to a decrease in mechanical strength at the interdiffusion zone [136]. This results in reduced pressure-bearing capabilities and spallation of the coating.

After exposures to both environments, all three coatings exhibited an interdiffusion area at the coating/substrate interface, see Figure 56.

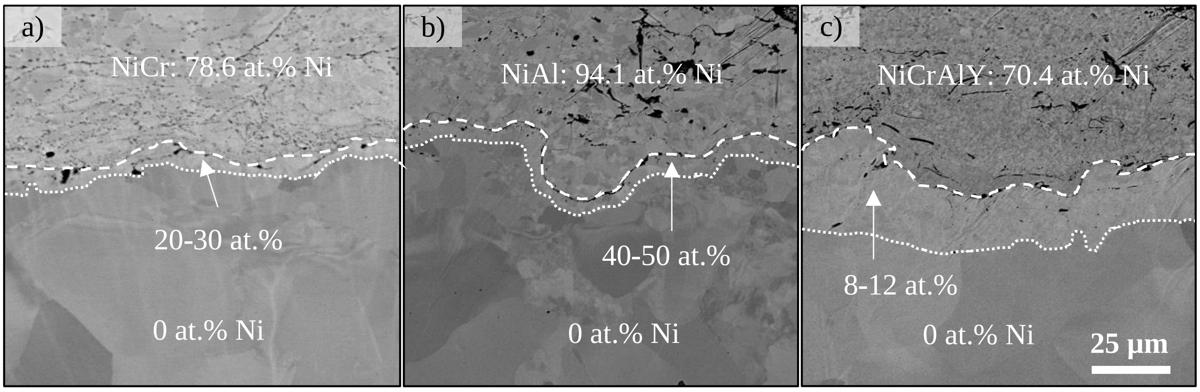

Figure 56: SEM images using BSE of cross-sections of a) NiCr coating, b) NiAl coating, and c) NiCrAlY coating at the coating/substrate interface, after an exposure to 5% O_2 + 20% H_2O + N_2 at 600 °C for 168 hours. The regions between the dashed lines are the austenitized areas.

The driving force for the diffusion of nickel was high as the substrate material 16Mo3 does not contain any. EDX point analysis revealed that the NiAl sample had the highest nickel content in the interdiffusion zone with 40-50 at.%, followed by the NiCr sample with 20-30 at.%, and the NiCrAlY sample with 8-12 at.%. Not only does the nickel content differ among the samples at this interdiffusion zone but also the depth. The NiCrAlY sample exhibited the deepest area compared to the two other coated samples.

Austenitization occurred due to the high nickel content in that zone. This could lead to mechanical issues caused by the higher coefficient of thermal expansion of the austenitic phase than the ferritic phase [137, 138]. Mechanical stresses would therefore be introduced during thermal cycling, which could cause spallation of the coating. The nickel content in the interdiffusion zone increased when the nickel content in the coating increased. This is due to the gradient of nickel between the coating and the substrate that induced the driving force for diffusion: the more nickel content in a coating, the stronger the driving force. However, no negative effects of the interdiffusion on the performance of the coatings were observed for 168-hour exposures. It is therefore necessary to investigate this aspect further with thermal cycling and/or longer exposure times.

Highly corrosive environment: 5% O_2 + 20 %H_2O + N_2 + 1.0 mg/cm^2 KCl

The corrosion behavior of the three coatings was also investigated when exposed to air at 600 °C with pre-deposited KCl for 168 hours [139]. The general behavior of the coatings in this environment was that they remained overall protective, however, the corrosion protection differed among the coatings. The NiCr coating formed an outward-growing oxide scale as well as an inward growing-oxide scale, reaching a depth of about 30 µm. For the NiCrAlY coating, a low corrosion attack was observed with only minor oxide formation. The NiAl coating exhibited good performance regarding corrosion resistance.

As water vapor and alkali chlorides are present simultaneously in flue gas during the combustion of biomass and waste [11, 140], it is relevant to include both of them in the simulated environment.

The mass gains of the coatings in the presence of KCl and water vapor are presented in Figure 51. The NiCr coating exhibited the highest mass gain with approximatively 2.4 mg/cm^2, corresponding to a thickness of 17 µm. The NiCrAlY coating showed a lower mass gain than the NiCr coating with roughly 0.38 mg/cm^2, which corresponds to an oxide thickness of about 3 µm. In contrast to the other two coatings, the NiAl coating displayed a mass loss that implies that the oxidation rate was lower than the evaporation rate of the deposited KCl. As a comparison, the mass gains of 304L varied between 0.9 and 2.5 mg/cm^2 (calculated from the oxide thickness).

The high mass gain of NiCr can be explained by the presence of a thick oxide of 30-50 µm on the surface of the coating, which can be seen as two different layers (Figure 57). The EDX analysis revealed that the outermost layer was composed of a nickel- and a chromium-containing oxide, with potassium chromate (K_2CrO_4). The oxide layer beneath the outermost layer was composed of a porous chromium oxide. This oxide layer was outward-growing, marked by a straight horizontal line at its base. Below this line, an inward-growing layer with a maximum thickness of about 15 µm was observed. It grew along the splat boundaries and was composed of nickel and chromium oxide. The presence of voids was also observed due to the separation of splats, resulting in wider inter-splat boundaries. This feature was observable up to a depth of 75 µm. Chromium chlorides were detected deeper down in the coating, at the splat boundaries (EDX map in Figure 57). Hence, chlorine had diffused through the coating towards the coating/substrate interface where metal chlorides had also formed within the substrate (Figure 58).

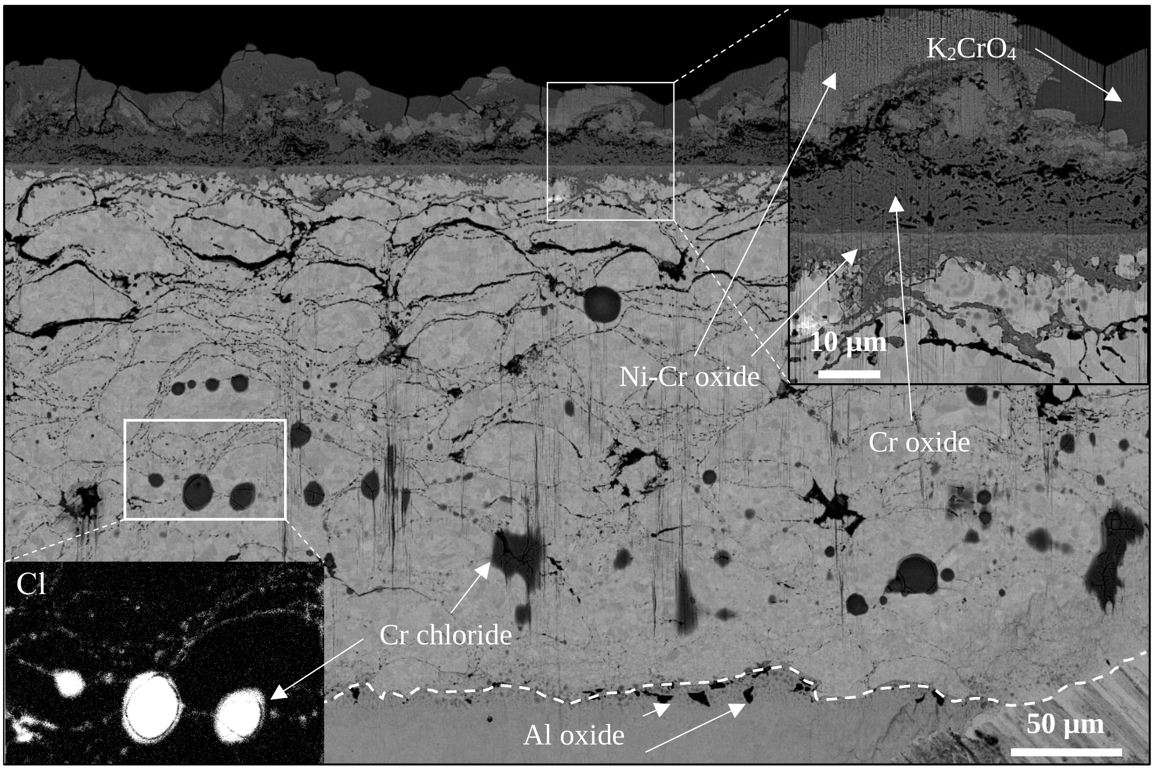

Figure 57: SEM image using BSE of a cross-section of a NiCr-coated sample after exposure to 5% O_2 *+ 20%* H_2O *+* N_2 *+ 1.0 mg/cm*^{2} *at 600 °C for 168 hours. The signal for chlorine from the EDX analysis is located at the bottom left of the picture. A higher magnification of the thick oxide layer is shown at the top right. The dashed line represents the coating/substrate interface.*

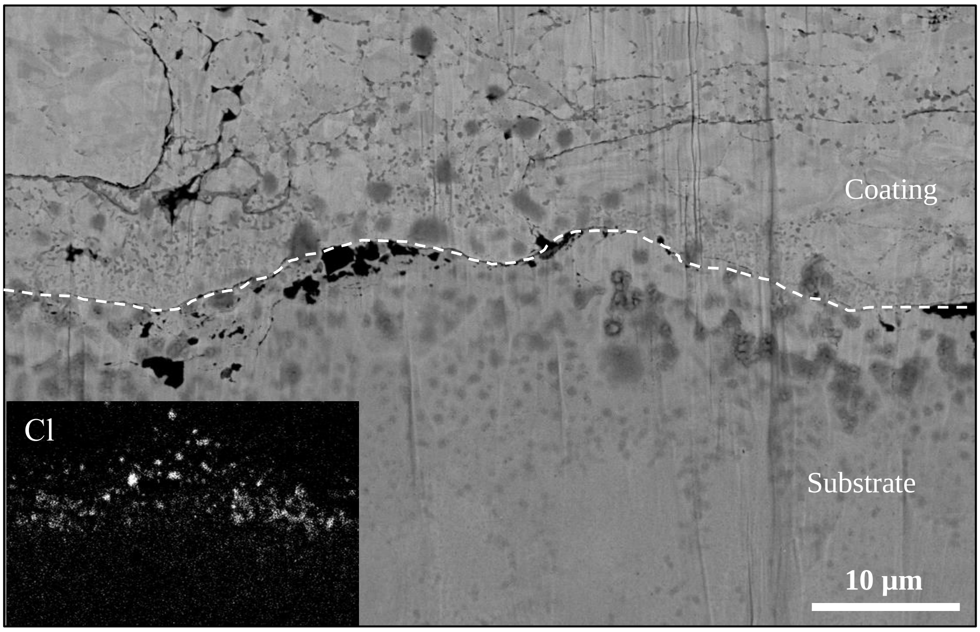

Figure 58: SEM image using BSE of a cross-section of the coating/substrate interface of a NiCr-coated sample after exposure to 5% O_2 *+ 20%* H_2O *+* N_2 *+ 1.0 mg/cm²* *at 600 °C for 168 hours. The signal for chlorine from the EDX analysis is located at the bottom left of the picture. The dashed line represents the coating/substrate interface.*

The NiAl coating exhibited the lowest corrosion attack and did not form any thick oxide on the surface but a non-continuous aluminum oxide of 5 µm thickness, see Figure 59. No oxide formation nor chlorides were detected within the coating. This means that the aluminum oxide formed on top prevented species (e.g. chlorine) from penetrating the coating. Compared to the NiCr coating, no breakdown of the oxide scale on the surface was observed, i.e. the primary protection remained present in the NiAl coating. This is explained by KCl only reacting with a chromium-rich oxide and not an aluminum-rich oxide. However, the most protective form of aluminum oxide is α-Al_2O_3, which was not considered in this study because the exposure temperature would have been too low for the formation of α-Al_2O_3. It was, therefore, assumed that a transient form of alumina γ-Al_2O_3 had formed. It has been shown that this transient form exhibits less corrosion resistance in the presence of KCl [141], however, in the present study, it exhibited a sufficiently protective behavior that prevented chlorine penetration.

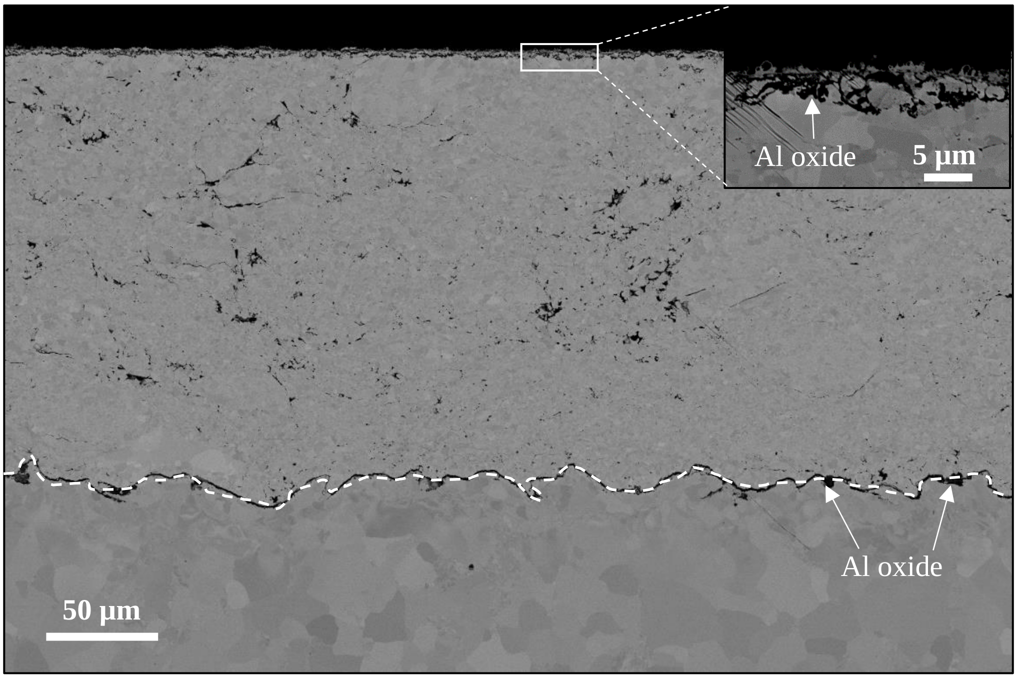

Figure 59: SEM image using BSE of a cross-section of a NiAl-coated sample after exposure to 5% O_2 + 20% H_2O + N_2 + 1.0 mg/cm^2 at 600 °C for 168 hours. The dashed line represents the coating/substrate interface.

The overall corrosion resistance of NiCrAlY was much better than for NiCr but lower than for NiAl. This is probably due to the presence of chromium in the coating; the chromium reacted with KCl to form K_2CrO_4 particles on the surface (Figure 60). An enrichment of chromium at the splat boundaries just beneath these particles was observed (EDX map in Figure 60). This was probably caused by the diffusion of chromium towards the surface, as this element was depleted due to the reaction with KCl. Despite the formation of potassium chromate, no thick oxide scale was formed on the surface of the coating. Furthermore, no sign of oxide formation nor chlorine penetration was observed within the coating. Consequently, the thin oxide formed on the on the surface of the coating remained protective, preventing the intrusion and diffusion of corrosive species. Therefore, the NiCrAlY coating managed to protect the substrate from a corrosion attack. However, it is unknown how the performance of the coating would be affected by further depletion of chromium with longer exposure durations and larger amounts of KCl.

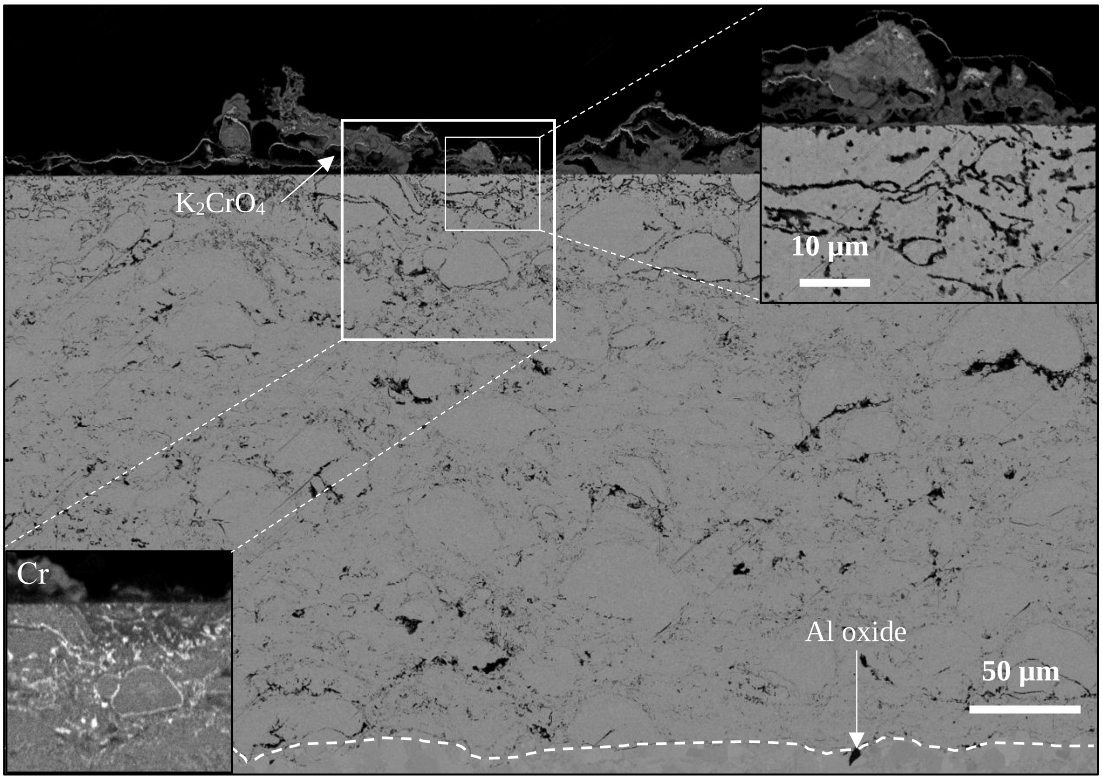

Figure 60: SEM image using BSE of a cross-section of a NiCrAlY-coated sample after exposure to 5% O_2 *+ 20%* H_2O *+* N_2 *+ 1.0 mg/cm*^{2} *at 600 °C for 168 hours. The signal for chromium from the EDX analysis is located at the bottom left of the picture. A higher magnification of the surface is shown at the top right. The dashed line represents the coating/substrate interface.*

Porosity of coatings using different thermal spraying techniques

Porosity has always been a weakness for coatings. Pores must be kept to a minimum in order to obtain good performance of the final product. Other than HVAF, the thermal spraying techniques flame spraying, plasma spraying, and HVOF have been analyzed as-sprayed [142]. It was found that the three techniques exhibited a lot of porosity compared to HVAF. However, it was also found that the spraying parameters of the HVOF technique could be optimized to obtain a denser coating. T. Hussain et al. have characterized the microstructures of HVOF-sprayed coatings of different compositions and found not only a large spread in porosity but also that the composition of the powders used had an impact on the final microstructure of the coating [143]. A previous study has compared the microstructure of as-sprayed HVOF and HVAF coatings with the same composition [144]. It was shown that the HVAF-sprayed coatings exhibited less porosity than the HVOF-sprayed coatings. Consequently, this novel HVAF technique seems to have the potential to produce better corrosion protection.

The HVAF-sprayed coatings used in this thesis seemed to show more porosity than some HVOF- and plasma-sprayed coatings used in previous studies [142, 143, 145]. The reason behind this observation is suggested to be as follows: mechanical polishing was not used in the present study to prepare the cross-sections of the coatings, instead, BIB milling was used, which resulted in very smooth surfaces. The difference between mechanical polishing [146] and BIB milling is shown in Figure 61. It can be seen that more porosity appears when BIB milling is used, as no potential plastic deformations caused by mechanical polishing occurs, which probably makes the pores less visible. It is, consequently, difficult to directly compare the microstructure of the coatings prepared in these two different ways. However, regardless of cross-sectional technique, the observation underlines that the spraying parameters must be optimized in order to reduce porosity.

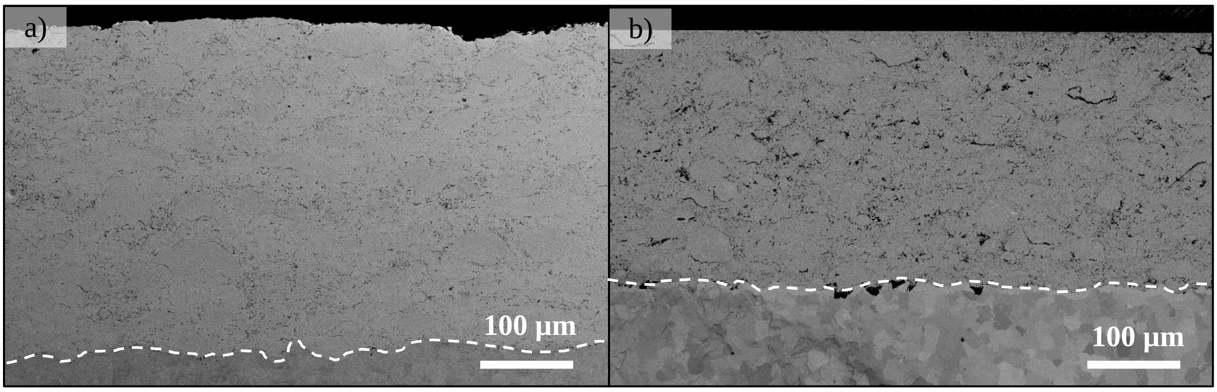

Figure 61: SEM image using BSE of the cross-section of the NiCrAlY coated sample after a) mechanical polishing and after b) broad ion milling (BIB). The dashed line indicates the coating/substrate interface.

9.2.2. Mitigation of high-temperature corrosion by altering the environment

Field exposures are as important as laboratory exposures the combination of both is required in order to fully understand the corrosion phenomena that occur in boilers and, subsequently, find adequate corrosion mitigation solutions. Field exposures are relevant as the materials tested are surrounded by real environmental conditions, which are more complex and in some cases more corrosive than the simulated environment in a laboratory.

Two types of tests are usually conducted in boilers to investigate corrosion:

- A deposit test: samples are exposed inside the boiler at the area of interest to collect ashes or deposits that are to be characterized.
- A corrosion test: the samples are exposed inside the boiler in order to generate new knowledge about the corrosion behavior of the materials.

Two field investigations were conducted in this thesis in order to reduce the high-temperature corrosion experienced by the tested materials by making the surrounding environment less corrosive. The results were assessed with the two types of tests described previously.

- First field investigation: Steamboost superheater [118]

The aim of this field investigation was to experimentally evaluate the corrosiveness of a new location for superheaters. This location was unraveled via CFD calculations, which indicated a potentially milder environment for superheaters. A summary of the research strategy of this field investigation is described in 8.2.2.

Deposit tests

The deposits tests were performed in order to evaluate the influence of several operating settings of the boiler on the chemical composition of the deposit at the new possible superheater position. 29 settings were tested by inserting probes inside the boiler for 2 hours to collect ashes/deposits. After each different setting, the samples were removed for characterization, and photographs were taken for optical inspection. Ion Chromatography (IC) was performed in order to quantify the amount of corrosive species present within the deposits, and SEM/EDX was used on selected deposits in cross-sections.

It is well known that the amount of deposits and their relative contents of chlorine and alkali compounds are relevant factors to consider when dealing with the high-temperature corrosion of superheaters and, more specifically, stainless steels. Therefore, the analysis focused on the evaluation of these parameters when investigating the deposits.

Figure 62 shows the chlorine content in the deposits. The concentration of chlorine varied between 3.5 at% for the setting with the least amount, and 20.9 at% for the setting with the highest amount. Figure 63 shows the amount of deposits collected for each setting. It is important to consider that the amount of chlorine is not correlated to the amount of deposits. One of the settings marked in red (Figure 62 and Figure 63) was chosen for the corrosion probe test. This setting shows a small amount of chlorine with very few deposits. The distribution of chlorine within the deposits was analyzed with SEM paired with EDX.

The deposit analysis showed that the composition of the deposit was sensitive to the boiler’s settings. Natural variations in flue gas temperature and composition/deposit formation occurred due to the variations in combustion and fuel. However, the large variations observed herein regarding the amount of deposits accumulated on the samples, and the amount of chlorine present within the deposits, show that the operating settings of a boiler have an impact on the corrosiveness of the deposits at the new possible superheater position. This implies that it is possible to vary the amount of deposits and the amount of chlorine present in the deposits by changing the way of operating a boiler.

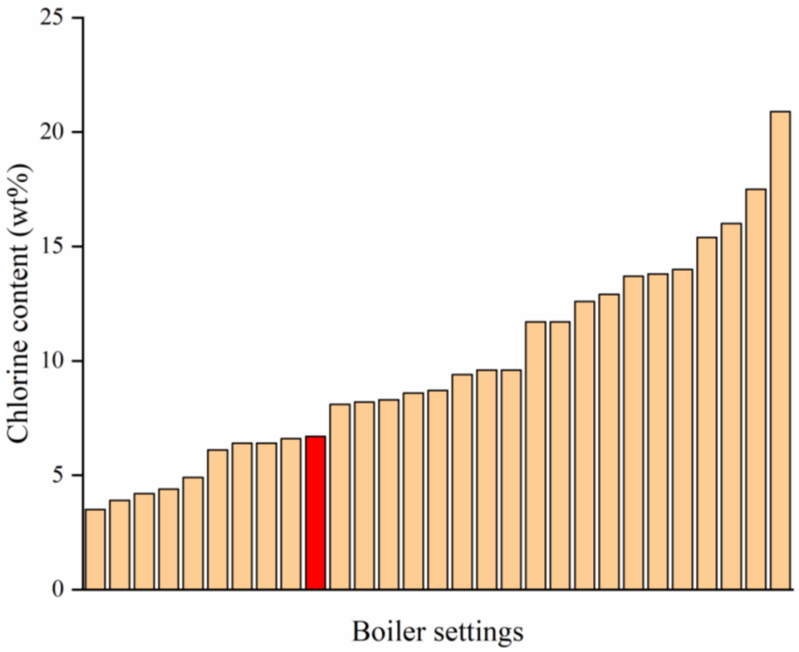

Figure 62: Chlorine content (wt%) in the deposits accumulated on an air-cooled probe at the Steamboost position for the 29 different boiler settings during 2 hours. The red bar represents the boiler settings leading to small amount of chlorine and very few deposits.

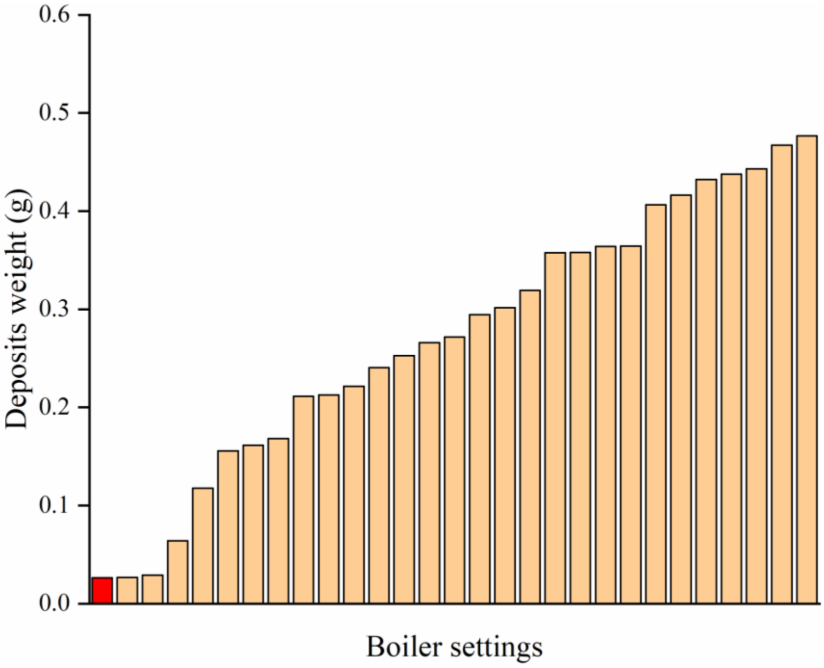

Figure 63: Amount of deposits accumulated on the air-cooled probe for the 29 different settings during 2 hours. The red bar represents the boiler settings leading to small amount of chlorine and very few deposits.

Corrosion tests

Corrosion tests were performed using corrosion probe exposure and a fixed installation that consisted of three loops connected to the main steam of the plant and carrying several different superheater tubes welded together. Only material from the system of loops was investigated in this thesis. The inlet temperature of the steam was 340 °C at the entrance to the first superheater loop and 470 °C at the outlet, resulting in a metal temperature of approximatively 525 °C. The fixed installation was exposed for 8000 hours.

The material loss of the samples was analyzed using ultrasound measurements in order to quantify the corrosion tests of the fixed installed materials. The thickness was measured at eight points on each sample along the ring using an Olympus 27MG ultrasonic thickness gage with a 0.01 mm resolution.

The present study focused on the fixed installed material 347H. The material loss is presented in Figure 64. The steam entered the inlet of the first loop at 340 °C and left the fixed installation via the outlet of the third loop at 470 °C. The material temperatures were estimated to be 395 °C at the inlet of the first loop and 525 °C at the outlet of the third loop. The material loss of the samples increased when the temperature increased (from loop 1 to loop 3).

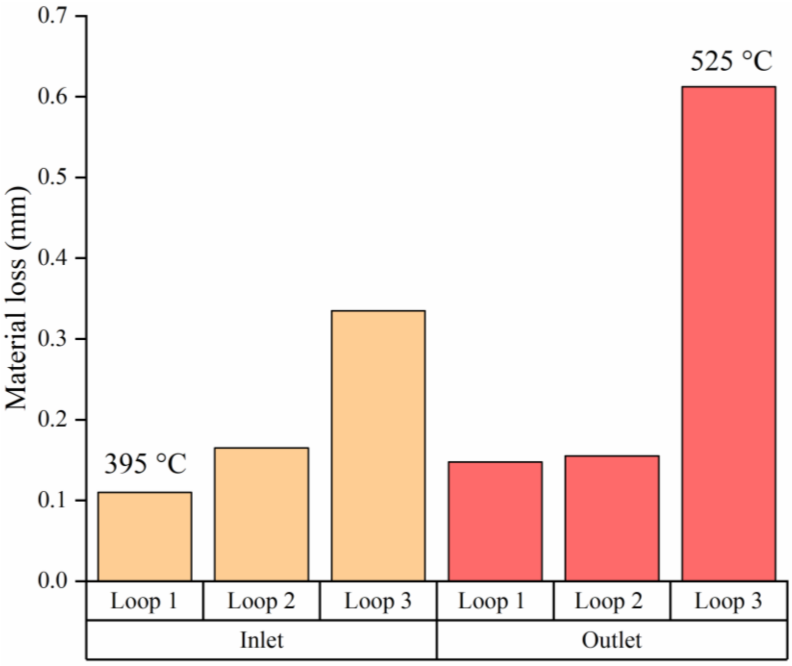

Figure 64: Material loss of 347H samples exposed at six different locations during 8000 hours at 600 °C.

The 347H sample exposed at the highest material temperature was analyzed in detail with microscopy investigation. The sample was exposed at the outlet of the third loop with a material temperature of approximatively 525 °C. Very small amounts of deposits were found on the sample as the boiler was cleaned before removing the sample. Figure 65 shows a SEM image acquired with the BSE of a representative area. A thick oxide scale of about 250 µm, consisting of a complex layered scale was observed. The EDX analysis shown in Figure 66 reveals that the outer parts were made of fully oxidized

Fe-Cr scale with some areas/alloy grains in the middle that were not oxidized. Grain boundary attacks could be seen at the scale/substrate interface, where nickel enrichment seemed to occur in the alloy. The steel grain boundary attack is in good agreement with the features observed in lab-scale exposures using continuous deposition of KCl(s) on 304L (see 9.1.1 and 9.1.2).

Indications of alkali chromates were confirmed with EDX point analysis. Low chlorine concentrations were also detected in the corrosion products. The overall observation is that the 347H sample reached breakaway oxidation, which is in good agreement with the material loss measurements. As described in Section 6.2, the chromium from the protective layer (primary protection) may react with the alkali compounds to form alkali chromates, thus depleting the protective layer of chromium. This leads to a fast-growing iron oxide (secondary protection).

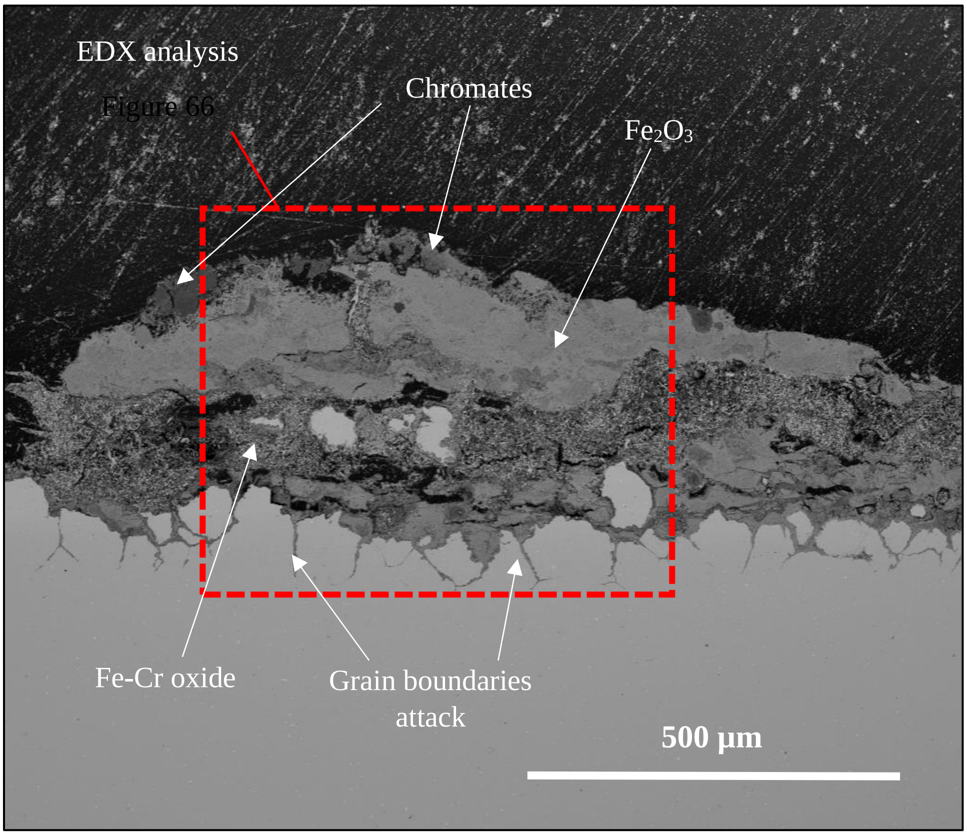

Figure 65: SEM image using BSE of 347H material exposed at the outlet of loop 3 in the Steamboost position during 8000 hours.

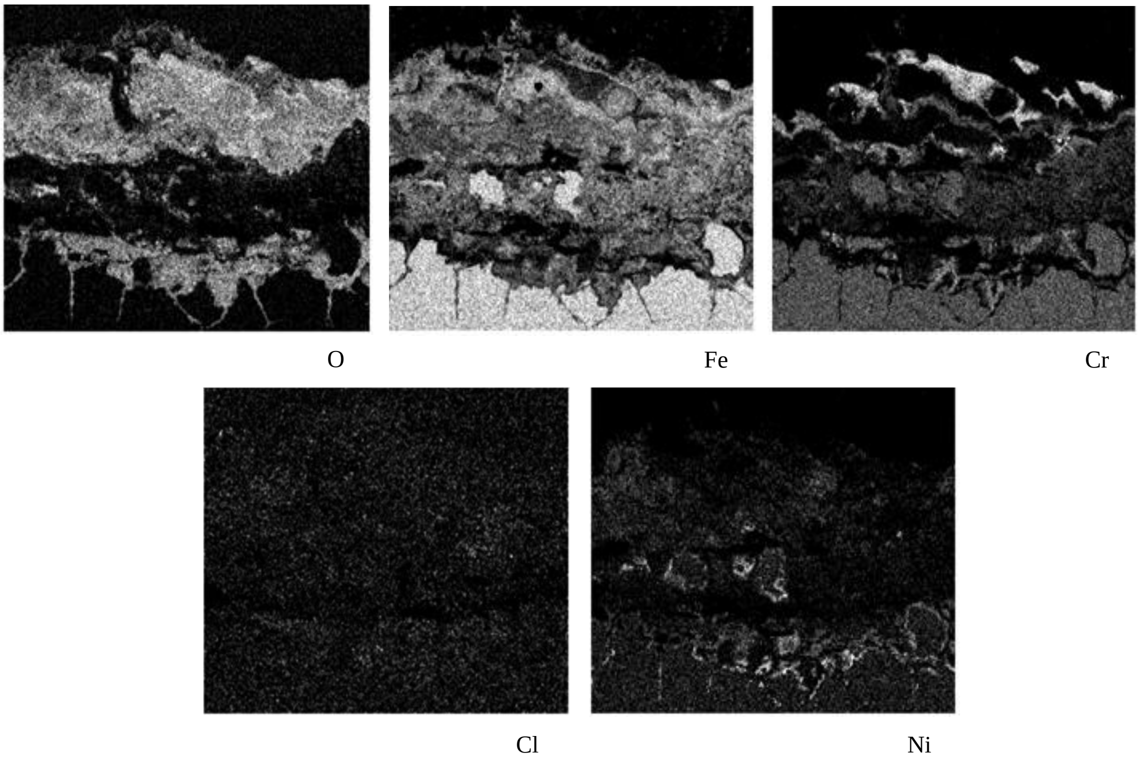

Figure 66:EDX analysis of the marked area in Figure 65.

- Second investigation: Sulfur recirculation and corrosion memory

The aim of this field investigation was to study the corrosion memory effect using two different lines/boilers: one considered corrosive as a reference and one considered less corrosive due to a milder environment induced by the Sulfur Recirculation technique. Changing samples from one line to another one halfway through an exposure would give insights into this corrosion memory effect.
A summary of the research strategy of this field investigation is described in 8.2.2.

Deposit tests

The deposit tests were performed in order to observe the influence of Sulfur Recirculation and corrosion memory on the chemical composition of the deposit at the superheater position. Deposits were removed from the air-cooled probes after the 2000-hour exposures, see example in Figure 67.

Figure 67: Air-cooled probe exposed 1000 h in the Sulfur Recirculation line (first) and 1000 h in the reference line (after).

The amounts of chlorine and sulfur were determined using Ion Chromatography (IC) and are presented as mass percentage (amount of ions/100 g deposits). Figure 68 shows the percentage of chlorine measured in the deposits of the reference and corrosion memory probes. After the 2000-hour exposure, it was observed that the amount of chlorine was drastically lower (0.1%) in the Sulfur Recirculation line (Rec) than the reference line (2.65% for Ref). This can be interpreted as a 97% reduction of chlorine content in the deposits.

Regarding the corrosion memory probes which were exposed 1000 h in each line/environment, the dense and hard deposits made the selection of a representative part of the deposits complicated. It was therefore only possible to analyze the outer part of the deposits. The first corrosion memory probe is represented as RecRef where the samples were first exposed 1000 hours to the reference line and then 1000 hours to the Sulfur Recirculation line. By comparing with the results of the reference exposures, it can be concluded that the RefRec sample has similar amount of chlorine as the deposit on the sulfur recirculation sample (Rec). A similar trend may be observed for the RecRef sample which shows a chlorine content in line with the Reference sample deposit (Ref). This indicates that only the outer part of the deposit was possible to analyse, corresponding this deposit to the last 1000 hours of exposure.

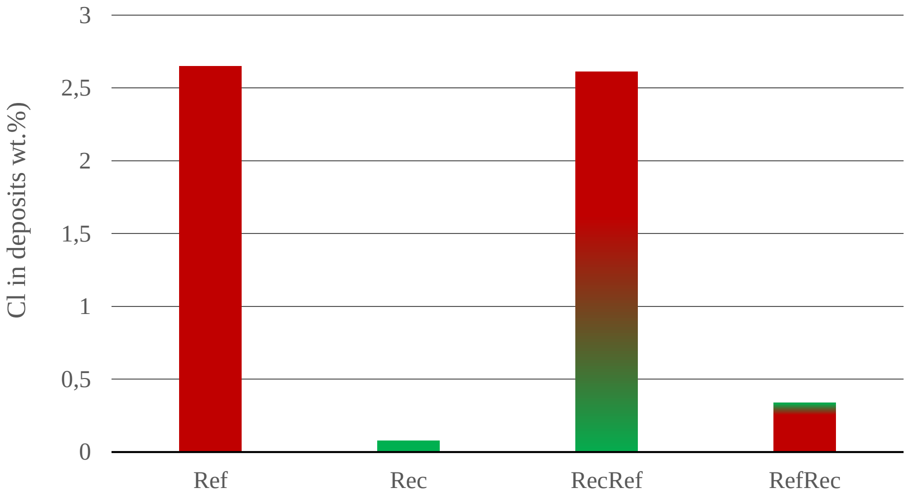

Figure 68: Chlorine content (wt.%) in the deposits accumulated on the Rec, Ref, RecRef and RefRec probes.

Figure 69 shows the percentage of sulfate in the deposit for the different exposures. After 2000 hours exposure, the amount of sulfur in the Sulfur Recirculation line is approximately 13% and approximately 9% in the reference line as expected. As mentioned above, the hard deposits made it very difficult to take a homogeneous deposit sample for these probes and no significant difference can be found between the RefRec probe, which presents an 8% sulfate, and the RecRef probe with a 9% sulfate. By comparing with the reference exposures, it can be seen that only the Rec probe, exposed 2000 hours in the sulfur recirculation line, presents a higher amount of sulfate.

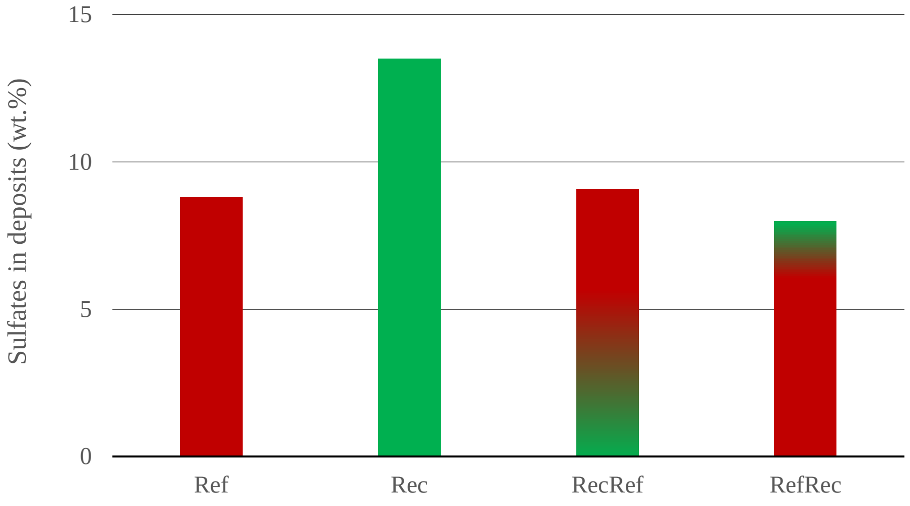

Figure 69: Sulfur content (wt.%) in the deposits accumulated on the Rec, Ref, RecRef, and RefRec probe.

Corrosion tests

Corrosion tests were performed using rings attached to a corrosion probe (similar to the probe used in the deposit tests of the first field investigation). Material loss was used as a criterion for the assessment of corrosion performance. Several materials were tested at two different temperatures, 450 and 525 °C. However, only the 525 °C temperature and the material 347H are included in the present work.

The material loss measurements were performed by measuring the thickness of the ring at 8 different locations using SEM images. The results are shown in Figure 70. The flue gas direction is indicated with a red arrow. All materials for all conditions of exposure tend to display a higher material loss on the side exposed to the flue gas. The clear beneficial effect of sulfur addition can be seen when comparing the material loss between the two probes Rec and Ref. Nearly no material loss was observed for Rec while Ref exhibited a material loss of approximatively 0.3 mm on the flue gas side. The corrosion memory probe RecRef exhibited a higher material loss than Rec but a lower one than Ref. Exposing 347H to the Sulfur Recirculation line first seems to have had a beneficial effect on the future corrosion performance of the material. The second corrosion memory probe RefRec displayed material loss similar to the Ref probe.

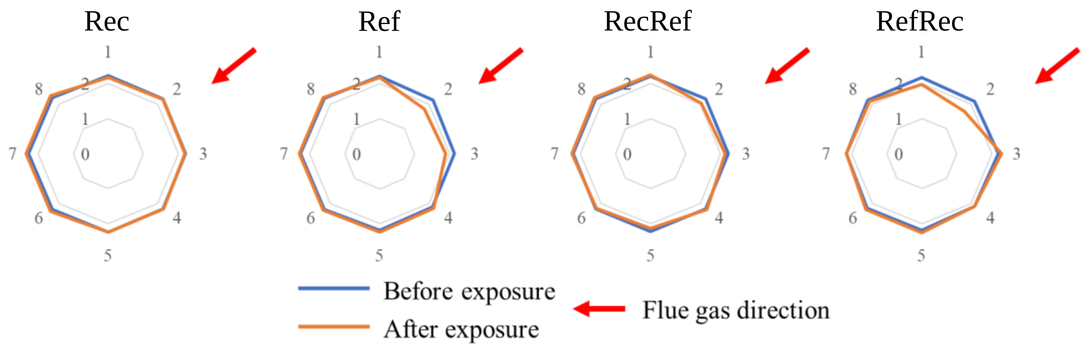

Figure 70: Material loss (mm) of 347H at 525 °C during 2000 hours under four different experimental conditions.

For a better visualization of the results, Figure 71 shows the maximum material loss linearly calculated in mm/year for the four different conditions studied. Studies have previously shown that the material loss experienced by probe samples is usually higher than the material loss measured directly on the superheater tubes [147, 148]. Waste-fired boilers operating within similar temperature ranges and using industrial waste as fuel can induce a material loss up to 16 mm/year in 304L-type steel probe samples [149]. The samples exposed to the reference line (Ref) exhibited a material loss of 1.8 mm/year. This indicates that the reference line contains a mild/medium corrosive environment. The samples exposed to the Sulfur Recirculation line exhibited a material loss of 0.2 mm/year. This implies a decrease of 89% in material loss when sulfur addition is incorporated into the boiler. Such a material loss is very low considering that biomass-fired boilers can exhibit a material loss of 1 mm/year with the same materials investigated using a probe [147, 148]. In addition, other sulfur addition techniques can lead to a material loss up to 6 mm/year when the boiler is operated around 600 °C [150]. Based on these observations and comparisons, it can be stated that the environment inside the Sulfur Recirculation line is very mild.

The two different lines gives a good possibility to investigate the corrosion memory effect. In order to estimate the combined expected corrosion rate in the mixed exposures, the corrosion rate needs to be estimated based on the ref/rec 2000 hours exposures. A linear growth rate extrapolated from the different environments would give a predicted material loss of 1,8/2 + 0,2/2 = 1,0 mm/year, i.e. the results (0,7 mm/year) indicate a positive corrosion memory effect of the initial sulfur rich environment/deposit

The samples attached to the first corrosion memory probe (RecRef) were exposed to the Sulfur Recirculation line for the first 1000 hours and to the reference line for the last 1000 hours. They exhibited a material loss of 0.7 mm/year which implies a 60% decrease in material loss compared to the samples exposed to the reference line only (Ref). It exhibited also a lower value than the calculated mixed exposure (1 mm/year). This result suggests a positive corrosion memory effect by exposing the materials to a sulfur-rich environment first.

The samples attached to the second corrosion memory probe (RefRec) were exposed to the reference line for the first 1000 hours and to the Sulfur Recirculation line for the last 1000 hours. They exhibited a material loss of 1.9 mm/year (to be compared with the calculated 1 mm/year). This value is also in the same range as the samples exposed only in the reference line for the same amount of time. This result indicates a very strong negative corrosion memory effect when the samples are exposed first in the most corrosive environment. Thus, both the mixed exposures indicate a corrosion memory effect.

These observations agree well with a chlorine-induced accelerated corrosion. The Rec sample exhibited very little material loss compared to the Ref sample. This was also associated with a low chlorine content found in the deposits of the Rec sample due to sulfation of the alkali chlorides. It has been demonstrated that the presence of chlorine generally increases the severity of the corrosion attack. Several mechanisms have been suggested to cause the accelerated corrosion e.g. the active oxidation [13, 16, 60-65] or electrochemical mechanism [61, 74, 75]. However, the results (see below) indicate the presence of reactive alkali and a breakaway corrosion in all environments even if the Rec sample resulted in a mild corrosion attack.

The corrosion memory sample RecRef was first exposed in the line with Sulfur Recirculation, building the first layers of deposits with a low chlorine content due to the mild environment. After being changed to the reference line (after 1000 hours), the deposits from the harsher environment began to stack on top of the previous deposits. Compared to the calculated mean value of material loss expected after 1000 hours in each line, the RecRef sample exhibited a lower material loss. This could be explained by the first hard layers of deposits with low chlorine content, which could mitigate the aggressive deposit buildups generated in the reference line. The deposits containing a higher amount of chlorine would then remain on the outer part of all the deposits, making the path towards the material more intricate for corrosive species, i.e. chlorine. This agrees well with the chlorine content value (2.6 wt.%) of the RecRef sample where only deposits from the outer part were analyzed, showing the high accumulation of chlorine in the outer part.

Reversely, the RefRec sample exhibited a higher material loss than the calculated mean value. This could be explained by the first buildup of deposits with high chlorine content from the harsh environment. Due to the hard deposits, even after placing the sample in a milder environment (Sulfur Recirculation), the corrosive species, i.e. chlorine could remain active in the accelerated corrosion without being neutralized (e.g. via sulfation). Thus, the aggressiveness of the first layers of deposits building on a sample could dictate its future corrosion resistance.

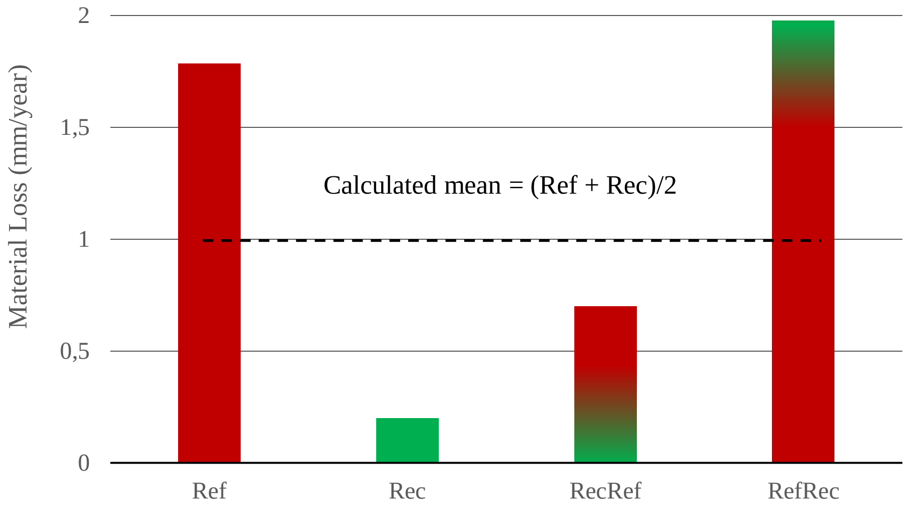

Figure 71: Material loss (mm/year) of the samples exposed under four different experimental conditions. The dashed line represents the calculated mean value of the RecRef and RefRec exposures (~1 mm/year).

This field investigation clearly shows the influence of the full-scale Sulfur Recirculation technique on deposit chemistry. Deposits of lower corrosiveness accumulate on the materials, resulting in an overall milder corrosion attack.

The corrosion memory tests show that exposing the materials first to a less corrosive environment (fewer corrosive deposits) may mitigate the corrosion that could occur when the materials are exposed to a more corrosive environment afterwards.

10. Conclusions and Summary

10.1. Laboratory investigations of corrosion mechanisms

High-temperature exposures of commercial alloys with increasing nickel content: a comparative study

The aim of this study was to investigate the corrosion behavior of four commercial alloys with increasing nickel content in a harsh KCl-rich environment: T91/P91 (0 wt.% Ni), 304L (10 wt.% Ni) Sanicro 28 (30 wt.% Ni) and Inconel 625 (62 wt.% Ni).

Considering the general corrosion, increasing the amount of alloying elements in an alloy, e.g. nickel or chromium, resulted in a drastic decrease of the total oxide thickness, from ~23 µm for T91/P91 to ~ 500 nm for Inconel 625.

More precisely, increasing the amount of nickel (e.g. from Sanicro 28 to Inconel 625) in an alloy can decrease the corrosion rate of the general corrosion (i.e. decreasing the total oxide thickness).

Considering the steel grain boundary attack, it was first observed that the absence of nickel in T91/P91 resulted in mild grain boundary attacks represented by the formation of chromium-rich oxide at the grain boundaries. For the stainless steels containing nickel (304L and Sanicro 28) and the nickel-based alloy (Inconel 625), the depth and morphology of the grain boundary attack changed compared to T91/P91:

- 304L and Sanicro 28 exhibited grain boundary attacks characterized by internal oxidation and porosity.
- Inconel 625 exhibited grain boundary attacks characterized primarily by void formation and the development of large cavities.

Even if the introduction of nickel in an alloy resulted in more severe grain boundary attacks, it seems that increasing the nickel content would decrease the depth of the attacks. These observations indicate that increasing the amount of nickel in an alloy can decrease the extent of grain boundary attacks and can also change their morphology.

It is important to consider that the study was focused only on commercial alloys used in biomass- and waste-fired boilers. However, their chemical composition also differs regarding e.g. other elements and crystal structure. Thus, the role of nickel in the secondary regime is suggested to be investigated with model alloys where better control can be achieved of other parameters.

In-depth investigation of grain boundary attack on a 304L-type alloy

The aim of this study was to provide a detailed representation and new insights regarding intergranular corrosion in stainless steels by using a FIB/SEM to perform 3D reconstruction/tomography of grain boundary attacks linked to a TEM investigation.

The key findings of this study are summarized as follows:

- The combination of the 3D-FIB/TEM offers a great potential for the study of complex features, i.e. intergranular corrosion. The 3D tomography provides information beyond the traditional two-dimensional analyses allowing a better interpretation of the features observed, while the TEM complements with high magnification imaging and high-resolution chemical analysis. The implementation of the 3D EDX-FIB technique in future work would also enhance the depth of such study by providing three-dimensional chemical information.

- The initiation (1-hour exposure) and growth (24-hour exposure) of the grain boundary attack occurred very rapid below an intact secondary protection.

- No large accumulations of metal chlorides were observed at the grain boundary regions. Instead, indications of very rapid diffusion (large depletion zones) and a microstructure indicating fast diffusion were observed.

Influence of microstructure and environment on the KCl-induced corrosion attack

The aim of this study was to investigate the influence of α-Cr precipitates on the KCl-induced corrosion attack. Two heat treatments (solution-treated and heat-treated) were performed to generate different amounts of α-Cr in a nickel-based alloy (Ni35Cr4Nb). Within the scope of the collaboration between DTU and CTH, the study was focused on the comparison between the two methods of applying salt onto samples (pre-deposited slurry onto samples vs continuous condensation onto samples) regarding the KCl-induced attack, i.e. a possible combined effect of changes in microstructure and environment.

The results showed that the difference in simulating a corrosive environment resulted in a variation of the internal attack of the two different microstructures (generated by the heat treatments). The results are summarized as follows:

- KCl-induced corrosion by continuous deposition of KCl resulted in chromium depletion and void formation in the solution-treated sample while the pre-deposited KCl method led to chromium depletion only.

- KCl-induced corrosion by continuous deposition of KCl resulted in selective attack on the α-Cr precipitates in the heat-treated sample while the pre-deposited KCl method led to the selective attack and phase dissolution of the α-Cr precipitates.

10.2. Approaches to mitigate high-temperature corrosion

Mitigation of corrosion by improving materials: the use of coatings

The aim of this study was to evaluate the performance of three different nickel-based coatings HVAF-sprayed on a low-alloyed steel when exposed to two different environments.

Regardless of the type of environment, several features were found:

- The three coatings showed good adhesion to the substrate without any signs of spallation.
- A region of interdiffusion was observed at the coating/substrate interface, where nickel diffused from the coating towards the substrate, leading to austenitization of the area. A higher nickel content in a coating resulted in a higher content of nickel in the interdiffusion region.

In the mildly corrosive environment (5% O_2 + 20%H_2O + N_2 at 600 °C), all three coatings formed a thin protective oxide on top. However, the NiCr sample showed signs of oxide formation within the coating.

In the highly corrosive environment (5% O_2 + 20%H_2O + N_2 + 1.0 mg/cm^2 KCl at 600 °C), the level of corrosion attack differed among the coatings:

- The NiCr sample exhibited a high level of corrosion attack, resulting in the formation of a thick oxide on top of the coating together with chlorine penetration that reached the coating/substrate interface.
- The NiAl and NiCrAlY samples showed signs of good corrosion resistance with no chlorine penetration.

Future research on the three coatings should investigate of the coating/substrate adhesion by performing thermal cycling tests, as the interdiffusion zone could cause issues attributable to mechanical stresses. Longer exposures to a harsh environment must also be performed to study the influence of the depletion of chromium from a coating on its performance.

Mitigation of corrosion by altering the environment

- Steamboost superheater

The purpose of this study was to investigate the corrosiveness of a potentially new position for superheaters in a boiler. This concept has been labelled “Steamboost”. Previous CFD calculations indicated that this position should exhibit a milder environment [107], for this reason, deposit tests and corrosion tests were conducted.

- The deposit investigation showed that it is possible to influence both the amount as well as the corrosiveness of the deposit formed at the new superheater position over the grid, by optimizing boiler settings.
- The corrosion investigation showed that at the highest temperature of the fixed installation, the 347H stainless steel loses its protectiveness and enters the breakaway regime. The morphology of the grain boundaries attacks is in good agreement with the lab-scale exposure using continuous deposition of KCl(s).

Overall, the data acquired during the field exposures linked to CFD calculations indicate a new potential position for superheaters. However, the variations in fuel during combustion coupled with the complex processes that occur over the grid make the study more complex. Therefore, future work regarding the Steamboost position is need in order to understand the influence of the position on corrosion mechanisms.

- Sulfur recirculation and corrosion memory

This study aimed at investigating the corrosion memory effect by using two different boilers: one operating normally and used as a reference, and one implemented with the Sulfur Recirculation technique. The same materials were exposed to four different environments: Ref (reference line during 2000 hours), Rec (Sulfur Recirculation line during 2000 hours), RecRef (corrosion memory: exposed first to Rec during 1000 h and then to Ref during 1000 h), RefRec (corrosion memory: exposed first to Ref during 1000 h and then Rec during 1000 h).

The results showed that it is possible to mitigate the material degradation by exposing the material to a mild environment first (RecRef). However, the results also showed that mitigation of the material degradation due to a mild environment may not occur if the material has been exposed to a corrosive environment first (RefRec).

This shows the importance of the corrosion history of a material on its future corrosion resistance.

References

1. *NASA - Global Climate Change*. Available from: https://climate.nasa.gov/.
2. Arnell, N.W., S. Brown, S.N. Gosling, P. Gottschalk, J. Hinkel, C. Huntingford, B. Lloyd-Hughes, J.A. Lowe, R.J. Nicholls, T.J. Osborn, T.M. Osborne, G.A. Rose, P. Smith, T.R. Wheeler and P. Zelazowski, *The impacts of climate change across the globe: A multi-sectoral assessment.* Climatic Change, 2016. **134**(3): p. 457-474.
3. *Paris Agreement - COP 21*. Available from: https://ec.europa.eu/clima/policies/international/negotiations/paris_en.
4. *IEA - Policies database*. Available from: https://www.iea.org/policies?sector=Multi-sector&page=1&year=asc.
5. Frandsen, F.J., *Impacts of Fuel Quality on Power Production and the Environment.* Energy & Fuels, 2013. **27**(10): p. 5593-5594.
6. Frandsen, F.J., S. Fendt and H. Spliethoff. *Fuel Quality Impact in a Historical Perspective: A Review of 25 Years of EU-Funded Research on Fuel Characterization, Ash and Deposit Formation, and Corrosion*. in *Fuel Quality Impact Conference 2016*. 2016.
7. Frandsen, F.J. *Quantification of Release of Critical Elements, Formation of Fly Ash and Aerosols: Status on Current Understanding and Research Needs*. in *11th European Conference on Industrial Furnaces and Boilers (INFUB11)*. 2017. Elsevier.
8. Frandsen, F.J., *Next Generation of High-Efficient Waste Incinerators.* 2010.
9. Karlsson, S., L.-E. Åmand and J. Pettersson. *Reducing high temperature corrosion when burning waste by adding digested sewage sludge*. in *Swedish-Finnish Flame Days, January 26-27 2011 in Piteå, Sweden, The Swedish and Finnish National Committees of the International Flame Research Foundation (IFRF) and The Scandinavian-Nordic Section of the Combustion Institute (SNCI)*. 2011.
10. Kassman, H., L. Bäfver and L.-E. Åmand, *The importance of SO2 and SO3 for sulphation of gaseous KCl – An experimental investigation in a biomass fired CFB boiler.* Combustion and Flame, 2010. **157**(9): p. 1649-1657.
11. Kassman, H., M. Broström, M. Berg and L.-E. Åmand, *Measures to reduce chlorine in deposits: Application in a large-scale circulating fluidised bed boiler firing biomass.* Fuel, 2011. **90**(4): p. 1325-1334.
12. Kassman, H., J. Pettersson, B.-M. Steenari and L.-E. Åmand, *Two strategies to reduce gaseous KCl and chlorine in deposits during biomass combustion—injection of ammonium sulphate and co-combustion with peat.* Fuel Processing Technology, 2013. **105**: p. 170-180.
13. Nielsen, H.P., F.J. Frandsen, K. Dam-Johansen and L.L. Baxter, *The implications of chlorine-associated corrosion on the operation of biomass-fired boilers.* Progress in Energy and Combustion Science, 2000. **26**(3): p. 283-298.
14. Davidsson, K.O., L.-E. Åmand, B. Leckner, B. Kovacevik, M. Svane, M. Hagström, J.B.C. Pettersson, J. Pettersson, H. Asteman, J.-E. Svensson and L.-G. Johansson, *Potassium, Chlorine, and Sulfur in Ash, Particles, Deposits, and Corrosion during Wood Combustion in a Circulating Fluidized-Bed Boiler.* Energy & Fuels, 2007. **21**(1): p. 71-81.
15. Folkeson, N., J. Pettersson, C. Pettersson, L.G. Johansson, E. Skog, B.-Å. Andersson, S. Enestam, J. Tuiremo, A. Jonasson and B. Heikne. *Fireside corrosion of stainless and low alloyed steels in a waste-fired CFB boiler; The effect of adding sulphur to the fuel*. in *Materials Science Forum*. 2008. Trans Tech Publ.
16. Grabke, H.J., E. Reese and M. Spiegel, *The effects of chlorides, hydrogen chloride, and sulfur dioxide in the oxidation of steels below deposits.* Corrosion Science, 1995. **37**(7): p. 1023-1043.
17. Karlsson, S., L.-E. Åmand and J. Liske, *Reducing high-temperature corrosion on high-alloyed stainless steel superheaters by co-combustion of municipal sewage sludge in a fluidised bed boiler.* Fuel, 2015. **139**: p. 482-493.
18. Kiamehr, S., K.V. Dahl, M. Montgomery and M.A.J. Somers, *KCl-induced high temperature corrosion of selected commercial alloys.* Materials and Corrosion, 2015. **66**(12): p. 1414-1429.

19. Lehmusto, J., P. Yrjas, B.J. Skrifvars and M. Hupa, *High temperature corrosion of superheater steels by KCl and K2CO3 under dry and wet conditions.* Fuel Processing Technology, 2012. **104**: p. 253-264.
20. Okoro, S.C., S. Kiamehr, M. Montgomery, F.J. Frandsen and K. Pantleon, *Effect of flue gas composition on deposit induced high temperature corrosion under laboratory conditions mimicking biomass firing. Part I: Exposures in oxidizing and chlorinating atmospheres.* Materials and Corrosion, 2017. **68**(5): p. 499-514.
21. Okoro, S.C., M. Montgomery, F.J. Frandsen and K. Pantleon, *High temperature corrosion during biomass firing: improved understanding by depth resolved characterisation of corrosion products.* Materials at High Temperatures, 2015. **32**(1-2): p. 92-101.
22. Pettersson, J., H. Asteman, J.-E. Svensson and L.-G. Johansson, *KCl Induced Corrosion of a 304-type Austenitic Stainless Steel at 600°C; The Role of Potassium.* Oxidation of Metals, 2005. **64**(1): p. 23-41.
23. Pettersson, J., N. Folkeson, L.-G. Johansson and J.-E. Svensson, *The Effects of KCl, K2SO4 and K2CO3 on the High Temperature Corrosion of a 304-Type Austenitic Stainless Steel.* Oxidation of Metals, 2011. **76**(1): p. 93-109.
24. Sui, J., J. Lehmusto, M. Bergelin and M. Hupa, *The Effects of KCl, NaCl and K2CO3 on the High-Temperature Oxidation Onset of Sanicro 28 Steel.* Oxidation of Metals, 2016. **85**(5): p. 565-598.
25. Enestam, S., D. Bankiewicz, J. Tuiremo, K. Mäkelä and M. Hupa, *Are NaCl and KCl equally corrosive on superheater materials of steam boilers?* Fuel, 2013. **104**: p. 294-306.
26. Lai, G.Y., *High-temperature corrosion and materials applications*. 2007: ASM international.
27. Jonsson, T., S. Karlsson, H. Hooshyar, M. Sattari, J. Liske, J.-E. Svensson and L.-G. Johansson, *Oxidation After Breakdown of the Chromium-Rich Scale on Stainless Steels at High Temperature: Internal Oxidation.* Oxidation of Metals, 2016. **85**(5): p. 509-536.
28. Malede, Y.C., M. Montgomery, K.V. Dahl and J. Hald, *Effect of microstructure on KCl corrosion attack of modified AISI 310 steel.* Materials at High Temperatures, 2018. **35**(1-3): p. 243-254.
29. *BIOMASS ENERGY: Efficiency, Scale and Sustainability*. 2009; Available from: https://www.biomasscenter.org/policy-statements/FSE-Policy.pdf.
30. *Report on conversion efficiency of biomass. BASIS - Biomass Availability and Sustainability Information System*. 2015; Available from: http://www.basisbioenergy.eu/fileadmin/BASIS/D3.5_Report_on_conversion_efficiency_of_biomass.pdf.
31. Peña, J.A.P., *Bubbling Fluidized Bed (BFB), When to use this technology?* Industrial Fluidization South Africa, 2011: p. 1-12.
32. *Schematic drawing of a grate-firing boiler*. Available from: http://www.detroitstoker.com/main/detroit-stokers-reciprograte/.
33. Thunman, H., F. Lind, C. Breitholtz, N. Berguerand and M. Seemann, *Using an oxygen-carrier as bed material for combustion of biomass in a 12-MWth circulating fluidized-bed boiler.* Fuel, 2013. **113**: p. 300-309.
34. Lind, F., A. Corcoran and H. Thunman, *Validation of the oxygen buffering ability of bed materials used for OCAC in a large scale CFB boiler.* Powder Technology, 2017. **316**: p. 462-468.
35. Moldenhauer, P., A. Gyllén and H. Thunman. *A Scale-Up Project for Operating a 115 MWth Biomass-Fired CFB boiler with Oxygen Carriers as Bed Material*. in *Proceedings for the 5th international conference on chemical looping, Park City, USA*. 2018.
36. Liukkonen, M., H. Mikko, E. Halikka, T. Hiltunen and H. Yrjö, *Analysis of Flue Gas Emission Data from Fluidized Bed Combustion Using Self-Organizing Maps.* Applied Computational Intelligence and Soft Computing, 2010. **2010**.
37. *From resource economy to bioeconomy*. Available from: https://sweden.se/climate/#from-resource-economy-to-bioeconomy.
38. *A sustainable energy and climate policy for the environment, competitiveness and long-term stability*. Available from: https://www.iea.org/policiesandmeasures/pams/sweden/name-42459-en.php.

39. Värme, E.O., *Change of fuel composition from 1991 to 2019 in Händeloverket*. 2020, E.On internal data.
40. Lehmusto, J., D. Lindberg, P. Yrjas and L. Hupa, *The Effect of Temperature on the Formation of Oxide Scales Regarding Commercial Superheater Steels.* Oxidation of Metals, 2018. **89**(1): p. 251-278.
41. Folkeson, N., J. Liske, C. Pettersson, L.-G. Johansson, E. Skog, B. Å. Andersson, S. Enestam, J. Tuiremo, A. Jonasson, B. Heikne and J.-E. Svensson, *Fireside Corrosion of Stainless and Low Alloyed Steels in a Waste-Fired CFB Boiler; The Effect of Adding Sulphur to the Fuel*. Vol. 595-598. 2008. 289-297.
42. Li, Y., P. Murphy and C.-Y. Wu, *Removal of elemental mercury from simulated coal-combustion flue gas using a SiO2–TiO2 nanocomposite.* Fuel Processing Technology, 2008. **89**(6): p. 567-573.
43. Nielsen, H.P., F.J. Frandsen and K. Dam-Johansen, *Lab-scale investigations of high-temperature corrosion phenomena in straw-fired boilers.* Energy & Fuels, 1999. **13**(6): p. 1114-1121.
44. Bhadeshia, H. and R. Honeycombe, *Steels: Microstructure and Properties*. 2017: Elsevier Science.
45. Callister, W.D., *Materials Science And Engineering: An Introduction*. 2007: John Wiley & Sons.
46. Sabol, G.P. and R. Stickler, *Microstructure of Nickel-Based Superalloys.* physica status solidi (b), 1969. **35**(1): p. 11-52.
47. *Superalloys: A Primer and History*. Available from: https://www.tms.org/meetings/specialty/superalloys2000/superalloyshistory.html.
48. Kofstad, P., *High Temperature Corrosion*. 1988. 558.
49. *Ellingham Diagram*. [cited 2018 18/06]; Available from: https://www.doitpoms.ac.uk/tlplib/ellingham_diagrams/ellingham.php.
50. West, A.R., *Basic solid state chemistry*. 1999: John Wiley & Sons.
51. Khanna, A.S., *Introduction to High Temperature Oxidation and Corrosion*. 2002: ASM International.
52. Heitjans, P. and J. Kärger, *Diffusion in condensed matter: methods, materials, models*. 2006: Springer Science & Business Media.
53. Kaur, I., W. Gust and Y. Mishin, *Fundamentals of grain and interphase boundary diffusion*. 1995: Wiley Chichester.
54. Wagner, C., *Beitrag zur Theorie des Anlaufvorgangs*, in *Zeitschrift für Physikalische Chemie*. 1933. p. 25.
55. Jones, D.A., *Principles and Prevention of Corrosion*. 1996: Prentice Hall.
56. Jonsson, T., B. Pujilaksono, H. Heidari, F. Liu, J.E. Svensson, M. Halvarsson and L.G. Johansson, *Oxidation of Fe–10Cr in O2 and in O2+H2O environment at 600°C: A microstructural investigation.* Corrosion Science, 2013. **75**: p. 326-336.
57. Greenwood, N.N. and A. Earnshaw, *Chemistry of the Elements*. 2012: Elsevier.
58. Enke, C.G., *Nonstoichiometry, diffusion, and electrical conductivity in binary metal oxides. (Wiley series on the science and technology of materials). P. Kofstad. 160 Abb. 11 Tab. XI, 382 S. Ca. 1060 Schrifttumshinweise. Format 15.5 × 23 cm. Wiley Interscience (J. Wiley & Sons, Inc.) New York-London-Sydney-Toronto,1972. Gebunden ca. DM 52.* Materials and Corrosion, 1974. **25**(10): p. 801-802.
59. Zahs, A., M. Spiegel and H. Jürgen Grabke, *Chloridation and oxidation of iron, chromium, nickel and their alloys in chloridizing and oxidizing atmospheres at 400–700°C*. Vol. 42. 2000. 1093-1122.
60. Abels, J.M. and H.H. Strehblow, *A surface analytical approach to the high temperature chlorination behaviour of inconel 600 at 700 °C.* Corrosion Science, 1997. **39**(1): p. 115-132.
61. Folkeson, N., L.-G. Johansson and J.-E. Svensson, *Initial Stages of the HCl-Induced High-Temperature Corrosion of Alloy 310.* Journal of The Electrochemical Society, 2007. **154**(9): p. C515-C521.
62. McNallan, M., W. Liang, S. Kim and C. Kang. *Acceleration of the high temperature oxidation of metals by chlorine*. in *International Corrosion Conference Series*. 1983. NACE.

63. Shinata, Y., *Accelerated oxidation rate of chromium induced by sodium chloride.* Oxidation of Metals, 1987. **27**(5): p. 315-332.
64. Wang, C.-J. and T.-T. He, *Morphological Development of Subscale Formation in Fe–Cr–(Ni) Alloys with Chloride and Sulfates Coating.* Oxidation of Metals, 2002. **58**(3): p. 415-437.
65. Zahs, A., M. Spiegel and H.J. Grabke, *Chloridation and oxidation of iron, chromium, nickel and their alloys in chloridizing and oxidizing atmospheres at 400–700°C.* Corrosion Science, 2000. **42**(6): p. 1093-1122.
66. Halvarsson, M., J.E. Tang, H. Asteman, J.E. Svensson and L.G. Johansson, *Microstructural investigation of the breakdown of the protective oxide scale on a 304 steel in the presence of oxygen and water vapour at 600°C.* Corrosion Science, 2006. **48**(8): p. 2014-2035.
67. Pettersson, C., T. Jonsson, C. Proff, M. Halvarsson, J.-E. Svensson and L.-G. Johansson, *High Temperature Oxidation of the Austenitic (35Fe27Cr31Ni) Alloy Sanicro 28 in O2 + H2O Environment*. Vol. 74. 2010. 93-111.
68. Jonsson, T., S. Canovic, F. Liu, H. Asteman, J.E. Svensson, L.G. Johansson and M. Halvarsson, *Microstructural investigation of the effect of water vapour on the oxidation of alloy 353 MA in oxygen at 700 and 900°C.* Materials at High Temperatures, 2005. **22**(3-4): p. 231-243.
69. Asteman, H., J.-E. Svensson and L.-G. Johansson, *Evidence for Chromium Evaporation Influencing the Oxidation of 304L: The Effect of Temperature and Flow Rate.* Oxidation of Metals, 2002. **57**(3): p. 193-216.
70. Asteman, H., K. Segerdahl, J.-E. Svensson and L.-G. Johansson, *The Influence of Water Vapor on the Corrosion of Chromia-Forming Steels*. Vol. 369-372. 2001. 277-286.
71. Jenkins, B.M., L.L. Baxter, T.R. Miles and T.R. Miles, *Combustion properties of biomass.* Fuel Processing Technology, 1998. **54**(1): p. 17-46.
72. Vassilev, S.V., D. Baxter, L.K. Andersen, C.G. Vassileva and T.J. Morgan, *An overview of the organic and inorganic phase composition of biomass.* Fuel, 2012. **94**: p. 1-33.
73. Viklund, P., *Superheater corrosion in biomass and waste fired boilers : Characterisation, causes and prevention of chlorine-induced corrosion*, in *Trita-CHE-Report*. 2013, KTH Royal Institute of Technology: Stockholm. p. 55.
74. Cantatore, V., M.A. Olivas Ogaz, J. Liske, T. Jonsson, J.-E. Svensson, L.-G. Johansson and I. Panas, *Oxidation Driven Permeation of Iron Oxide Scales by Chloride from Experiment Guided First-Principles Modeling.* The Journal of Physical Chemistry C, 2019. **123**(42): p. 25957-25966.
75. Jonsson, T., N. Folkeson, J.E. Svensson, L.G. Johansson and M. Halvarsson, *An ESEM in situ investigation of initial stages of the KCl induced high temperature corrosion of a Fe–2.25Cr–1Mo steel at 400°C.* Corrosion Science, 2011. **53**(6): p. 2233-2246.
76. Folkeson, N., T. Jonsson, M. Halvarsson, L.-G. Johansson and J.-E. Svensson, *The influence of small amounts of KCl(s) on the high temperature corrosion of a Fe-2.25Cr-1Mo steel at 400 and 500°C.* Vol. 62. 2011. 606-615.
77. Sutton, A.P. and R.W. Balluffi, *Interfaces in crystalline materials*. 1995: Clarendon Press.
78. Zhou, W., R. Apkarian, Z.L. Wang and D. Joy, *Fundamentals of scanning electron microscopy (SEM)*, in *Scanning microscopy for nanotechnology*. 2006, Springer. p. 1-40.
79. Orloff, J., M. Utlaut, L. Swanson and A. Wagner, *High resolution focused ion beams: FIB and its applications.* Physics Today, 2004. **57**(1): p. 54-55.
80. Khan, A. and R. Srisha, *Image Segmentation Methods: A Comparative Study.* International Journal of Soft Computing and Engineering, 2013: p. 2231-2307.
81. Kaur, D. and Y. Kaur. *Various Image Segmentation Techniques: A Review*. 2014.
82. Hanif, I., *Ion Irradiation Modification of Silicon Nanowires*. 2017, University of Huddersfield.
83. Cullity, B.D. and S.R. Stock, *Elements of X-ray Diffraction*. 2014: Pearson Education.
84. Smart, L.E. and E.A. Moore, *Solid state chemistry: an introduction*. 2016: CRC press.
85. Viklund, P., R. Pettersson, A. Hjörnhede, P. Henderson and P. Sjövall, *Effect of sulphur containing additive on initial corrosion of superheater tubes in waste fired boiler.* Corrosion Engineering, Science and Technology, 2009. **44**(3): p. 234-240.

86. Karlsson, S., E. Larsson, T. Jonsson, J.-E. Svensson and J. Liske, *A Laboratory Study of the in Situ Sulfation of Alkali Chloride Rich Deposits: Corrosion Perspective.* Energy & Fuels, 2016. **30**(9): p. 7256-7267.
87. Okoro, S.C., M. Montgomery, F.J. Frandsen and K. Pantleon, *Time and Temperature Effects on Alkali Chloride Induced High Temperature Corrosion of Superheaters during Biomass Firing.* Energy & Fuels, 2018. **32**(7): p. 7991-7999.
88. Broström, M., S. Enestam, R. Backman and K. Mäkelä, *Condensation in the KCl–NaCl system.* Fuel Processing Technology, 2013. **105**: p. 142-148.
89. Michelsen, H.P., F. Frandsen, K. Dam-Johansen and O.H. Larsen, *Deposition and high temperature corrosion in a 10 MW straw fired boiler.* Fuel Processing Technology, 1998. **54**(1): p. 95-108.
90. Montgomery, M. and A. Karlsson, *In-situ corrosion investigation at Masnedø CHP plant–a straw-fired power plant.* Materials and Corrosion, 1999. **50**(10): p. 579-584.
91. Chen, B., J.N. Hu, P.E.J. Flewitt, A.C.F. Cocks, R.A. Ainsworth, D.J. Smith, D.W. Dean and F. Scenini, *Effect of thermal ageing on creep and oxidation behaviour of Type 316H stainless steel.* Materials at High Temperatures, 2015. **32**(6): p. 592-606.
92. Hudson, J.A., S.G. Druce, G. Gage and M. Wall, *Thermal ageing effects in structural steels.* Theoretical and Applied Fracture Mechanics, 1988. **10**(2): p. 123-133.
93. Jha, B., B. Mishra, B. Satpati and S. Ojha, *Effect of thermal ageing on the evolution of microstructure and degradation of hardness of 2.25 Cr-1Mo steel.* Materials Science-Poland, 2010. **28**(1): p. 335.
94. Malede, Y.C., *Effects of precipitation reactions on KCl induced high temperature corrosion*, in *Department of Mechanical Engineering, Materials and Surface Engineering*. 2019, Technical University of Denmark: Kgs. Lyngby. p. 260.
95. May, J.E., C.A.C.d. Souza, P.A.d.P. Nascente, P. Soares, C.M. Lepienski and S.E. Kuri, *Effect of thermal aging conditions on the corrosion properties and hardness of a duplex stainless steel.* Materials Research, 2010. **13**(4): p. 431-436.
96. Sakthivel, T., S.P. Selvi, P. Parameswaran and K. Laha, *Influence of Thermal Ageing on Microstructure and Tensile Properties of P92 Steel.* High Temperature Materials and Processes, 2018. **37**(5): p. 425-435.
97. Sikka, V., *Effects of thermal aging on the mechanical properties of type 316 stainless steel-elevated-temperature properties*. 1982, Oak Ridge National Lab., TN (United States).
98. Fujikawa, H. and N. Maruyama, *Corrosion behaviour of austenitic stainless steels in the high chloride-containing environment.* Materials Science and Engineering: A, 1989. **120**: p. 301-306.
99. Grabke, H.J., M. Spiegel and A. Zahs, *Role of alloying elements and carbides in the chlorine-induced corrosion of steels and alloys.* Materials Research, 2004. **7**(1): p. 89-95.
100. Malede, Y.C., J.P. Simon, T. Jonsson, M. Montgomery, K.V. Dahl and J. Hald, *KCl-induced corrosion of Ni-based alloys containing 35–45 wt% Cr.* Materials and Corrosion, 2019. **70**(8): p. 1486-1506.
101. Bihlet, U.D., K.V. Dahl and M.A. Somers, *Microstructure of Precipitation Hardenable Powder Metallurgical Ni Alloys Containing 35 to 45 pct Cr and 3.5 to 6 pct Nb.* Metallurgical and Materials Transactions A, 2014. **45**(11): p. 4796-4809.
102. Hjörnhede, A. and A. Nylund, *Adhesion testing of thermally sprayed and laser deposited coatings.* Surface and Coatings Technology, 2004. **184**(2): p. 208-218.
103. Hjörnhede, A., P. Sotkovszki and A. Nylund, *Erosion-corrosion of laser and thermally deposited coatings exposed in fluidised bed combustion plants.* Materials and Corrosion, 2006. **57**(4): p. 307-322.
104. Sadeghimeresht, E., J. Eklund, J.P. Simon, J. Liske, N. Markocsan and S.V. Joshi, *Effect of water vapor on the oxidation behavior of HVAF-sprayed NiCr and NiCrAlY coatings.* Materials and corrosion - Werkstoffe und Korrosion, 2018. **69**(10): p. 1431-1440.
105. Sadeghimeresht, E., N. Markocsan and P. Nylén, *Microstructural and electrochemical characterization of Ni-based bi-layer coatings produced by the HVAF process.* Surface and Coatings Technology, 2016. **304**: p. 606-619.

106. Zeng, Z., N. Sakoda, T. Tajiri and S. Kuroda, *Structure and corrosion behavior of 316L stainless steel coatings formed by HVAF spraying with and without sealing.* Surface and Coatings Technology, 2008. **203**(3): p. 284-290.
107. Madsen, O.H., *Next Generation of Waste Fired Power Plants - Getting the most out of your trash!*, in *NAWTEC15-3205*. 2007: Miami, Florida USA.
108. Paz, L., J. Pother-Simon, T. Jonsson and L. Mikkelsen, *Increased steam temperature with Steamboost superheater - The effect of the combustion in deposits and high temperature corrosion.* 2017.
109. Andersson, S., M.D. Paz, J. Phother-Simon and T. Jonsson, *HIGH TEMPERATURE CORROSION AND DIOXIN ABATEMENT USING SULFUR RECIRCULATION IN A WASTE-TO-ENERGY PLANT.* Detritus, 2019(5).
110. Henderson, P., P. Szakálos, R. Pettersson, C. Andersson and J. Högberg, *Reducing superheater corrosion in wood-fired boilers.* Materials and Corrosion, 2006. **57**(2): p. 128-134.
111. Karlsson, S., J. Pettersson, J.-E. Svensson and L.-G. Johansson. *KCl-Induced High Temperature Corrosion of the Austenitic Stainless Steel 304L–The Influence of SO2*. in *Materials Science Forum*. 2011. Trans Tech Publ.
112. Krause, H., D. Vaughan and W. Boyd, *Corrosion and deposits from combustion of solid waste—Part III: effects of sulfur on boiler tube metals.* 1975.
113. Vainio, E., P. Yrjas, M. Zevenhoven, A. Brink, T. Laurén, M. Hupa, T. Kajolinna and H. Vesala, *The fate of chlorine, sulfur, and potassium during co-combustion of bark, sludge, and solid recovered fuel in an industrial scale BFB boiler.* Fuel Processing Technology, 2013. **105**: p. 59-68.
114. Hunsinger, H., H. Seifert and K. Jay, *Reduction of PCDD/F formation in MSWI by a process-integrated SO2 cycle.* Environmental Engineering Science, 2007. **24**(8): p. 1145-1159.
115. Andersson, S., S. Kreisz and H. Hunsinger, *Dioxin removal: Adiox for wet scrubbers and dry absorbers.* Filtration & Separation, 2005. **42**(10): p. 22-25.
116. PERSDOTTER, A., *Beyond Breakaway Corrosion: Secondary Corrosion Protection of Iron-based Alloys.*
117. Phother-Simon, J., T. Jonsson and J. Liske, *Continuous KCl addition in high temperature exposures of 304 L – A way to mimic a boiler environment.* Corrosion Science, 2020. **167**: p. 108511.
118. Mikkelsen, L., T. Jonsson, L. Paz, J. Eklund, J. Liske, B. Jonsson, N. Israelsson, S. Selin, J. Hernblom, J. Högberg and J. Nockert Olovsjö, *Increased steam temperature in grate fired boilers - Steamboost*, in *KME 709*. 2017. p. 113.
119. Proff, C., T. Jonsson, C. Pettersson, J.-E. Svensson, L.-G. Johansson and M. Halvarsson, *Microstructural investigation of the KCl-induced corrosion of the austenitic alloy Sanicro 28 (35Fe27Cr31Ni) at 600 C.* Materials at High Temperatures, 2009. **26**(2): p. 113-125.
120. Sand, T., C. Geers, Y. Cao, J. Svensson and L. Johansson, *Effective reduction of chromium-oxy-hydroxide evaporation from Ni-base alloy 690.* Oxidation of Metals, 2019. **92**(3-4): p. 259-279.
121. Karlsson, S., J. Pettersson, L.-G. Johansson and J.-E. Svensson, *Alkali induced high temperature corrosion of stainless steel: the influence of NaCl, KCl and CaCl 2.* Oxidation of metals, 2012. **78**(1-2): p. 83-102.
122. Okoro, S.C., M. Montgomery, F.J. Frandsen and K. Pantleon, *High Temperature Corrosion under Laboratory Conditions Simulating Biomass-Firing: A Comprehensive Characterization of Corrosion Products.* Energy & Fuels, 2014. **28**(10): p. 6447-6458.
123. Young, D.J. and B. Gleeson, *Alloy phase transformations driven by high temperature corrosion processes.* Corrosion Science, 2002. **44**(2): p. 345-357.
124. Durham, R.N., B. Gleeson and D.J. Young, *Factors Affecting Chromium Carbide Precipitate Dissolution During Alloy Oxidation.* Oxidation of Metals, 1998. **50**(1): p. 139-165.
125. Tu, J., Z. Li and Z. Mao, *Internal chlorination of Ni-based alloys and its relation to volatilization corrosion.* Materials and Corrosion, 1997. **48**(7): p. 441-446.
126. Li, Y.-K. and R.A. Rapp, *Internal chloridation of dilute Ni-Cr alloys.* MTB, 1983. **14**(3): p. 509-510.

127. Li, Y.S., Y. Niu and M. Spiegel, *High temperature interaction of Al/Si-modified Fe–Cr alloys with KCl.* Corrosion Science, 2007. **49**(4): p. 1799-1815.
128. Li, Y.S., M. Sanchez-Pasten and M. Spiegel. *High temperature interaction of pure Cr with KCl*. in *Materials science forum*. 2004. Trans Tech Publ.
129. Chen, S. and L. Rong, *Effect of silicon on the microstructure and mechanical properties of reduced activation ferritic/martensitic steel.* Journal of Nuclear Materials, 2015. **459**: p. 13-19.
130. Field, K.G., M.A. Snead, Y. Yamamoto and K.A. Terrani, *Handbook on the Material Properties of FeCrAl Alloys for Nuclear Power Production Applications.* 2017.
131. Song, L., E. Guo, L. Wang and D. Liu, *Effects of Silicon on Mechanical Properties and Fracture Toughness of Heavy-Section Ductile Cast Iron.* Metals, 2015. **5**(1): p. 150.
132. Sadeghi, E. and N. Markocsan, *Electrochemical Behavior of Bilayer Thermal-Spray Coatings in Low-Temperature Corrosion Protection*. Vol. 7. 2017.
133. Sadeghimeresht, E., N. Markocsan, P. Nylén and S. Björklund, *Corrosion performance of bi-layer Ni/Cr2C3–NiCr HVAF thermal spray coating.* Applied Surface Science, 2016. **369**: p. 470-481.
134. Eklund, J., J. Phother, E. Sadeghi, S. Joshi and J. Liske, *High-Temperature Corrosion of HVAF-Sprayed Ni-Based Coatings for Boiler Applications.* Oxidation of Metals, 2019. **91**(5-6): p. 729-747.
135. Pint, B.A., Y. Zhang, J.A. Haynes and I.G. Wright, *High temperature oxidation performance of aluminide coatings.* environments, 2003. **9**: p. 12.
136. Texier, D., D. Monceau, Z. Hervier and E. Andrieu, *Effect of interdiffusion on mechanical and thermal expansion properties at high temperature of a MCrAlY coated Ni-based superalloy.* Surface and Coatings Technology, 2016. **307**: p. 81-90.
137. Cverna, F., *Thermal properties of metals.* ASM International, Materials Park, OH, 2002.
138. Totten, G.E., *Handbook of residual stress and deformation of steel*. 2002: ASM international.
139. Jafari, R., E. Sadeghimeresht, T.S. Farahani, M. Huhtakangas, N. Markocsan and S. Joshi, *KCl-induced high-temperature corrosion behavior of HVAF-sprayed Ni-based coatings in ambient air.* Journal of Thermal Spray Technology, 2018. **27**(3): p. 500-511.
140. Steinmetz, P. and C. Rapin. *Corrosion of metallic materials in waste incinerators*. in *Materials science forum*. 1997. Trans Tech Publ.
141. Israelsson, N., *High Temperature Oxidation and Chlorination of FeCrAl Alloys*. 2014: Chalmers University of Technology.
142. Moskowitz, L., *Application of HVOF thermal spraying to solve corrosion problems in the petroleum industry—an industrial note.* Journal of Thermal Spray Technology, 1993. **2**(1): p. 21-29.
143. Hussain, T., T. Dudziak, N. Simms and J. Nicholls, *Fireside corrosion behavior of HVOF and plasma-sprayed coatings in advanced coal/biomass co-fired power plants.* Journal of thermal spray technology, 2013. **22**(5): p. 797-807.
144. Sadeghimeresht, E., N. Markocsan and P. Nylen, *Microstructural characteristics and corrosion behavior of HVAF-and HVOF-sprayed Fe-based coatings.* Surface and Coatings Technology, 2017. **318**: p. 365-373.
145. Varis, T., D. Bankiewicz, P. Yrjas, M. Oksa, T. Suhonen, S. Tuurna, K. Ruusuvuori and S. Holmström, *High temperature corrosion of thermally sprayed NiCr and FeCr coatings covered with a KCl–K2SO4 salt mixture.* Surface and Coatings Technology, 2015. **265**: p. 235-243.
146. Sadeghimeresht, E., L. Reddy, T. Hussain, M. Huhtakangas, N. Markocsan and S. Joshi, *Influence of KCl and HCl on high temperature corrosion of HVAF-sprayed NiCrAlY and NiCrMo coatings.* Materials & Design, 2018. **148**: p. 17-29.
147. *Sulfur Recirculation and improved material selection for high temperature corrosion abatement - KME 714*. 2017.
148. *Combating high temperature corrosion by new materials, testing procedures and improved material selection - KME 711 and KME 720*. 2018.
149. Paz, M.D., D. Zhao, S. Karlsson, J. Liske and T. Jonsson, *Investigating corrosion memory: The influence of previous boiler operation on current corrosion rate.* Fuel Processing Technology, 2017. **156**: p. 348-356.

150. Olivas Ogaz, M.A., L. Paz, T. Jonsson and J. Liske, *Correlation between field and laboratory exposures for boiler corrosion test - mechanistic study of chlorine induce corrosion*. 2018.